PHYSICAL PROPERTIES OF MACROMOLECULE-METAL OXIDE NANOPARTICLE COMPLEXES: Magnetophoretic Mobility, Sizes, and Interparticle Potentials

Olin Thompson Mefford IV

Dissertation submitted to the faculty of the Virginia Polytechnic Institute and State University in partial fulfillment of the requirements for the degree of

Doctor of Philosophy
in
Macromolecular Science and Engineering

Approved by:

Judy S. Riffle (Chair)
Richey M. Davis
Timothy G. St. Pierre
James. E. McGrath
Brian J. Love

June 14, 2007
Blacksburg, Virginia

Keywords: magnetite, nanoparticle, magnetophoretic mobility, polydimethylsiloxane, TEM, DLS, SQuID, DLVO theory, rheology

PHYSICAL PROPERTIES OF MACROMOLECULE-METAL OXIDE NANOPARTICLE COMPLEXES: Magnetophoretic Mobility, Sizes, and Interparticle Potential

Olin Thompson Mefford

Abstract

Magnetic nanoparticles coated with polymers hold great promise as materials for applications in biotechnology. In this body of work, magnetic fluids for the treatment of retinal detachment are examined closely in three regimes; motion of ferrofluid droplets in aqueous media, size analysis of the polymer-iron oxide nanoparticles, and calculation of interparticle potentials as a means for predicting fluid stability. The macromolecular ferrofluids investigated herein are comprised of magnetite nanoparticles coated with tricarboxylate-functional polydimethylsiloxane (PDMS) oligomers. The nanoparticles were formed by reacting stoichiometric concentrations of iron chloride salts with base. After the magnetite particles were prepared, the functional PDMS oligomers were adsorbed onto the nanoparticle surfaces.

The motion of ferrofluid droplets in aqueous media was studied using both theoretical modeling and experimental verification. Droplets (~1-2 mm in diameter) of ferrofluid were moved through a viscous aqueous medium by an external magnet of measured field and field gradient. Theoretical calculations were made to approximate the forces on the droplet. Using the force calculations, the times required for the droplet to travel across particular distances were estimated. These estimated times were within close approximation of experimental values.

Characterization of the sizes of the nanoparticles was particularly important, since the size of the magnetite core affects the magnetic properties of the system, as well as the long-term stability of the nanoparticles against flocculation. Transmission electron microscopy (TEM) was used to measure the sizes and size distributions of the magnetite cores. Image analyses were conducted on the TEM micrographs to measure the sizes of approximately 6000 particles per sample. Distributions of the diameters of the magnetite cores were determined from this data. A method for calculating the total particle size, including the magnetite core and the adsorbed polymer, in organic dispersions was established. These estimated values were compared to measurements of the entire complex utilizing dynamic light scattering (DLS). Better agreement was found for narrow particle size distributions as opposed to broader distribution.

The stability against flocculation of the complexes over time in organic media were examined via modified Derjaguin-Landau-Verwey-Overbeek (DLVO) calculations. DLVO theory allows for predicting the total particle-particle interaction potentials, which include steric and electrostatic repulsions as well as van der Waals and magnetic attractions. The interparticle potentials can be determined as a function of separation of the particle surfaces. At a constant molecular weight of the polymer dispersion stabilizer, these calculations indicated that dispersions of smaller PDMS-magnetite particles should be more stable than those containing larger particles. The rheological characteristics of neat magnetite-PDMS complexes (i.e, no solvent or carrier fluid were present) were measured over time in the absence of an applied magnetic field to probe the expected properties upon storage. The viscosity of a neat ferrofluid increased over the course of a month, indicating that some aggregation occurred. However, this effect could be removed by shearing the fluids at a high rate. This suggests that the particles do not irreversibly flocculate under these conditions.

Acknowledgements

I would like to begin by expressing my deep gratitude to my advisor Prof. Judy Riffle. She has been an advocate and has always encouraged me take advantage of the opportunities that have been available. I would also like to thank the members of my committee, who have become close friends and great collaborators. Appreciation is extended to Prof. Richey Davis for the countless conversations and "number-crunching" that has made much of this work possible. Thanks is extended to Prof. James McGrath for the excellent guidance and instruction at the beginning of my graduate career, and the excellent wine and restaurant choices today. Dr. Brian Love is thanked for his advice on biomaterials. Finally, Prof. Tim St. Pierre is thanked for being a great friend and mentor during my various visits to the University of Western Australia. Whether we were cooking pickles in the biophysics lab or trying our best to get to Rottnest Island despite the weather, it was always a blast.

Keeping on the Australian side of the world, I am in great debt to Dr. Robert Woodward. During both of my visits, he was by my side for all of our discoveries whether planned or not. My knowledge of magnetism and experimental design would not be present if it were not for Rob. In addition, Matt Carroll has been the ideal collaborator. His care and precision matches well with my haphazard nature. Also special thanks go to Annette Tyler, Anne Dinh, Sara Hackett, Wanida Chua-anusorn, and Mike House. You guys were always there for me, whether the issue was work-related or otherwise.

Also some words need to go out to my lab mates in Virginia. Thanks for all of the adventures and making each day have a new surprise. The long lunches and occasional parties have been a great distraction. I hope that you will continue to keep our reputation for conferences to come. Specific thanks goes to Dr. Michael Vadala for synthesizing most of the materials I have worked with in the past year; Shane Thompson and Dr. Yin Lin for helping me sort out any synthetic issues I was having. Jonathon Goff, Phil Huffstetler, Nikorn Pothayee, and Jon Boyd for keeping me on my toes in the lab and downtown. On the chemical engineering side of things, thanks goes to Beth Caba, Will Miles, and Akelish Garg for helping me when I was out of my element.

I am also thankful for the generous assistance by Angie Flynn. She made the impossible possible. No matter how last minute my request seemed to be, she was there to help me through my problems. I truly believe that our labs would not function without her watchful eye.

Outside the lab I have some outstanding friends to thank for their support. To my various roommates through the years, Dave Schilling, Massi Naso, Bryce Guyer, and Selanga Ranawaka. Special thanks goes to Kerry Wood. You have taught me more than you know. Also thanks goes to my Bollo's/Cellar buddies; Lee Bryant, Bine Sibler, Krista Rule, Nick Wiggington, Callie Raulfs, and Tiffany Adams. You have all been great friends and supported me throughout.

I also want to thank the support of my parents Olin and Donna Mefford. Thank you for the freedom to direct my future. You were always there to encourage me. Finally, I want to acknowledge my fiancé Julie Franklin who has been my shining light. Even though we were apart for most of my time at Virginia Tech, my love and gratitude for you has continued to grow. I am excited that we will soon lead the life less ordinary together.

"Today's scientists have substituted mathematics for experiments, and they wander off through equation after equation, and eventually build a structure which has no relation to reality." -Nikola Tesla[1]

Attribution

Mr. Jonathon D. Goff at Virginia Tech synthesized the ferrofluids in Chapter 2, and advised on the synthesis and preparation of the nanoparticles in Chapters 3 and 4.

Mr. Timothy P. Vadala at Virginia Tech synthesized the ferrofluids in Chapter 2.

Dr. J.P. Dailey of the Erie Retinal Clinic provide assistance in design of devices for the treatment of retinal detachment. He particularly aided in designing the sizes and viscosity properties seen of the measurement of magnetophoretic mobility presented in Chapter 2.

Mr. Matthew R. L Carroll at the University of Western Australia aided in the development of the magnetic separation column used in Chapter 3 and 4. In addition, all TEM images in Chapters 3 and 4 were taken by him at the University of Western Australia's Center for Microscopy and Microanalysis.

Dr. Michael L. Vadala of NanoMedics synthesized the polymers and nanoparticles presented in Chapters 3 and 4. He also oversaw the measurement of DLS and rheology presented in those chapters.

Ms. Raquel Mejia-Ariza of Virginia Tech was responsible for DLS and rheology measurements presented in Chapters 3 and 4.

Dr. Martin Saunders of the University of Western Australia aided in the development of the analysis of TEM images presented in Chapter 3.

Dr. Beth Caba of Virginia Tech developed the method in which the radius of polymer-particle is converted into a radius of gyration by calculating the mass and moment of inertia presented in chapter 4.

Dr. Robert C. Woodward at the University of Western Australia provided guidance and assitance in experimental set up and design for the measurement of the magnetophoretic mobility of ferrofluid droplets presented in Chapter 2. In addition, he help develop the technique for the analysis of TEM images presented in Chapter 3 and 4.

Dr. Richey M. Davis of Virginia Tech is assisted in the application of the brush density model that led to particle size predictions presented in Chapters 3 and 4. He is also advised heavily on the calculations of particle interactions presented in chapter 4.

Dr. Timothy G. St. Pierre acted advisor during my time at the University of Western Australia and supervised experimental design and contributed to the calculations of magnetophoretic mobility in Chapter 2.

Dr. Judy .S. Riffle was my principle advisor throughout my graduate career. She directly assessed in overall project design and overviewed publications and communications of my work at Virginia Tech of which this document is a result.

List of Symbols and Abbreviations

a	power-law coeffecient
α	Langevin argument $\alpha = \frac{\pi}{6}\frac{\mu_0 M_d H d^3}{kT} = \frac{mH}{kT}$
α	Weibull scale parameter
A	area
$\bar{A}$	average area
AIBN	2,2'-azobisisobutyronitrile
B	field induction
c	speed of light
c_∞	characteristic ratio
γ	shear strain or Weibull shape parameter
$\dot{\gamma}$	shear rate
δ	dimensionless surface-to-surface distance
d	diameter
DD	density distribution
DLS	dynamic light scattering
DLVO	Derjaguin-Landau-Verwey-Overbeek theory
D_3	hexamethylcyclotrisiloxane
$\bar{D}_v$	volume average diameter
Δ_{ss}	surface-to-surface distance
Δ_{cc}	center-to-center distance
ε	surface concentration of adsorbed molecules
ε_0	permittivity of free space
$\varepsilon(0)$	dielectric constant of the medium
$\bar{\varepsilon}(0)$	dielectric constant of the substrate
E	energy
E_s	energy from steric repulsion
F	force

F_D drag force

F_m magnetic force

$F(\delta)$ retardation factor

g grams

g acceleration due to gravity

G Gauss

$\hbar$ Planck's constant

H field

H_c coercivity

I inertia

$1/\kappa$ Debye length

k_B Boltzmann's constant, 1.38 x 10^{-23} $N \cdot m \cdot K^{-1}$

l surface separation parameter

l_0 average length of a backbone bond

$L(\alpha)$ Langevin function

L_k statistical segment length

m mass

m_s mass per segment

m meter

m moment

M magnetization

MRI magnetic resonance imaging

M_d saturation magnetization of the bulk material

M_r remanent magnetization

M_s saturation magnetization

μ_0 permeability of free space, 4π x 10^{-7}

n power-law exponent

n number of bonds in the backbone of a chain

n_0 low frequency refractive index of the medium

$\overline{n_0}$ low frequency refractive index of the substrate

N_a	Avogadro's number
N_k	number of Kuhn segments
η	viscosity
η_0	zero-shear viscosity
$[\eta]$	intrinsic viscosity
η_r	relative viscosity
η_s	viscosity of the solution
π	pi
P(r)	probability of a particle as a function of radius, r
Pa	Pascal
PDMS	polydimethylsiloxane
ρ	density
$\Delta\rho$	difference in density
ϕ	volume fraction
ϕ_m	maximum-packing volume fraction
r	radius
R_c	radius of core
R_g	radius of gyration
R_m	radius of complex
s	second
σ	shear stress
σ	length scale of blob model diameter
SQuID	superconduting quantum interference device
T	temperature or Tesla
TEM	transmission electron microscopy
TGA	thermogravimetric analysis
THF	tetrahydrofuran
U	velocity
v	Flory exponent

V	volume
$\bar{V}$	average volume
V_a	van der Waals potential
V_e	electrostatic potential
V_m	magnetic potential
V_s	steric potential
V_{total}	total interparticle potential
ω	frequency of the dominant relaxation in the UV
Ψ_0	surface potential
z	elevation in the gravitational field
Z	distance traveled by the droplet
$\xi(r)$	blob diameter

Table of Contents

List of Figures

List of Tables

1. Chapter 1: Introduction

1.1. Magnetic Materials Containing Magnetite Particles

Several types of magnetic fluids have been developed. The most noteworthy and the subject of this body of work are colloidal ferrofluids. Ferrofluids are colloidal suspensions of particles, which may or may not settle out slowly. A typical fluid contains around 5% by volume of magnetic particles and around 10% by volume of a dispersion stabilizer. The remaining volume is comprised of the carrier fluid.[2] Rosensweig asserts that a true ferrofluid does not settle out. Rather, these materials will exhibit a "slight concentration gradient" after long exposure to a magnetic or gravitational force.[3] Ferrofluids are composed of coated single domain magnetic particles (3-15 nm) suspended in a liquid carrier fluid. These materials remain suspended due to thermal energy and the surface coatings prevent aggregation.[3] Because of their high sensitivity to electromagnetic energy, ferrofluids have been applied to such applications as seals, bearings, dampers, stepping motors, loudspeakers, and sensors.[2] Magnetorheological fluids have also been developed. These are composed of larger particles, typically on the order of microns or more. These fluids will solidify in the presence of magnetic materials/fields. In contrast, ferrofluids will continue to flow in the presence of a magnetic field.[3] This flow behavior will be discussed in the many sections that follow. This body of work will focus on ferrofluids, and more specifically on magnetite nanoparticles that are coated with polydimethylsiloxane oligomers to be utilized in biotechnological applications.

Magnetite exists naturally in a variety of biological settings. In one of the simplest forms of life, bacteria contain discrete magnetite particles in tiny organelles called magnetosomes. The magnetosomes are often arranged in linear chain structures inside the bacterial cells.[4] Magnetite has also been reported in rainbow trout,[5] salmon,[6] sea turtles,[7] albatrosse,[8] and petrels.[9] It is proposed that the magnetite found in the mucus of some of these species acts as a geomagnetic field receptor, aiding the animal in directional sensing.[5, 6] In humans magnetite has been found in the heart, spleen, liver and brain. The highest concentrations have been in the heart.[10] However, it has been suggested that magnetite has no association with geomagnetic field sensing in humans.[11] Nonetheless, the presence of naturally occurring magnetite in the body suggests that synthetically derived materials should be biocompatible, and this lack of toxicity opens opportunities for a wide variety of biomedical applications using magnetic nanoparticles.

Magnetic nanoparticles have been demonstrated to have exceptional properties for MRI contrast enhancement, drug targeting and delivery, hyperthermia treatment, and magnetic separations of bioagents.[12, 13] In addition, we have worked for several years to develop hydrophobic ferrofluids for treating retinal detachment.[14-18] Retinal detachment is a leading cause of blindness, and currently available treatments fail in as many as 1/3 of complicated retinal detachment patients, resulting in partial or complete loss of vision for several million people worldwide. A retinal tear provides a pathway for vitreous fluid to pass through and underneath the retina, thus detaching the retina from the choroid. The goal of surgery is to close any holes in the retina, preventing further fluid flow into the sub-retinal space, allowing for reattachment of the retina. Chapter 2 will provide greater detail regarding the proposed treatments.

The goal of this dissertation has been to refine the magnetite-PDMS materials for treating retinal detachment, and to characterize their unique properties. The remainder of this chapter gives background on magnetic materials, synthetic routes to magnetite nanoparticles, interparticle interactions, and the rheology of particle systems. Chapter 2 will discuss the mobility of ferrofluid droplets in aqueous media. The motion of the droplets has been measured, and theoretical models are presented that describe the motion as a function of droplet size, droplet composition, properties of the external magnetic field, and the medium that the droplet was moved through. Chapter 3 discusses a refinement in the magnetic nanoparticles by means of magnetic filtration, in which large particles and aggregates were removed from the distributions. Size analyses and methods for size prediction are also presented. Chapter 4 discusses the interparticle interaction potentials between the nanoparticles in dispersions. By calculating the total interaction potential, inferences were made regarding the stability of the ferrofluids over time. These inferences were then compared to aging studies of neat magnetite-PDMS fluids utilizing sensitive rheological measurements. Chapter 5 offers some conclusions from this work and suggestions for possible future projects.

1.2. Fundamentals of Magnetic Materials

Understanding the magnetic properties of ferrofluids involves the properties of multi and single domain materials. Solid ferromagnetic materials contain domains, each composed of groups of atoms with oriented moments in fixed directions. Multiple domains within a solid

material with magnetic moments oriented in different directions result in the total field energy being reduced relative to a single domain material. However, because the formation of domain boundaries comes at a cost in energy, an infinitesimal amount of domains is not possible. Rather an energy balance is reached between the energy gained by having individual domains and the energetic expense of their formation. In some cases it is energetically more favorable for moments of all domains to be aligned. This is referred to as ferromagnetic behavior. Iron, nickel, cobalt, and many alloys of each exhibit this behavior. Antiferromagnetic materials demonstrate no net magnetic moment, due to alternating moments from atom to atom. Such materials include MnO, FeO, NiO, $FeCl_2$, MnSe, and many others. Ferrimagnetic materials exhibit a net moment less than that of ferromagnetic materials because of unequal alternation in their magnetic moments. This behavior is often observed in ferrites of the general formula $MO{\bullet}Fe_2O_3$, where *M* represents Fe, Ni, Mn, Cu or Mg. Magnetite, Fe_3O_4, is probably the best known of these ferrites. It has a cubic crystalline structure. Paramagnetic materials align with an applied magnetic field but lack long-range order in the absence of a field. Such materials include liquid oxygen, rare-earth materials, and ferromagnets above their Curie temperature.[3] Table 1.1 illustrates the different types of magnetic behavior.

Table 1.1: Types of Magnetic Behavior

Class	Domains	Organization of Spins[3]	Atomic Structure[19]
Ferromagnetism	Yes		Atoms have permanent spins and particle interactions result in even alignment (parallel)
Antiferromagnetism	Yes		Atoms have permenent spins and particle interactions result in alignment (antiparallel)
Ferrimagnetism	Yes		Atoms have permanent spins and particle interactions result in uneven antiparallel alignment
Paramagnetism	No		Atoms have permanent spins, but particle interactions are weak
Diamagnetism	No		Atoms have no permanent magnetic spin moment

Magnetic hysteresis loops are commonly employed to describe the properties of magnetic materials. Figure 1.1 illustrates a typical hysteresis loop in which the magnetization of the material, M, is measured relative to the applied field, H. When a sufficiently large field is applied the majority of spins within the material align with the field. The magnetization in these cases is described as the saturation magnetization, M_s. As the field is reduced, the spins in the material no longer align perfectly with the field, and some spins remain aligned at zero field. The magnetization at that point is described as the remanent magnetization, M_r. The field is further decreased until the magnetization becomes zero. This point is the coercive field, H_c. This is the magnitude of field that must be applied to bring the net moment of the sample to zero.[3, 20]

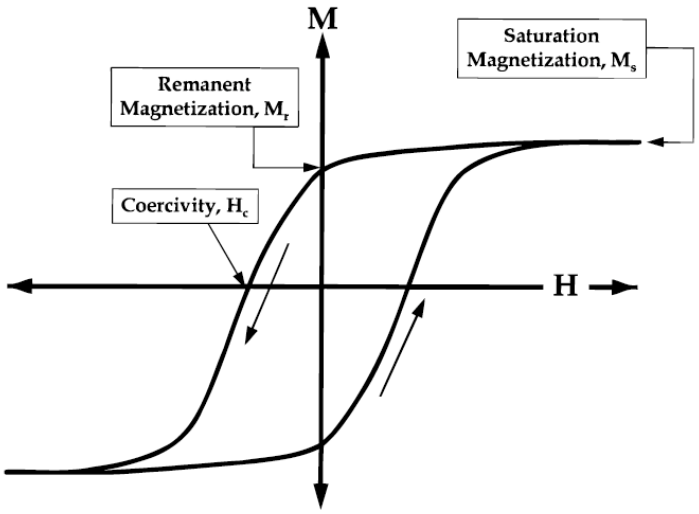

Figure 1.1: Typical hysteresis loop for a ferromagnetic material illustrating saturation magnetization, M_s, remanent magnetization, M_r, and coercivity, H_c

Ferrofluids are colloidal suspensions of single domain particles of ferro- or ferrimagnetic materials. For magnetite, the maximum diameter for which particles can overcome anisotropy to become a single domain was calculated by Kittel to be 128 nm.[21] Because the particles in suspensions are single domain particles, each particle in a ferrofluid has its own magnetic moment, **m**. In the absence of a field, the moment of each particle is randomly oriented, resulting in no net magnetization for the ferrofluid. However, as an applied field is increased, the particles will become increasingly aligned with the field. It is possible at very high fields that

the particles become completely aligned, reaching a saturation magnetization, M_s. When the field is removed the particles will relax back into a state of random order of the directions of magnetic moments, with no remanent magnetization for the material (Figure 1.2). This behavior is referred to as superparamagnetic.[3] The term 'superparamagnetic properties' is often used to describe nanomaterials. It should be understood that Neel relaxation (relaxation of the magnetic moment due to thermal energy) is the underlying driving force for superparamagnetism rather than other relaxation factors, e.g. Brownian relaxation.[20] That is, particles that can freely rotate during magnetometry experiments will appear as though they have superparamagnetic behavior, due to randomization caused by particle rotations. However, if the particles are held rigidly in place, some coercivity may be observed.

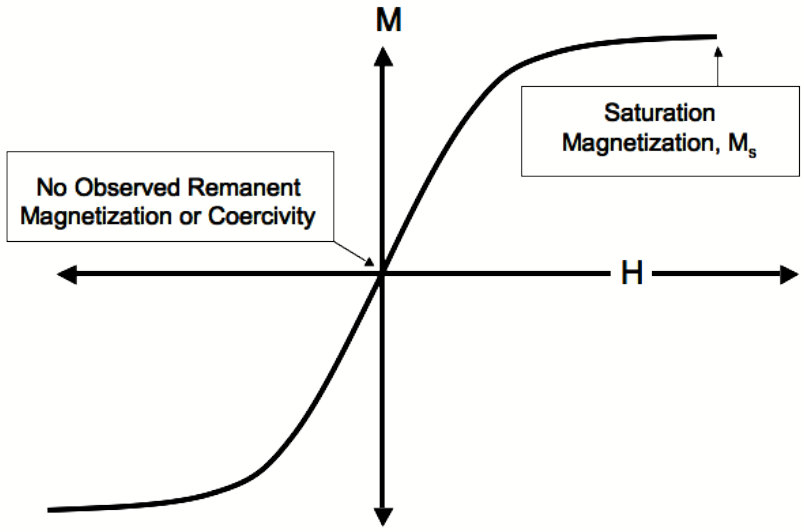

Figure 1.2: Hysteresis loop for a material that has superparamagnetic behavior

The magnetization, M, for a superparamagnetic material can be best described by a Langevin function, $L(\alpha)$.

$$\frac{M}{\phi M_d} = \coth\alpha - \frac{1}{\alpha} \equiv L(\alpha)$$

Eq. 1.1

where $\alpha = \frac{\pi}{6}\frac{\mu_0 M_d H d^3}{k_B T} = \frac{mH}{k_B T}$, ϕ is the volume fraction, M_d is the saturation magnetization of the bulk material, μ_0 is the permeability of free space, H is the applied field, d is the diameter of the particles, **m** is the moment of the particles, k_B is Boltzman's constant, and T is the absolute temperature in Kelvin. This equation can be used to determine particle size via magnetometric measurements. Figure 1.3 illustrates the calculated magnetization values for monodisperse spherical magnetite particles of varying sizes. Particles with smaller diameters have a lower relative susceptibility.

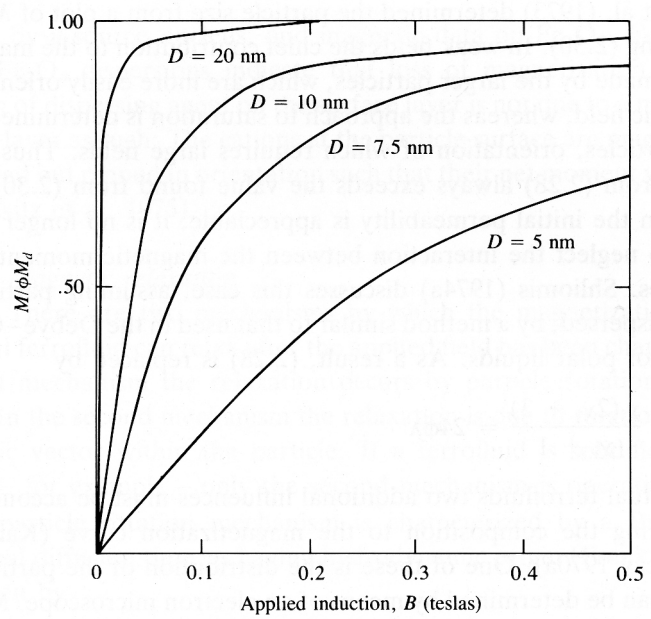

Figure 1.3: Calculated magnetization for magnetite nanoparticles with varying diameters in which smaller particles have lower suceptibility[3] [Reprinted by permission of Cambridge University Press]

1.3. Methods for the Synthesis of Ferrofluids

The production of ferrofluids can be divided into two categories. One can either make little particles by grinding larger particles, or produce the little particles from solution.[3] The first option was developed by S. Papell in 1965.[22] Typically this process began with micron sized material, 10-20 volume percent of a suspending agent, and a liquid medium. The materials were ground for extended periods (~1000 hours). Rosensweig and Kaiser demonstrated that ferrofluids could be prepared by this method in a variety of media, including water,

hydrocarbons, aromatics, and esters. The authors noted a ten-fold increase in the saturation magnetization of the fluids following extended grinding.[23]

The second method involves chemical precipitation in an organic or aqueous solvent. There are several different variations of this process. The most commonly used method was developed by Khalafalla and Reimers.[24-26] This process involves the co-precipitation of iron oxide particles, through reaction of iron salts with hydroxide (Figure 1.5).

$$5NaOH + 2FeCl_3 + FeCl_2 \rightarrow Fe_3O_4 + 5NaCl + 5H_20$$

Figure 1.4: Reaction scheme for the co-precipitation of magnetite

Typical sizes of magnetite nanoparticles produced by co-precipitation are around 10 nm in diameter. Unfortunately broad polydispersities and aggregation are concerns with this process. McNab et al. demonstrated that particles produced in this manner have a relatively broad distribution.[27] Nevertheless, recent efforts have utilized this method to synthesize biocompatible ferrofluids.[17, 28] A wide variety of surfactants have been utilized to stabilize the materials in both polar and non-polar media. Shen et al. demonstrated via SANS measurements that particles could be stabilized in water via adsorption of two layers of surfactants onto the nanoparticles.[29]

Over the years additional techniques have been investigated for gaining control over the sizes of magnetic nanoparticles synthesized by co-precipitation. These include alterations of the ionic properties of solutions to drive the precipitation of larger particles out of solution due to electrostatic shielding effects.[30-33] While these techniques are effective in polar solvents, their use in organic solvents is limited. Another method for size control of magnetic nanoparticles is to utilize size exclusion chromatography (SEC) for separation of the particle distributions. In SEC, dispersions of particles are passed through a nanoporous material in which larger particles elute faster than smaller particles. However, particles that are too big to pass through the pores do not elute at all.[34] This method is limited by expensive separation media and particle size distributions that cannot be adequately separated.[35]

Recent efforts by Sun et al. have demonstrated that magnetite can be synthesized via reduction of iron(III) acetylacetonate, $Fe(acac)_3$, at elevated temperatures in the presence of oleic acid and oleylamine as steric dispersion stabilizers.[36] This method leads to relatively narrow distributions of particles sizes. In addition, the degree of flocculation observed via TEM is significantly less than for magnetite produced via co-precipitation in the absence of the

dispersion stabilizers.[36, 37] Bae et al. reported that the temperature of these reactions directly relates to the particle size and the size distribution.[38]

Metal carbonyl thermolysis reactions have been utilized to synthesize ferrofluids with elemental cobalt or iron nanoparticles. This was first described by Thomas,[39] and Hess and Parker.[40] For example, dicobalt octacarbonyl ($Co_2(CO)_8$) was dissolved in an organic solution with a dispersion stabilizing agent. At elevated temperatures the carbonyl ligands were displaced to form elemental cobalt nanoparticles. This method has been further developed through the years.[30, 41-47]

Thermolysis methods to form metal nanoparticles can also be conducted in aqueous environments by utilizing ultrasonic pulses to quickly elevate the solution temperature. It has been reported that hot spots with temperatures as high as 5000 K and lifetimes of approximately a nanosecond can exist in selected examples of these reactions.[48, 49].

Sonication has also be used to produce magnetite nanoparticles, $Fe(CO)_5$ has been charged into a solution of decane containing surfactants such as 11-undecenoic acid (CH_2=CH(CH_2)$_8$COOH), dodecyl sulfonic acid ($C_{12}H_{17}PO_3H_2$), or octyl phosphonic acid ($C_8H_{17}PO_3H_2$). The solutions were sonicated for approximately three hours at room temperature, and this yielded magnetite particles with similar distributions to those prepared by co-precipitation of iron salts.[50] Kumar et al. reported a similar procedure with iron(II) acetate in deoxygenated water.[51] The authors later reported that adding dextran to the reaction resulted in rod-shaped particles with broader distributions.[52] However, the use of poly(vinyl alcohol) as a stabilizer reportedly resulted in monodisperse particles.[53]

Hygrothermal synthetic routes yield particles with similar properties to those prepared by thermolysis. Hygrothermal reactions consist of aqueous solutions, which are heated (~200ºC) in high-pressure autoclaves.[2] Under these conditions, hydrolysis rates are accelerated, allowing rapid propagation of nucleated particles. Magnetite nanoparticles have been synthesized by oxidation of iron(II) 2-methoxyethoxide ($Fe(OCH_2CH_2OCH_3)_2$) in 2-methoxyethanol-H_2O solutions as the solvent medium. By varying the ratio of 2-methoxyethanol to water, the resulting iron oxide powder could be varied from α-Fe_2O_3 to Fe_3O_4.[54] In addition, Yi et al. produced rather polydisperse magnetite particles by adding ammonia to aqueous solutions of $FeCl_3$.[55]

Relatively narrow distributions of magnetite particles have been synthesized in reverse micelles. A typical procedure utilizes an organic solvent in which a surfactant is added to form micelles with hydrophilic cores. Aqueous solutions of magnetite precursors were subsequently added to the interior of the micelles. The micelles function as mini-reactors, allowing for good heat dissipation, and they prevent aggregation during particle formation. Examples of surfactants that have been employed in such procedures include bis(2-ethylhexyl) sodium sulfosuccinate (AOT)[56, 57], polyoxyethylene(5) nonyl phenyl ether[58], polyoxyethylene(9) nonyl phenyl ether[58], and sodium dodecyl sulfate (Na(DS)).[59]

Electrodeposition has also been used to synthesize magnetite nanoparticles. Banerjee et al. dissolved $FeCl_3$ in a solution of tetraethylorthosilicate.[60] A small amount of acid was added to the solution and the mixture was allowed to cure for a couple of weeks. This mixture was then ground and converted to a paste by adding water. The paste was spread onto an iron cathode and voltages from 10-20 V were applied across the paste. The resulting iron oxide particles had diameters ranging from 5-11 nm depending on the concentration of $FeCl_3$ and the applied voltage.[60]

1.4. Colloidal Properties and Energetics of Ferrofluids

The flow properties of ferrofluids are similar to those of colloidal dispersions of nonmagnetic materials. The particles in ferrofluids have stabilization energies sufficient to maintain dispersion even in the presence of magnetic fields.[3] Colloids are defined as suspensions of small particles. The term "colloid" is a derivative of the Greek word κολλα, meaning glue. As early as the 17th century, alchemists created stable suspensions of inorganic particles such as gold. Organic suspensions found in the milky sap of rubber trees were first utilized in the 19th century. These suspensions of small particles of insoluble rubber in an aqueous fluid were referred to as latexes, and this led to the term "latex" that is currently applied to stable suspensions of polymeric particles. By the 1950s, scientists had prepared monodisperse suspensions of polymeric particles. It is through this work that mathematical models were devised to describe the flow properties of colloidal suspensions.[61]

The behavior of colloidal suspensions is tied directly to their thermodynamic properties. This discussion will begin by considering the different energetic terms for each particle that affect the stability of ferrofluids. For each particle we can consider

$$\text{Thermal energy} = k_B T$$

Eq. 1.2

$$\text{Magnetic energy} = \mu_0 MHV$$

Eq. 1.3

and

$$\text{Gravitational energy} = \Delta\rho V g z$$

Eq. 1.4

where k_B is Boltzmann's constant, T is absolute temperature in Kelvin, μ_0 is the permeability of free space, H is field, M is the magnetization, V is volume, $\Delta\rho$ is the difference in density between the particle and the solution, **g** is the acceleration due to gravity, and z is the elevation in the gravitational field.[3]

Regarding the stability of particles in an external magnetic field, we can consider the case where the thermal energy of the system imparts motion to the particles in opposition to the attractive magnetic forces that pull the particles together. For stability to be maintained, thermal energy must be greater than magnetic energy, yielding the following:

$$\frac{thermal\ energy}{magnetic\ energy} = \frac{k_B T}{\mu_0 MHV} \geq 1$$

Eq. 1.5

By describing volume in terms of diameter, d, and then solving for particle diameter the following results:

$$d \leq \left(\frac{6 k_B T}{\pi \mu_0 MH} \right)^{1/3}$$

Eq. 1.6

Rosensweig considered the following conditions to substitute into equation 1.6 for the case of magnetite nanoparticles and a permanent (portable) magnet at room temperature.[3]

$$H = 8 \times 10^4 \, A/m$$
$$M = 4.46 \times 10^5 \, A/m$$
$$T = 298 K$$

Eq. 1.7

The field, H, corresponds to a field of 1000 Gauss. The magnetization, M, corresponds to 5600 Gauss. Inserting the values results in

$$d \leq 8.1 \times 10^{-9} m \text{ or } 8.1 \text{ nm}$$

Eq. 1.8

This analysis only applies to a single nanoparticle, and does not consider interparticle forces such as van der Waals attractions or electrostatic or steric repulsions. Thus, in reality, magnetite nanoparticle sizes can be larger and dispersion stability can be maintained. However, it should be considered that particles of far greater volume would not have sufficient thermal energy to remain dispersed in the presence of magnetic fields.[3] This force balance will become more complex as interparticle interactions along with steric forces are considered.

Staying in the realm of energetics of a single particle, a comparison can be made between gravitational and magnetic energy. The ratio between gravitational energy and magnetic energy is

$$\frac{gravitational\ energy}{magnetic\ energy} = \frac{\Delta \rho g z}{\mu_0 M H}$$

Eq. 1.9

Again the values for magnetite nanoparticles in combination with a handheld permanent magnet at room temperature can be substituted into Eq. 1.9, along with the following values:

$$z = 0.05 m$$
$$\Delta \rho = \rho_{solid} - \rho_{fluid} = 5300 kg \cdot m^{-3} - 1000 kg \cdot m^{-3} = 4300 kg \cdot m^{-3}$$
$$g = 9.8 \frac{m}{s^2}$$

Eq. 1.10

The ratio is the following:

$$\frac{gravitational\ energy}{magnetic\ energy} = 0.047$$

Eq. 1.11

Based upon this calculation, magnetic force effects should be a greater concern than gravitational forces.[3]

Having compared the lone particle energetics, the thermal energy required to inhibit magnetic agglomeration will be compared by including effects of interparticle interactions. Because magnetite nanoparticles exhibit superparamagnetic behavior, each particle has one moment. The energy required to separate two particles of diameter, d, when the particles are in alignment is considered. This dipole-dipole energy, E_{dd}, can be described by

$$E_{dd} = \frac{\pi}{72}\frac{\mu_0 M^2 d^6}{\left(\Delta_{ss} + d\right)^3}$$

Eq. 1.12

where Δ_{ss} is the surface-to-surface separation distance. If we set s = 0, meaning that particles are in contact, the energy equation reduces to

$$E_{dd} = \tfrac{1}{12}\mu_0 M^2 V$$

Eq. 1.13

By considering the ratio of thermal energy to magnetic dipole-dipole energy, one can solve for the maximum diameter of the nanoparticle that will allow thermal energy to compensate for the magnetic dipole interparticle interaction.

$$\frac{thermal\ energy}{dipole-dipole\ contact\ energy} = \frac{24 k_B T}{\mu_0 M^2 V} \geq 1$$

$$\left(\frac{144 k_B T}{\pi \mu_0 M^2}\right)^{1/3} \geq d$$

$$9.8nm \geq d$$

Eq. 1.14

As before the maximum particle size was found to be close to 10 nm.

The next interparticle energetic force to consider is the van der Waals attractive force, V_a. This force is the result of electric dipole-dipole forces. The equation for this force is

$$V_a = -\frac{A}{6}\left[\frac{2}{l^2+4l} + \frac{2}{(l+2)^2} + \ln\frac{l^2+4l}{(l+2)^2}\right]$$

Eq. 1.15

where A is the Hamaker constant, $l = 2\Delta_{ss}/d$, and Δ_{ss} is the surface-to-surface separation. The reported Hamaker constant for Fe_3O_4 varies from 0.34-2.3 x 10^{-19} N•m.[62] The Hamaker constant is affected by the dielectric constants of the medium and the material, in this case PDMS and magnetite. Some retardation effects due to separation distances also contribute to this factor.

For the case of particle-particle contact (l=0) the energy required to separate the two would be infinite. Therefore top priority should be given to prevent such contact. For ferrofluids this is typically accomplished via steric stabilization.[3]

Steric repulsion is the energy resulting from the physical interaction of molecules on the exterior of coated particles. These interactions are of high energy when particles are in close proximity but repulsion energy drops rapidly with distance. The steric repulsion energy, E_s, for neighboring spheres can be described by

$$\frac{E_s}{kT} = 2\pi d^2\varepsilon\left[2 - \frac{l+2}{t}\ln\left(\frac{1+t}{1+l/2}\right) - \frac{l}{t}\right]$$

Eq. 1.16

where $l = 2\Delta_{ss}/d$, $t = 2L/d$, ε is the surface concentration of adsorbed molecules, Δ_{ss} is the surface-to-surface separation between particles, L is the length of the adsorbed stabilizing layer, E_s is the repulsion energy per unit area, and d is the particle diameter.[3] Recently, other methods have described the interaction of polymeric spheres in solution. This will be addressed in the next section.

Combining all the energies results in a net interaction curve that can be used to predict the behavior of magnetic nanospheres in ferrofluids. Figure 1.5 illustrates the result of combining van der Waals attractions, magnetic attractions, and steric repulsion for 10-nm

diameter magnetite particles coated with either 0.5 or 2 nm thick brushes of oleic acid. One should note that dispersions of particles that have the more dense brush are predicted to be more stable.[3]

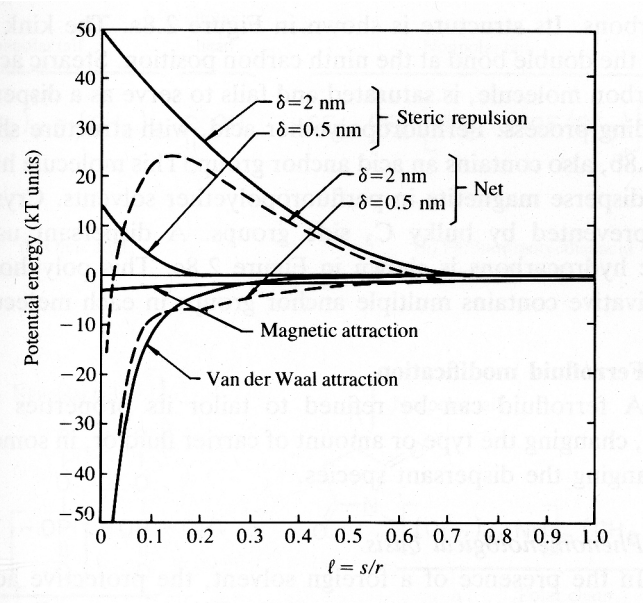

Figure 1.5: Potential energy versus surface-to-surface separation for sterically stabilized magnetite particles[3] [Reprinted with the permission of Cambridge University Press]

If predictions can be made of dispersion stability based on the core particle size and the coating thickness, the reverse should also hold true. The necessary thickness of the steric layer of a particle of known size that will produce stable dispersions can be calculated at given fields. Berkovsky et al. calculated the minimum coating layer thickness for magnetic particles of varying sizes with varying magnetic fields.[62] It was found that stronger fields require a thicker stabilizing layer to suspend the particles. If overall volume is held constant, this increased coating comes at a cost since the volume of the magnetic phase is diluted with stabilizer. This results in a decrease in the saturation magnetization, M_s, of the ferrofluid.[62] A careful balance must therefore be reached between the amount of carrier fluid, magnetic particles, and stabilizer.

1.5. Recent Advances in Calculating the Steric Interactions of Polymeric Particles

Many theories have been developed to quantify the interactions of polymer-coated particles. The first theories considered the coated particles as two flat plates, and described surface-to-surface interactions as the distance between the plates was changed.[63, 64] This interaction model was converted to a curved surface by the Derjaquin approximation.[65] Such a

model provided a convenient method for describing interactions between particles in which the ratio of brush thickness, L, to core radius, R_c was low $\left(\frac{L}{Rc} < 0.1\right)$. However, for the case of nanoparticles coated with polymers, $\frac{L}{R_c} \approx 1$. Thus, another model is necessary for describing steric particle-particle interactions in this case.

Recently, theories describing the interaction parameters for star-like polymeric micelles have been developed.[66, 67] This is an improvement over flat surface models, as chain density decays as one moves away from the surface due to curvature effects. In addition, by understanding this chain density decay, the physics of chain interpenetrations is better described.

This work is based on size characterization (DLS and SANS) of star-like micelles by Vagberg et al..[68] Vagberg's method for calculating the size of micelles was based on the 'blob model' devised by several authors.[69-71] The blob model (Figure 1.6) consists of a central spherical core in which polymer chains are anchored. Polymer chains extend out from the central core occupying spherical spaces known as blobs, where each layer contains the same number of blobs. The diameter of each blob, $\xi(r)$, increases as one moves away from the surface of the core. In addition, the density of each blob layer decreases with increasing size. The radius of the complex, R_m, is calculated by considering the number of blobs necessary for a chain to extend from the surface of the core. The length of the polymer brush, L, can be found by subtracting the core radius, R_c, from the radius of the complex, R_m.

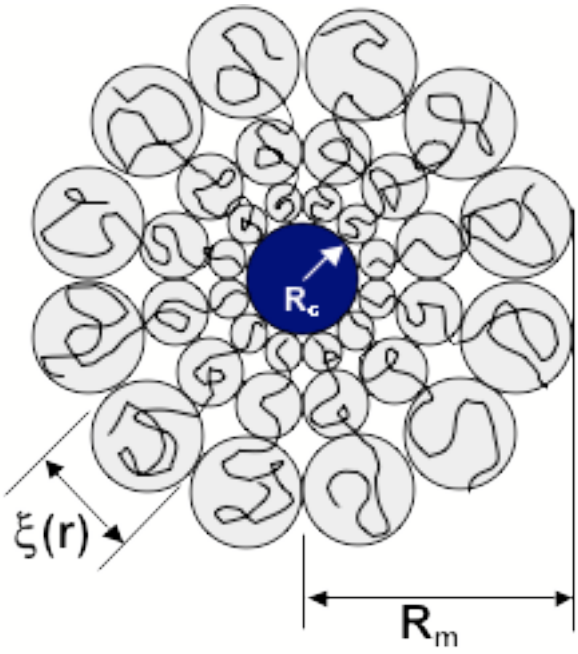

Figure 1.6: Cartoon of Blob Model, Adapated from Daoud and Cotton[71]

The particle interaction between two identical particles is calculated by considering the interaction to occur in two different situations. In the first case, the two particles are separated by a distance wherein the chains on the surface do not interpenetrate. In this scenario, the interaction parameter exponentially decays as the distance between the particles increases.[66, 67] In the second case, the chains of the two particles interpenetrate. The potential increases rapidly due to osmotic pressures predicted by Witten and Pincus.[69] Combining the interaction potentials in the two domains produces a uniform function where the interaction parameters for each domain are equivalent at the point of contact of the brushes.[66]

1.6. Principles of Rheology

A brief review of some principles of rheology is appropriate. The majority of rheological properties of ferrofluids are concerned with shear flow. Figure 1.7 shows an idealized parallel model for shear flow. A force is applied parallel to the medium in the x-direction.

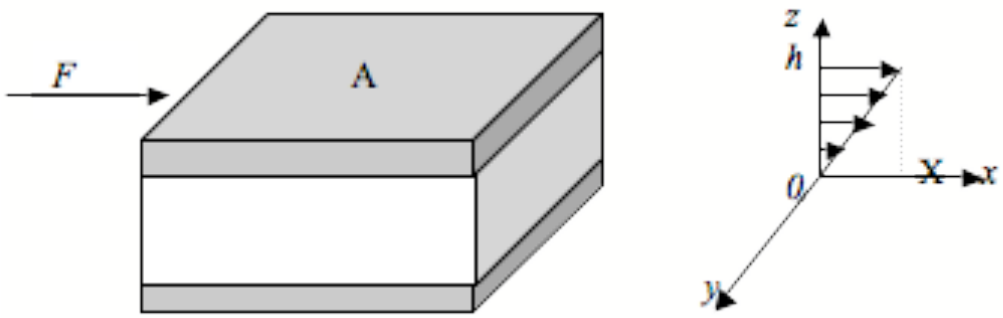

Figure 1.7: Ideal model for a parallel plate rheometer

Shear stress, σ, is defined as the force, F, over the area of the plate, A.

$$\sigma = \frac{F}{A}$$

Eq. 1.17

Shear strain, γ, can be described as the derivative of displacement, x, with respect to the z-direction.

$$\gamma = \frac{dx}{dz}$$

Eq. 1.18

The shear rate, $\dot{\gamma}$, can be described as the change in velocity, du, for a given change in height, dz.

$$\dot{\gamma} = \frac{du}{dz} = \frac{X}{h}$$

Eq. 1.19

Comparing shear stress to shear rate defines the viscosity, η:

$$\eta = \frac{\sigma}{\dot{\gamma}}$$

Eq. 1.20

The SI unit for viscosity is the Pascal-second (Pa.s). In some fields of study, the Poise (P) is commonly used. A Poise in 10 times smaller than a Pascal-second. Water at 20.2 ºC has a viscosity of 1 mPa.s (milliPascal-second) or 1 cP (centipoise). Table 1.2 gives the viscosities for some common materials.[72]

Table 1.2: Viscosities of common materials at room temperature[72] [Reprinted from Barnes, H. A.; Hutton, J. F.; Walters, K., *An Introduction to Rheology*. Elsevier: New York,1989.]

Liquid	Approximate viscosity (Pa.s)
Glass	10^{40}
Molten glass (500 °C)	10^{12}
Bitumen	10^{8}
Molten polymers	10^{3}
Golden syrup	10^{2}
Liquid honey	10^{1}
Glycerol	10^{0}
Olive oil	10^{-1}
Bicycle oil	10^{-2}
Water	10^{-3}
Air	10^{-5}

It is important to examine the rheology of polymer colloids in terms of dimensionless variables. Relative viscosity, η_r, is defined as the ratio of the colloidal suspension viscosity, η, to the viscosity of the dispersing agent, η_0.[73]

$$\eta_r = \frac{\eta}{\eta_0}$$

Eq. 1.21

1.7. Rheological properties of colloids

1.7.1. Volume Fraction

In the Annus Mirabilis of 1905, Einstein published his calculation of flow around a single sphere,[74]

$$\eta = \eta_s (1 + 2.5\phi)$$

Eq. 1.22

where η is the viscosity of the suspension, η_s is the viscosity of the solvent, and ϕ is the volume fraction of the suspended particles. This model assumes that there are no interparticle interactions, meaning that this only applies at low volume fractions ($\phi \leq 0.03$).

Batchelor expanded upon the finding of Einstein and added an additional term to describe the interaction between two spherical particles, altering the flow behavior of each other if they pass closely enough. These hydrodynamic interactions were combined with Einstein's calculations resulting in[75, 76]

$$\eta_r = \frac{\eta}{\eta_s} = 1 + 2.5\phi + 6.2\phi^2$$

Eq. 1.23

Comparison of the results of this equation to experimental findings indicates that this equation only applies in cases where $\phi \leq 0.10$.[77] As an alternative, Maclaurian developed a theorem to describe the relative viscosity of a colloidal suspension for a given volume fraction. Maclaurin's theorem is a series function where the coefficient, b_i, represents the *i*th derivative of the function evaluated at $\phi = 0$ and then divided by $i!$.[73]

$$\eta_r = 1 + [\eta]\phi + b_2\phi^2 + b_3\phi^3 \ldots$$

Eq. 1.24

The constants are difficult to determine in even the simplest of cases. The best result of this function was performed by Batchelor and Greene for polystyrene particles.[78] They were able to successfully calculate the value of b_2 to be 7.6. Unfortunately, calculating further values is an increasingly formidable task. Simply truncating the series and only using the value for b_2 results in poor predictions at higher volume fractions.[73]

Yet another alternative is to return to Einstein's equations, and expand the applicable volume fraction, ϕ, through an effective Arrhenius argument.[61] The assumption is made that for each time a small amount of particles, $d\phi$, is added, the particles are being added to a

homogeneous suspension with a viscosity, $\eta(\phi)$. In this case, a small change in viscosity, $d\eta$, can be defined by equation 1.25.

$$d\eta = 2.5\eta(\phi)d\phi$$

Eq. 1.25

Integration of the function results in

$$\eta = \eta_s e^{2.5\phi}$$

Eq. 1.26

The solution can be extended to account for particles of arbitrary shape:

$$\eta = \eta_s e^{[\eta]\phi}$$

Eq. 1.27

$[\eta]$ is the intrinsic viscosity with units of inverse volume fraction:

$$[\eta] = \lim_{\phi \to 0} \frac{\eta - \eta_s}{\phi \eta_s}$$

Eq. 1.28

At high ϕ this model is inaccurate, and this has been attributed to particle crowding. Ball and Richmond corrected this issue by including a maximum-packing volume fraction factor, ϕ_m in the equation.[79] For hard spheres this is typically between 0.63-0.64.[80]
The resulting equation is

$$d\eta = \frac{[\eta]\eta_s d\phi}{\left(1 - \frac{\phi}{\phi_m}\right)}$$

Eq. 1.29

Integrating this function yields

$$\eta = \eta_s \left(1 - \frac{\phi}{\phi_m}\right)^{-[\eta]\phi_m}$$

Eq. 1.30

Equation 1.30 is known as the *Krieger-Douugherty equation*.[81] Values for shapes other than spheres have been considered and tabulated by a number of scientists.[61, 72] While the values for ϕ_m and $[\eta]$ vary with the shape, the product of the two values, $\phi_m[\eta]$, remains fairly constant, only varying from ~1.4-3.[61]

An additional consideration is the effect of the suspending layer in these equations. A "bare" sphere has different properties compared to a sphere that is coated with a steric stabilizing agent. For volume fractions well below the maximum-packing volume fraction, ϕ_m, the assumption can be made that these particles behave similarly to "hard" spheres. The corrected volume fraction can be represented as

$$\phi = \phi_0 \left(1 + \frac{L}{R_c}\right)^3$$

Eq. 1.31

where ϕ_0 is the volume fraction of the "bare" particles, L is the thickness of the steric stabilizing layer, and R_c is the radius of the "bare" particle.[61, 82]

1.7.2. Shear Rate

Knowing the effects of volume fractions on viscosity is only a partial view of the rheological properties of colloids, and this is especially true for ferrofluids. The current model will be expanded to include the effects of shear rate. At higher shear rates, the interparticle spacing cannot remain in equilibrium due to an increase in kinetic energy. The mobility of particles in a suspension can be described by their diffusivities, D_0. For dilute suspensions, this is described by

$$D_0 = \frac{k_B T}{6\pi\eta_s r}$$

Eq. 1.32

where k_B is Boltzmann's constant, T is temperature in Kelvin, η_s is the viscosity of the solution, and r is the radius of the spheres.[61]

A variety of models describing the relationship between shear rate and viscosity can be considered. Polymeric suspensions behave as Newtonian fluids at low volume fractions. As the

volume fraction is increased, a more complex model for describing the flow behavior of suspensions is required.

One of the first non-Newtonian models proposed was the Bingham model. This model is able to approximate the relationship between the shear rate and stress, by incorporating what is known as a yield stress, σ_0.[72] The yield stress is defined as the point below which a material does not flow. Often materials demonstrating this type of behavior are referred to as Bingham plastics.[83]

$$\dot{\gamma} = \frac{\sigma - \sigma_0}{\eta_1}$$

Eq. 1.33

where η_1 is the limiting viscosity at high shear rates. Casson modified the Bingham model by taking the square root of the shear rate and other terms in equation 1.33, resulting in[84]

$$\dot{\gamma}^{\frac{1}{2}} = \frac{\sigma^{\frac{1}{2}} - \sigma_0^{\frac{1}{2}}}{\eta_1^{\frac{1}{2}}}$$

Eq. 1.34

This model is applicable to many polymeric colloidal materials that exhibit yield behavior.[73] However, for materials that flow at low shear rates this model is ineffective. An alternative that fits the flow of synthetic rubber latexes is the Ostwald de Waele "power law",[85]

$$\dot{\gamma} = a\sigma^n$$

Eq. 1.35

where, "a" is a coefficient which is equivalent to the viscosity at unit shear stress, and n is an exponential. Other models have been developed to more accurately describe the shear thinning observed in some systems. One equation accounts for Newtonian flow of the carrier fluid by one component and the spheres by another component.[86]

$$\eta = \eta_1 + (\eta_2 - \eta_1)\frac{\sinh^{-1}(\beta\dot{\gamma})}{\beta\dot{\gamma}}$$

Eq. 1.36

where η_2 is the low shear limiting viscosity, and β is the relaxation time. This model is effective because it has Newtonian regions at both high and low shear rates. A similar type of behavior was observed by Dougherty and Krieger.[81, 87]

$$\eta = \eta_1 + \frac{\eta_2 - \eta_1}{1 + |\sigma| / \sigma_c}$$

Eq. 1.37

where σ_c is a critical shear stress. Cross offered a similar equation, but altered it slightly by adding an additional parameter, n, which normally takes on values from $\frac{2}{3}$ to 1.[88]

$$\eta = \eta_1 + \frac{\eta_2 - \eta_1}{1 + \left(\dot{\gamma} / \gamma_c \right)^n}$$

Eq. 1.38

Finally, Carreau offered one more variation upon this relationship, by altering the denominator of equation 1.38 (equation 1.39).[89]

$$\eta = \eta_1 + \frac{\eta_2 - \eta_1}{\left(1 + \left(\dot{\gamma} / \gamma_c \right)^2 \right)^{n/2}}$$

Eq. 1.39

1.7.3. Shear Thickening

As shown by shear thinning, if the substructure of a suspension is disturbed, major changes in the viscosity can be observed. Just as substructures can be broken down by shear stress, microstructures can also develop due to shear stress. Typically an increase in viscosity is observed with increasing shear rate, followed by shear thinning of the material. Factors that contribute to shear thickening include volume fraction, the particle size distribution, and the viscosity of the carrier fluid.[72]

1.7.4. Shear History

For materials that display a small degree of flocculation, the shear history can play a critical role in the manner in which they flow under shear stress. For example, consider a

suspension of silica particles suspended in a polydimethylsiloxane carrier fluid. These particles are close to 10 nm in diameter but form some agglomerates up to one μm in size. Shear history can alter when the viscosity of a filled medium. This phenomenon is referred to as thixotrophy, and is characterized by a long relaxation rate.[61]

1.7.5. Magnetic Field Effects

When a magnetic field is applied to a ferrofluid, it can undergo shear deformation. If the field is parallel to the direction of fluid flow, then the particles can freely rotate and effects of magnetization are minimized. However if the field is orthogonal to the direction of flow, the effects are maximized.[3] This relationship was investigated by McTague by measuring the viscosities of dilute suspensions of polymer-stabilized cobalt particles in toluene flowing through a capillary tube (Poiseuille flow). Measurements were made when the field was perpendicular and parallel to the direction of flow. In both cases there was an increase in the viscosity of the fluid. Also in both cases the materials showed an increase with the Langevin argument α, before reaching a final saturation.[90] It was observed that the increases in viscosity with the field direction perpendicular to the flow were approximately twice those of the parallel field cases.[3, 91, 92]

2. Field Induced Motion of Ferrofluids through Immiscible Viscous Media: Testbed for Restorative Treatment of Retinal Detachment

O.Thompson Mefford,[a] R.C. Woodward,[b] J.D. Goff,[a] T.P. Vadala,[a] T.G. St. Pierre,[b] J.P. Dailey,[c] and J.S. Riffle[a]

[a]Macromolecules and Interfaces Institute, Virginia Tech, Blacksburg, Virginia 24061, [b]School of Physics, The University of Western Australia, Crawley, Western Australia 6009, Australia, [c]NanoMedics, Inc., Erie, PA 15607

Published by Elsevier In: *Journal of Magnetism and Magnetic Materials*, 311 (1), p.347-353, Apr 2007

2.1. Abstract

Biocompatible, hydrophobic ferrofluids comprised of magnetite nanoparticles dispersed in polydimethylsiloxane show promise as materials for treatment of retinal detachment. This paper focuses on the motion of hydrophobic ferrofluid droplets traveling through viscous aqueous media, whereby the movement is induced by gradients in external fields generated by small permanent magnets. A numerical method was utilized to predict the force on a spherical droplet, then the calculated force was used to estimate the time required for the droplet to reach the permanent magnet. The calculated forces and travel times were verified experimentally.

Keywords: ferrofluid, magnetite, polydimethylsiloxane, retina

2.2. Introduction

We have worked for several years to develop biocompatible polysiloxane ferrofluids for treating retinal detachment [14-16, 93, 94]. Retinal detachment is a leading cause of blindness, and currently available treatments fail in as many as 1/3 of complicated retinal detachment patients, resulting in partial or complete loss of vision for several million people worldwide. A retinal tear provides a pathway for vitreous fluid to pass through and underneath the retina, thus detaching the retina from the choroid. The goal of surgery is to close any holes in the retina, preventing further fluid flow into the sub-retinal space, allowing for reattachment of the retina.

The proposed treatment (Figure 2.1) requires synthesizing magnetic nanoparticles and complexing them with a functionalized polysiloxane, then dispersing the complex in a non-functional polysiloxane oligomer to form the ferrofluid. The fluid can be injected through a fine needle into the vitreous cavity of the eye in apposition to a tiny permanent magnet inserted just

beneath Tenon's capsule on the outside of the scleral wall of the eye. The polysiloxane fluid is hydrophobic and has a high interfacial tension against the vitreous gel, and thus a stable spherical ferrofluid droplet forms within the aqueous. The permanent magnet attracts the ferrofluid droplet toward the side of the eye, and it is anticipated that the droplet can then seal a retinal hole.

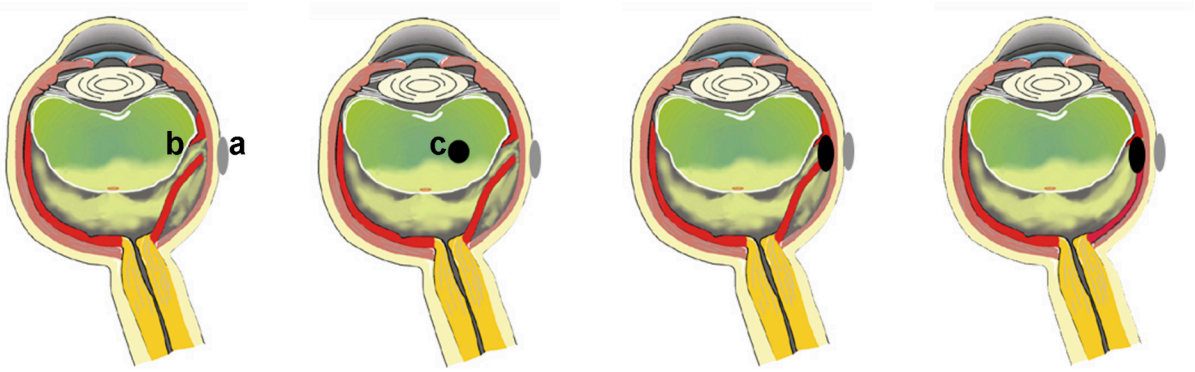

Figure 2.1: Proposed procedure for treating a retinal detachment: 1) A permanent magnet (a) with a pre-aligned magnetic field is placed in the conjunctiva proximal to the site of the retial detachment (b), 2) a ferrofluid droplet (c) is injected into the vitreous humor, 3) attracted to the permanent magnet, the ferrofluid closes the hole in the retina, and 4) the body absorbs the liquid that has accumulated underneath the retina.

Understanding the motion of a ferrofluid droplet as it travels in the eye is important for the success of this procedure. The permanent magnet on the exterior of the eye should generate a magnetic field of sufficient strength to pull the ferrofluid droplet to the retinal tear in a reasonable amount of time. The droplet volume must also be considered, as it will likely affect the size of the hole that can be sealed, as well as the overall motion of the droplet. Mathematical models for the motion of ferrofluids have been described by Shliomis [95-100] and Felderhof.[101-103] Others have investigated the use of gradient fields for positioning ferrofluids in microfluidic,[104] capillary,[105] and controlled rheological systems.[106-108] Rinaldi et al. have published an excellent review on this subject.[109]

The intention of this research has been to demonstrate the control of polysiloxane ferrofluid motion through a viscous aqueous medium. Fundamental magnetic properties of the ferrofluid, mathematical calculations of the forces applied to ferrofluid droplets by an external permanent

magnet, and simulations of the mobility of a ferrofluid droplet as it travels through the medium will be described.

2.3. Experimental

2.3.1. *Materials*

Hexamethylcyclotrisiloxane (D_3, Gelest) was dried over calcium hydride and sublimed under vacuum into pre-weighed, flame-dried, roundbottom flasks, each containing a magnetic stirring bar. The flasks were purged with argon and re-weighed to determine the amount of D_3 in each flask. Cyclohexane (EM Science, 99%) was stirred with concentrated sulfuric acid for one week, washed with deionized water until neutral, stirred over calcium hydride, distilled, stored over sodium under a nitrogen atmosphere, and distilled prior to use. Tetrahydrofuran (THF) (EM Science, 99.5%) was dried over calcium hydride, distilled, stored as the purple sodium/benzophenone dispersion under nitrogen, and distilled just prior to use. Toluene (Burdick and Jackson, 99.9%) was distilled from calcium hydride and deoxygenated by purging with dry nitrogen prior to use. Hydrochloric acid solution was prepared by adding 5 mL of concentrated hydrochloric acid (37 wt% in water, EM Science) to 5 mL of deionized water. Ferric chloride hexahydrate ($FeCl_3 \cdot 6H_2O$) and ferrous chloride tetrahydrate ($FeCl_2 \cdot 4H_2O$), both from Aldrich, were stored under nitrogen in a desiccator and used as received. Ammonium hydroxide (Alfa Aesar, 50% v/v aqueous), mercaptoacetic acid (97%, Aldrich), 2,2'-azobisisobutyronitrile (AIBN, 98%, Aldrich), n-butyllithium (2.0M, Aldrich), trivinylchlorosilane (Gelest), trimethylchlorosilane (Gelest), MQP-B NdFeB powder (kindly donated by Magnequench, Toronto, Canada), Provisc™ solution (Alcon Inc., generously supplied by the Lion's Eye Institute, Nedlands, WA, Australia), and Tarzan's Grip® (Selleys Pty Ltd) general purpose clear cyanoacrylate adhesive were used as received.

2.3.2. Ferrofluid Synthesis

The methods for synthesizing the ferrofluid components have been previously reported.[94] The ferrofluid utilized in the present work was comprised of magnetite nanoparticles complexed with a carboxylate-functional polydimethylsiloxane (PDMS) (Figure 2.2), and this complex was dispersed in a 5000 g mol^{-1} PDMS carrier fluid. The complex contained 50 wt% of magnetite and 50 wt% of the PDMS dispersant, and this complex was combined with the carrier fluid (50

wt% complex:50 wt% carrier fluid), yielding a ferrofluid that contained 25 wt% magnetite. A brief synthetic procedure is described.

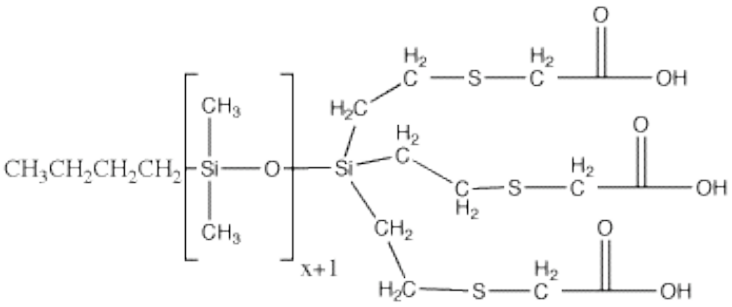

Figure 2.2: Tricarboxylic acid terminated PDMS used to stabilize magnetite nanoparticles.

The PDMS dispersion stabilizer having three carboxylic acid groups at one end was prepared by first subliming D_3 (27.44 g) into a septum-sealed, flame-dried, roundbottom flask. The flask was purged with nitrogen, and cyclohexane (30 mL) was added via a syringe to dissolve the D_3. The *n*-butyllithium initiator (3.5 mL of a 2.5M solution, 8.75 x 10^{-3} mol) was added to the reaction, and the solution was stirred at 25 ^{o}C for one h. THF (10 mL) was charged to the solution as a reaction promoter, and the polymerization was conducted at 25 ^{o}C. ^{1}H NMR was utilized to monitor the progress of the living anionic polymerization. The polymer was terminated by adding excess trivinylchlorosilane (2.2 mL, 0.0142 mol) at ~70-80% conversion and allowing the mixture to stir overnight. The excess trivinylchlorosilane was removed under vacuum, then the product was precipitated by pouring into methanol. The PDMS oligomer was diluted with chloroform, washed three times with deionized water, the chloroform was removed, and the polymer was dried under vacuum at 80 ^{0}C overnight. The synthetic procedure for the 5000 g mol^{-1} PDMS carrier fluid was similar to the one outlined above, except the living anionic polymerization was terminated with trimethylchlorosilane.

The thiol-ene addition of mercaptoacetic acid to the trivinyl-terminated PDMS oligomer was as follows. A 2500 g mol^{-1} trivinylsiloxy terminated PDMS (12.3 g, 0.0148 equiv vinyl) was added into a flame-dried, roundbottom flask and dissolved in toluene (60 mL). Argon was bubbled through the solution for approximately two h to deoxygenate the reaction mixture. AIBN (0.0035 g, 0.0213 mmol) and mercaptoacetic acid (1.39 mL, 0.0200 mol) were added to the reaction vessel, and the flask was purged with argon. The reaction was heated to 80 ^{0}C and stirred for one h. Reaction completion was confirmed by observing the disappearance of the vinyl proton peaks at δ 5.8-6.2 ppm in the ^{1}H NMR spectrum. The solvent was removed under

vacuum, and the polymer was dissolved in methanol and stirred for 30 min. Deionized water was added to the solution until the polymer coagulated. The methanol/deionized water coagulation process was repeated five times, and the polymer was dried under vacuum at 80 ^{0}C.

Synthesis of the magnetite nanoparticles and subsequent adsorption of the carboxylate-functional PDMS stabilizer onto the magnetite nanoparticle surfaces was achieved as follows. The composition was adjusted so that the final complex contained 50 wt% of magnetite and 50 wt% of the PDMS stabilizer. Magnetite nanoparticles were prepared using a chemical co-precipitation of iron salts. Iron (III) chloride hexahydrate (2.01 g, 7.44 mmol) and iron (II) chloride tetrahydrate (0.736 g, 3.70 mmol) were weighed into separate roundbottom flasks and each was dissolved in 20 mL of deoxygenated water. The two iron salt solutions were added to a 500-mL, three-necked, roundbottom flask fitted with an overhead stirring apparatus and a pH electrode. Ammonium hydroxide solution (~15 mL) was added via syringe until the rapidly stirring solution turned black and reached a pH of 9-10. The PDMS dispersion stabilizer (0.9 g) was dissolved in dichloromethane (20 mL) and the solution was added to the basic, aqueous, magnetite dispersion. After stirring for 30 min, aqueous HCl (~18.5 wt% HCl in water) was added slowly until the solution became slightly acidic (~ 6 mL was required to reach pH 5-6). The heterogeneous dispersion was stirred for 1 h, and then the dichloromethane was removed under vacuum. The magnetite complex was collected with a magnet and the water was decanted. The PDMS-magnetite complex was washed five times with water, five times with methanol, then dried overnight at 40 ^{0}C under reduced pressure.

To prepare the ferrofluid, a 5000 g mol^{-1} PDMS oligomer having trimethylsilyl endgroups (2 g) and the PDMS stabilizer-magnetite complex (2 g, 50 wt% PDMS and 50 wt% magnetite) were added to a scintillation vial. Chloroform (20 mL) was added to the vial. Once the carrier fluid and complex were dissolved, the dispersion was sonicated with a Biologics ultrasonic homogenizer (model 150V/T) for 15 min using the full power setting on a micro-tip probe and a 50% pulse. After sonication, the chloroform was removed under reduced pressure, yielding a PDMS-magnetite ferrofluid.

2.3.3. Ferrofluid Characterization

Samples of ferrofluid were sealed in pre-weighed polycarbonate sample chambers and placed in a Quantum Systems MPMS SQuID magnetometer. The magnetization of the ferrofluids was

measured between +70000 and -70000 Oe at room temperature. The density of the ferrofluid was determined by weighing the mass of the fluid in a sample chamber of known volume.

2.3.4. Preparation and Characterization of the Permanent Magnet

NdFeB powder was dispersed into a cyanoacrylate adhesive (80/20 wt/wt powder/adhesive), and the mixture was pressed into rectangular Teflon molds that were 5mm deep, 5mm wide, and 20 mm long. The samples were cured overnight at 25 ^{o}C in air. While still in the mold, the samples were placed in a 12 Tesla field to magnetize the magnet with the field direction perpendicular to the thickness of the magnet. The magnets were removed from the molds and the fields generated by the magnets were measured with a Hall probe every 1 mm from the center of the surface of the magnet to 30 mm away along the axis of magnetization. The data was fitted with a 5th order polynomial.

2.3.5. Measurement of magnetic force via a load cell

The fields from an electromagnet at 1, 2, and 3 amps of current were measured with a Hall probe as described for the permanent magnet. A 0.0304 g sample of ferrofluid was then placed on a top-loading electronic microbalance [Metler Toledo AB54]. A low weight spacer was placed between the sample and the balance to ensure that the magnetic fields from the electromagnet did not affect the performance of the balance. The electromagnet was placed 5, 9, 16, and 20 mm above the ferrofluid and the weights of the ferrofluid at each distance with 0, 1, 2, or 3 amps of current passing through the electromagnet were recorded. The magnetic forces (F_m) were determined by applying the acceleration due to gravity to the weight differences with and without the electromagnetic field:

$$F_m = \left(9.8 \tfrac{m}{s^2}\right)\left(wt_{in\ field} - wt_{without\ field}\right)$$

Eq. 2.1

2.3.6. Time-lapse photography of ferrofluid motion through a viscous medium

To test the accuracy of the numerical calculations, time-lapse photography was used to observe the motion of ferrofluid droplets through a viscous medium. An experiment was devised to approximate conditions within an eye. Hollow glass spheres, with 22 mm inner diameter and 24 mm outer diameter, were charged with Provisc™ (sodium hyaluronate) solution, a

"viscoelastic" commonly used in eye surgery, which has a viscosity of ~50 Pa s. Droplets of ferrofluid were introduced into the center of the glass sphere. The mass increase resulting from the ferrofluid was measured with a microbalance, and the droplet volume was calculated based on the density of the fluid assuming that the droplet was spherical. A permanent magnet was placed on the side of the sphere. Photographic images were taken every 15 s as the droplet moved from the center to the side of the glass sphere.

2.4. Theory

The magnetic force, F_M, acting on an object is given by [110]

$$\mathbf{F}_M = \mu_0 \nabla (\mathbf{m} \bullet \mathbf{H})$$

Eq. 2.2

where m is the magnetic moment of the object, μ_0 is the magnetic permeability of free space and H is the magnetic field. A number of assumptions were made to simplify the analyses. We assumed a point dipole approximation, where the magnetization of the droplet was along the field direction and only gradients in the field direction (x direction) were considered. In this case the magnetic force acting on a spherical droplet traveling through a uniform aqueous medium towards a permanent magnet on the exterior of the eye can be simplified to

$$F_M(x) = V * M(x) * \mu_0 * \frac{dH}{dx}$$

Eq. 2.3

where V is droplet volume, M is the magnetization of the PDMS ferrofluid droplet, and dH/dx is the gradient of the magnetic field, H, with respect to distance, x, from the permanent magnet.

If the magnet is sufficiently large, then the field generated by the permanent magnet as a function of distance from its surface, H(x), can be measured with a Hall probe. SQuID magnetometry was utilized to measure the magnetization of the ferrofluid as a function of the applied magnetic field (M(H)). By substituting H(x) in M(H), the magnetization of the droplet can be defined in terms of its distance from the permanent magnet, M(x). The result can be utilized to calculate the force generated by the permanent magnet on the PDMS droplet as a function of its distance from the permanent magnet.

The motion of a ferrofluid droplet through the vitreous humor will be opposed by viscous drag. If we assume that the droplet maintains a spherical shape, then the viscous drag force, F_D, on a droplet with radius, r, moving through an immiscible fluid with a velocity, U, and a viscosity, η, can be described by the generalized Stokes equation:

$$F_D = 6r\pi\eta U$$

Eq. 2.4

Solving for velocity yields:

$$U = \frac{F_D}{6r\pi\eta}$$

Eq. 2.5

To calculate steady state velocity, the magnetic force, F_M, can be equated to the drag force, F_D, from Eq. 2.3 and Eq. 2.4 respectively, which leads to an expression for the steady state velocity:

$$U(x) = \frac{F_M(x)}{6r\pi\eta}$$

Eq. 2.6

For a highly viscous medium, the time required for the droplet to accelerate to the steady state velocity is relatively insignificant. Thus, the assumption that the droplet always moves at the steady state velocity was invoked. Knowing the velocity, the time required for the droplet to travel from a point in the viscous medium to the permanent magnet can be estimated. Since U(x) gives the velocity at a point in space, integration across the distance to be traveled, Z, results in the time required for travel to the permanent magnet.

$$time = \int_0^Z \frac{1}{U(x)} dx = \int_0^Z \frac{6r\pi\eta}{F_M(x)} dx$$

Eq. 2.7

2.5. *Results and Discussion*

A series of experiments was conducted to understand the behavior of the PDMS ferrofluid in gradient magnetic fields. Magnetic moments measured by SQuID magnetometry were converted

to units of magnetization by dividing by the volume of ferrofluid in the sample chamber (converting from Am^2 to A/m) (Figure 2.3). The density of the ferrofluid was determined to be 1.32 g/mL. The SQuID data was fitted with a Langevin function to describe the magnetization, M, in terms of the field, H.

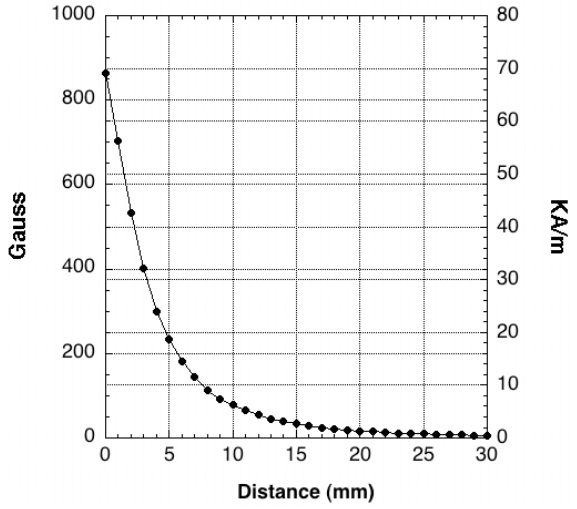

Figure 2.3: Field map around a 5mm thick by 5 x 20mm bar magnet containing 80 wt% NdFeB powder.

A permanent magnet was prepared from NdFeB powder in a polycyanoacrylate network. The moments of the NdFeB particles were aligned in a 12T field, and the resulting magnetic field generated by the permanent magnet was mapped with a Hall probe. This data was fitted with a 5^{th} order polynomial to mathematically describe the field, H, in terms of distance from the magnet, x (Figure 2.3). The field gradient dH/dx was found by differentiating this equation. The polynomial curves from the Hall probe measurements were combined with the Langevin fit function from the SQUID measurements on the ferrofluid to yield the magnetization as a function of distance from the magnet. The resulting expression was substituted into Equation 3 to provide a function for the force on a droplet of known volume resulting from a permanent magnet at a known distance, x, from the droplet. This expression was utilized to calculate the forces exerted on a 1-mm diameter droplet of ferrofluid (Figure 2.4).

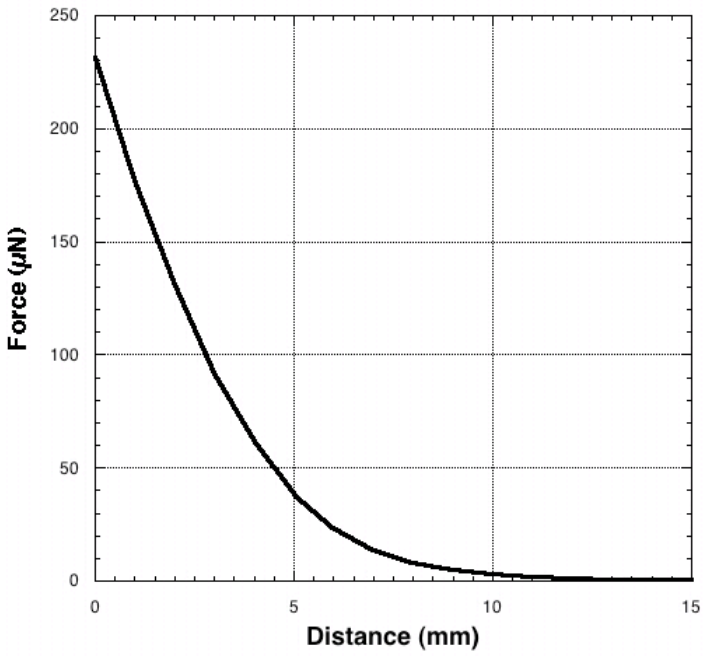

Figure 2.4: Calculated force on a 1-mm diameter droplet of ferrofluid generated from a 5mm thick by 5 x 20mm bar magnet containing 80 wt% NdFeB powder with the magnetic field through the thickness.

Experiments were designed to verify the calculations of forces imposed on the ferrofluids. A ferrofluid was placed on a balance and an electromagnet was positioned above the ferrofluid. When the magnetic field was applied, the mass read by the balance was reduced due to the upward force on the ferrofluid generated by the electromagnet. The magnetic forces were determined by subtracting the force due to gravity from the total forces. At low currents (low fields), the magnetic forces derived from the numerical method matched experimental results, but the method over-predicted the forces at higher currents (Figure 2.5). Based on magnets suitable for the given application to eye surgery, we anticipate that forces only up to ~200 μN (10 mm from the magnet) will be required to attract the ferrofluid droplet to the magnet (within about 10 minutes). Thus, it was reasoned that predictions of the magnetic force imposed on these ferrofluids by an external magnet are possible using the simplified expression (Eq. 2.3).

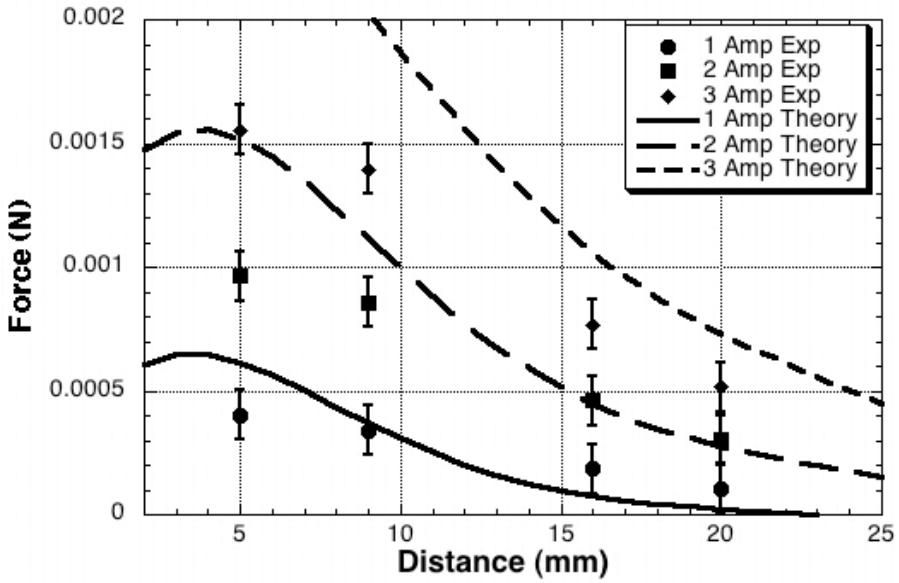

Figure 2.5: Theoretical magnetic forces exerted on a ferrofluid compared to experimental values at 1, 2, and 3 amps of current passing through the electromagnet.

The amount of time required for a ferrofluid droplet to travel through a viscous medium to a permanent magnet was approximated based on the force calculations. By assuming a steady state velocity, the drag force was equated to magnetic force, resulting in a function for the velocity at a given distance from the magnet (Eq. 2.6). The reciprocal of the velocity function was integrated to estimate the time required for a spherical droplet to travel through the aqueous medium. Travel times were calculated for a series of droplets of varying diameters moving through an aqueous medium with a viscosity of 50 Pa•s (Figure 2.6). This viscosity was selected because it is similar to the viscosities of fluids used as replacements for the aqueous humor in the eye. As expected, the estimated travel times indicate that larger droplets travel faster than smaller droplets. In addition, the velocity increases as the droplet moves closer to the magnet. Based on these predictions, the position at which the droplet would be introduced into the eye in relation to the position of the permanent magnet is important. For example, if the surgeon injects a 2-mm diameter droplet of ferrofluid 12 mm away from the side of the eye it would take approximately twice as long to travel compared to a droplet placed 10 mm away from the side of the eye.

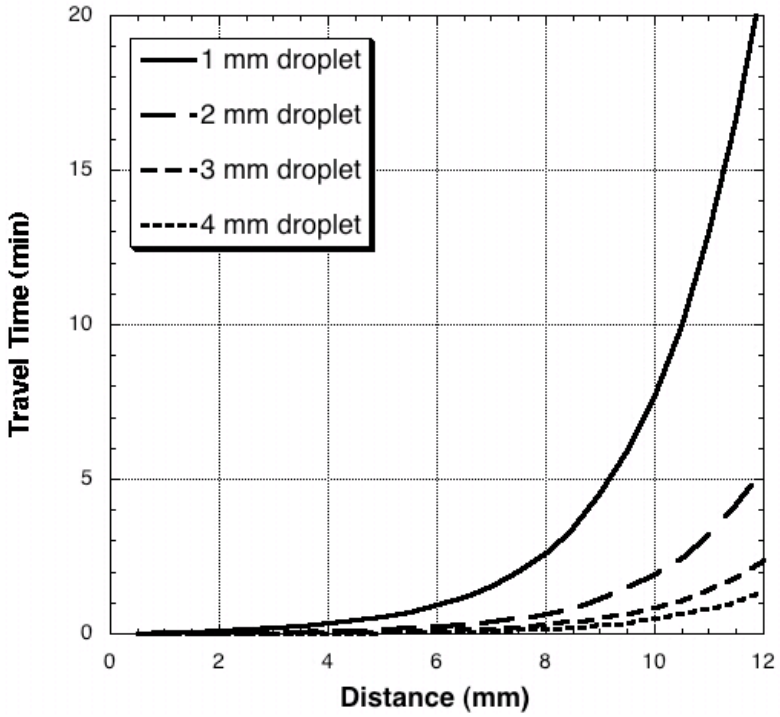

Figure 2.6: Calculated travel times for different diameter droplets through a aqueous medium with a viscosity of 50 Pa s to a 5mm thick by 5 x 20mm bar magnet containing 80 wt% NdFeB powder with the magnetic field through the thickness.

As a comparison to calculated travel times an experiment was devised to simulate the environment of the eye. Glass spheres were filled with Pro-visc™ aqueous solution to represent the eye. The permanent magnet was placed on the outside of the glass, and a droplet of ferrofluid was injected into the center of the sphere. The travel time of the droplet was recorded and compared to the numerical calculations (Table 2.1). Higher velocities of larger droplets were clearly demonstrated. The measured times were consistently shorter than those estimated by the theoretical model. The most likely reason for this systematic difference is the assumption that the droplet acts as a magnetic dipole located at the center of the droplet. Due to the field gradients in the system, the effective position of the dipole will be displaced towards the magnet and hence the resulting magnetic forces will be larger than those predicted by the current model.

Table 2.1: Theoretical vs. experimental travel times for different droplet sizes

Diameter of Droplet (mm)	Travel Distance (mm)	Theoretical Time (min)	Experimental Time (min)
1.0	12	21.2	15.0
1.8	12	6.6	4.0
2.0	11	3.2	2.5

Several interesting effects were observed in the images captured by the time-lapse photography that have not yet been considered in the calculations. At larger droplet sizes, the droplet shape deforms from a sphere to a teardrop as it moves through the viscous medium toward the magnet. In addition, as the droplet accelerates towards the magnet, separation of the tail of the teardrop was sometimes observed. This results in smaller droplets, which require longer travel times to the permanent magnet, and could potentially occlude vision.

2.6. Conclusions

While the droplets may change shape and break up, the numerical method for estimating the travel times is sufficiently accurate to provide an upper bound to the travel time. The calculated forces imposed on the droplets by small magnets predict that travel times of seconds to minutes should be possible in a clinical environment. Moreover, the numerical method can be utilized as an aid for the future design of magnets with appropriate sizes and strengths. All of these results show promise for the proposed treatment of retinal detachment.

More advanced modeling is required to integrate the forces over the total volume of the particle and to investigate the deformation of larger droplets. Both variation of forces within the droplet and hydrodynamic shear stress from the viscous medium may contribute to deformation of the droplet. The portion of the droplet closest to the magnet experiences a greater force than the section further away. This difference is likely a factor contributing to droplet shape change. Continuing work will include shear thinning of the droplet as it accelerates, as well as variance in the magnetic forces within the droplet.

2.7. Acknowledgements

The authors are grateful for the financial support of the Orris C. and Beatrice Dewey Hirtzel Memorial Foundation, the Lord Foundation, the NSF Materials World Network for the Study of Macromolecular Ferrofluids, the National Eye Institute of the NIH under SBIR contract B6867G1, and the ARC Discovery Grant - DP0559333.

3. Size Analysis of PDMS-Magnetite Nanoparticle Complexes: Experiment and Theory

O.Thompson Mefford,[a] M. R. J. Carroll,[c] M. L. Vadala,[b] J. D. Goff,[a] R. Mejia-Ariza,[a] M. Saunders,[d] R. C. Woodward,[c] T. G. St. Pierre,[c] R. M. Davis[a] and J. S. Riffle[a]

[a]Macromolecules and Interfaces Institute, Virginia Tech, Blacksburg, VA 24061
[b]Nanomedics LLC, Erie, PA, 16509
[c]School of Physics, The University of Western Australia, Crawley, Western Australia 6009, Australia
[d]Center for Microscopy Characterisation and Analysis, The University of Western Australia, Crawley, Western Australia 6009, Australia

3.1. Abstract

Biocompatible, hydrophobic nanoparticles show great promise as biomaterials. This paper reports the synthesis, magnetic separation, and characterization of magnetite nanoparticles with polydimethylsiloxane (PMDS) adsorbed onto their surfaces. Particle size distributions were varied by employing a magnetic separation/fractionation technique to remove larger particles and aggregates from an original distribution. The size distribution of the magnetite cores were analyzed by transmission electron microscopy (TEM), and sizes of the complexes in solution were measured by dynamic light scattering (DLS). A probability averaging method based on TEM data is proposed, together with implementation of a polymer brush model for calculating the thickness of the polymer surfactant, for predicting the sizes and distributions of these complexes in suspension. Specifically, the intensity, volume and number averages have been calculated, and the values were compared to sizes of the complexes measured by DLS. This approach provides a tool for a more precise characterization of the size distributions of polymer-nanoparticle complexes, relative to previous methods that utilized only a mean (single) core particle size. The calculated values of the sizes of the complexes closely approximate measured values from DLS for particles of narrow size distribution. Agreement between the predicted and measured sizes improves as the particle size distribution becomes more narrow.

3.2. Introduction

Magnetic nanoparticles show great potential in a variety of biomedical applications. They have been demonstrated to have exceptional properties for MRI contrast enhancement, drug targeting and delivery, hyperthermia treatment, and magnetic separation of bioagents.[12, 13] In

addition, we have worked for several years to develop hydrophobic ferrofluids for the treatment of retinal detachment.[14-18]

Magnetite nanoparticles were first produced in the 1960's by grinding iron oxides with surfactants and long chain hydrocarbons.[22] This was followed by the development of precipitation techniques utilizing the reaction of soluble iron salts with base.[111, 112] This method has been employed to create magnetite particles functionalized with a gamut of materials including water soluble polymers such as dextran[113] and poly(ethylene oxide),[28, 114] to nonpolar materials such as polystyrene and poly(methyl methacrylate).[115] Other techniques have also proven successful for synthesizing magnetite nanoparticles. These include the use of microelmulsions (i.e., reverse micellar solutions),[116-118] polyol reductions,[119, 120] and elevated temperature decompositions of organic precursors.[37, 121] Both Tartaj et al. and Harris et al. have presented reviews of these techniques.[13, 122]

Magnetic separations have been explored for several decades. For instance, Watson described the removal of micron-sized paramagnetic particles with stainless steel wool in applied fields from 0.1 - 0.15 Tesla.[123] This approach has been utilized by many researchers as it offers simplicity and a low cost/high throughput approach[124] that has recently been employed for separations of tagged cells. Sarikaya et al. have presented an excellent review of the design parameters (e.g., flow rate and strength of the applied field) for this type of particle separation in aqueous media.[125] An alternative to this technique is magnetic field-flow fractionation (MFFF). This method separates particles into various fractions due to the particles' individual magnetic moment.[35, 124, 126-129]

In this work, magnetite nanoparticles with terminally attached PDMS chains bound to their surfaces for sterically stabilizing the nanoparticles against flocculation were synthesized. The sizes and the size distributions of the particles were adjusted by magnetically removing larger particles and aggregates via magnetic separation. This was achieved by passing dispersions of the particles through columns packed with granules of soft magnetic material. Characterization of the magnetite-PDMS complexes, and their size distributions and properties will be discussed along with calculations of the polymer brush thicknesses and the hydrodynamic radii of the complexes in dispersions.

This work outlines a general methodology for characterizing metal oxide particles that are sterically stabilized with polymer brushes even when the particle size distribution is not

narrow. Nanoparticles to be utilized in a myriad of applications are typically polydisperse. For biomedical applications, sterically stabilizing polymer layers are frequently needed which can alter size due to brush thickness. It is important to quantify the full size distributions of complexes for controlling drug delivery, dosage, cell uptake, and renal clearance. In addition, it is believed that size distributions of MRI contrast agents will be important for understanding and enhancing their effectiveness.

3.3. Experimental

3.3.1. Materials

Hexamethylcyclotrisiloxane (D_3, Gelest, Inc., 98 %) was dried over calcium hydride and sublimed under vacuum into pre-weighed, flame-dried, roundbottom flasks, each containing a magnetic stir bar. The flasks were purged with nitrogen and re-weighed to determine the amount of D_3 in each flask. Cyclohexane (EM Science, 99%) was stirred with concentrated sulfuric acid for 48 h, washed with deionized water until neutral, stirred over magnesium sulfate, then over calcium hydride, distilled, stored over sodium under a nitrogen atmosphere, and distilled prior to use. Tetrahydrofuran (THF) (EM Science, 99.5%) was dried over calcium hydride, distilled, and stored over sodium in the presence of benzophenone under a nitrogen atmosphere until the solution was a deep purple. The THF was distilled just prior to use. Toluene (Burdick and Jackson, 99.9%) was washed twice with concentrated sulfuric acid and neutralized with water. It was dried over magnesium sulfate for 1 h, then over calcium hydride overnight and distilled just before use. Aqueous hydrochloric acid (50% by volume) was prepared by adding 5 mL of concentrated hydrochloric acid (EM Science) to 5 mL of deionized water in a graduated cylinder. Ferric chloride hexahydrate ($FeCl_3 \cdot 6H_2O$) and ferrous chloride tetrahydrate ($FeCl_2 \cdot 4H_2O$) (both from Aldrich) were stored under nitrogen in a desiccator and used as received. Iron granules (Alfa Aesar, 1-2 mm, 99.98%) were washed repeatedly with a variety of solvents to remove any coating on the surface. The granules were subsequently dried overnight in a vacuum oven at 40 ºC. Ammonium hydroxide (Alfa Aesar, 50% v/v aqueous), mercaptoacetic acid (Aldrich, 97%), 2,2'-azobisisobutyronitrile (AIBN, 98%, Aldrich), n-butyllithium (1.6 M, Aldrich), trivinylchlorosilane (Gelest, Inc., 95%), and trimethylchlorosilane (Gelest, Inc., 99%) were used as received. NdFeB doughnut-shaped magnets that were magnetized through the thickness were purchased from Engineered Concepts. The field generated by the doughnut magnets was 0.24 T,

and the magnets had dimensions of 1.0 in (2.54 cm) I.D., 0.5 in (1.27 cm) O.D, and 0.25 in (0.635 cm) thick.

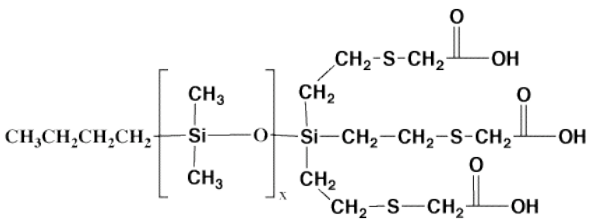

Figure 3.1: Tri-carboxylic acid functional PDMS

3.3.2. Synthesis of PDMS-coated Magnetite Nanoparticles

The methods for synthesizing the nanoparticles complexed with carboxylate-functional polydimethylsiloxane (PDMS) oligomers (Figure 3.1) have been previously reported.[17, 18] The PDMS oligomer that was utilized for the ferrofluid in the present work was a 3242 g mol^{-1} PDMS dispersion stabilizer prepared by the following method:

D_3 (51.23 g, 0.23 mol) was sublimed into a flame-dried roundbottom flask. The flask was purged with nitrogen, and cyclohexane (50 mL) was added to the flask via a syringe. Once the D_3 monomer was dissolved at room temperature, 1.6 M *n*-butyllithium (10.86 mL, 0.0174 mol) was added to the reaction flask, and the solution was stirred for 0.5 h. THF (15 mL) was then charged to the solution as a reaction promoter. ^{1}H NMR was used to monitor the progress of the living anionic polymerization. At ~95% conversion of monomer, the polymer was terminated with an excess of trivinylchlorosilane (3.78 mL, 0.0261 mol) and stirred overnight. The PDMS oligomer was diluted with chloroform, and washed with deionized water (3X). The solution was concentrated under vacuum and poured into methanol to precipitate the liquid polymer. The polymer was dried under vacuum at 80 ^{0}C overnight to remove residual monomer.

The thiol-ene addition of mercaptoacetic acid to the trivinylsilane-functional PDMS oligomer was conducted as follows. A 2800 g mol^{-1} trivinylsiloxy terminated PDMS (15 g, 0.016 eq vinyl) was added into a flame-dried, roundbottom flask and dissolved in distilled toluene (25 mL). The reaction solution was deoxygenated by sparging with nitrogen for 2 h. AIBN (0.0037 g, 2.4 x 10^{-4} mol) and mercaptoacetic acid (1.67 mL, 0.024 mol) were added to the reaction vessel, and the flask was purged with nitrogen. The reaction was heated to 80 ^{0}C and stirred for 1 h. Reaction completion was confirmed by observing the disappearance of the vinyl proton peaks at ~6 ppm in the ^{1}H NMR spectra. The solvent was removed under vacuum,

and the polymer was stirred in methanol (30 mL) for 30 min. Deionized water was added to the solution until the polymer coagulated into a solid, and then it was collected via filtration. The methanol/deionized water coagulation process was repeated several times (5X), and the polymer was dried under vacuum at 80 ^{0}C. The M_n of the functionalized PDMS oligomer was determined to be 3242 g mol^{-1} by ^{1}H NMR.

The preparative method for a 50:50 wt:wt PDMS stabilizer:magnetite complex is provided. Magnetite was synthesized using a chemical precipitation of iron salts after reaction with base. Iron (III) chloride hexahydrate (2.01 g, 0.00744 mol) and iron (II) chloride tetrahydrate (0.736 g, 0.00370 mol) were weighed into separate roundbottom flasks and each was dissolved in 20 mL of deoxygenated water. The two iron salt solutions were added to a 500-mL, three-necked, roundbottom flask connected to an overhead mechanical stirring apparatus. Ammonium hydroxide (15 mL) was added via syringe until the rapidly stirring solution turned black and reached a pH of 9-10. The 3242 g mol^{-1} PDMS dispersion stabilizer (0.86 g) was dissolved in dichloromethane (20 mL) and was added to the basic magnetite dispersion. After stirring for approximately 30 min, 50 vol % aqueous hydrochloric acid (~6 mL) was added slowly until the solution became slightly acidic (pH 5-6). The acidic interfacial solution was stirred for ~1 h, then the dichloromethane was removed under vacuum. The magnetite complex was collected with a magnet and the water was decanted. The magnetite complex was washed several times with water (5X) and methanol (5X) before drying overnight at 40 ^{0}C under reduced pressure. This produced the material that was used as the feedstock for the magnetic separations.

3.3.3. Magnetic Separation of PDMS-coated Magnetite Nanoparticles

Magnetic separation columns were comprised of ~6 g of soft iron granules firmly packed into 3-mL plastic syringes. A magnetic field of 0.24 Tesla was generated by a NdFeB doughnut-shaped magnet placed around the exterior of the syringe. PDMS-coated magnetite nanoparticles were diluted in chloroform to a concentration of 0.002 mg mL^{-1}. The dispersion was sonicated with a Biologics ultrasonic homogenizer (model 150V/T) for 5 min using the 50% power setting with a micro-tip probe and a 50% pulse cycle. Following sonication, 150 mL of the chloroform dispersion (0.3 g of particles) was passed through the column at a flow rate of ~20 mL min^{-1} and collected. Alternatively, 150 mL of the chloroform dispersion was passed through 5 freshly prepared separation columns in series with a donut magnet around each syringe. The positions

of the separation columns were adjusted such that the donut-shaped magnets were approximately 10 cm apart to prevent strong magnetic interaction. The collected dispersions were dried under vacuum and weighed to determine the amount of material that had been retained in the separation columns.

3.3.4. Characterization

3.3.4.1. Thermogravimetric Analysis

Thermogravimetric analysis was carried out on the PDMS-coated magnetite nanoparticles using a TA Instruments TGA Q500. After first equilibrating the samples at 30 ºC, the temperature was ramped at 10 ^{o}C min^{-1} to a maximum of 700 ºC under a nitrogen purge. Char yields (the mass remaining at the end of the experiments) were recorded at the maximum temperature.

3.3.4.2. Transmission Electron Microscopy (TEM)

TEM was conducted with a JEOL 3000F field-emission-gun transmission electron microscope (operated at 300 kV) equipped with a 1024x1024 pixel digital imaging system. Dry samples of the magnetite complexes were dispersed in chloroform and cast onto amorphous carbon-coated copper grids for analysis. Great care was taken to ensure that both eucentric height and focus were set consistently from one sample to another in order to reduce uncertainty in the digital image analyses. Images were acquired at a magnification of 300 kx, corresponding to 1.65 pixels nm^{-1}. This magnification gave both sufficient resolution and contrast for digital image analysis, and provided a large enough field of view to obtain adequate numbers of particles. Particle size analysis was performed using Reindeer Graphics' Fovea Pro 4 plug-in for Adobe Photoshop CS2. Mean and standard deviations of the particle size diameters were calculated based upon 3500-5000 particles per sample, and particle size distributions were fitted with a Weibull distribution.

3.3.4.3. Superconducting Quantum Interference Device (SQuID)

Magnetic properties were measured using a 7-Tesla Quantum Design MPMS SQuID magnetometer. Hysteresis loops on dried samples of the magnetite-polymer complexes were performed in fields of up to 7 T at 300K and 5K. The 5K hysteresis loop was obtained to

determine values of coercivity, and saturation magnetization, and to observe the presence or absence of any exchange bias. Samples of the PDMS-coated magnetite particles were mobile at temperatures as low as 170K (the glass transition temperature, T_g of the PDMS is approximately 150K)[130, 131]. To avoid Brownian reorientation of the particles, the samples were mixed with molten wax and then allowed to cool, creating a solid sample at 300K. Zero-field-cooled/field-cooled measurements were performed on these samples in a field of 0.01 T.

3.3.4.4. Dynamic Light Scattering (DLS)

DLS measurements were conducted with a Malvern Zetasizer ZS compact scattering spectrometer (Malvern Instruments Ltd, Malvern, UK) at a wavelength of 633 nm from a 4.0 mW, solid-state He-Ne laser at a scattering angle of 170°. Volume and number average diameters were calculated using Malvern's Zetasizer Nano 4.2 software utilizing an algorithm, based upon Mie theory, that transforms time-varying intensities to particle size calculations.[132]

3.4. Results and Discussion

3.4.1. Synthesis and Separation of Magnetic Nanoparticles

PDMS-coated magnetite nanoparticles have been prepared with different sizes to compare techniques for size analysis and test theoretical calculations of size distributions. The magnetite was synthesized by reacting a stoichiometric ratio of iron chloride salts with hydroxide. The surfaces of the magnetite nanoparticles were coated by adsorbing a PDMS oligomer that had three carboxylates on one end and a non-functional trimethylsilyl group at the other (Figure 1). The isoelectric point of magnetite in water is pH ~6.8, so at pH 6, there is a net positive charge on the metal oxide surface. The isoelectric point of magnetite has been confirmed by measurements of the zeta potentials by a number of authors using a variety of electrolytes including $NaClO_4$,[133] $NaNO_3$,[134] and H_2SO_4.[135] It is reasoned that the PDMS adsorbs through electrostatic binding of the negatively-charged carboxylate end group onto the cationic magnetite surface, and that the non-functional end of the PDMS oligomer provides a brush layer that extends outward from the nanoparticle to prevent aggregation. Following adsorption, the particles were extracted with methanol (a solvent for the carboxylate-functional PDMS) to remove any unbound polymer.

To remove aggregates and large particles, dispersions of the PDMS-coated magnetite particles in chloroform were passed through magnetic separation columns. Size distributions were compared among complexes that had not been magnetically separated, those passed through a single separation column (with ~60 wt % yield), and those passed through a series of five separation columns (with ~40 wt % yield). All of the complexes were extracted with methanol to remove any residual unbound polymer that might have passed through the separation column, and then the magnetic complexes were collected with a magnet.

The sizes of these polymer-magnetite complexes in dispersions reflect the densities of oligomeric chains on their surfaces, the molecular weights of the chains, and their propensity to interact with the solvent. The particle-polymer compositional ratios were determined by weight loss measurements (TGA). The materials were heated under nitrogen in a TGA furnace past the point of thermal degradation of the PDMS brushes, and this left only the magnetite mass as residual char. As previously reported, PDMS leaves no detectable char above 650 ºC when heated under these conditions.[136] It has also been shown previously that the magnetite does not lose weight under the conditions utilized in these measurements.[137] The materials that had been magnetically separated had lower concentrations of magnetite compared to the original material (Table 3.1). Because of their larger magnetic moments, larger particles and aggregates are more likely to be entrapped by the separation column. Since the separations preferentially removed aggregates and larger particles, complexes that passed through the columns should have higher magnetite specific surface areas, leading to higher mass fractions of polymer in the eluted materials.

3.4.2. Analysis of the Sizes of the Magnetite Cores by TEM

Dispersions of PDMS-coated magnetite particles were cast onto carbon grids and analyzed via TEM. The samples that had been magnetically separated had lower fractions of aggregates (Figure 3.2), but further interpretation with only a visual inspection of the micrographs was inconclusive.

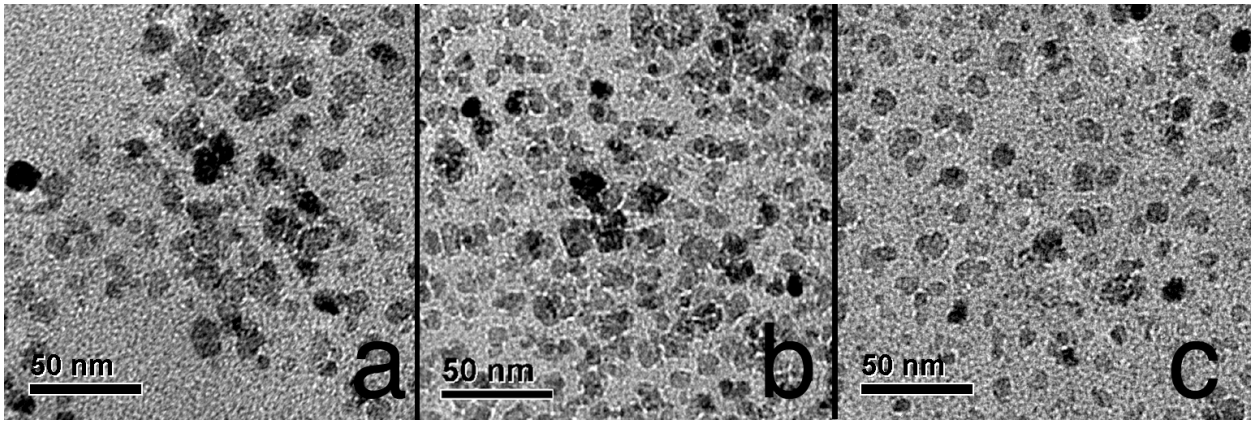

Figure 3.2. TEM images of PDMS-magnetite particles that (a) were not magnetically separated, (b) particles that were passed through a single separation column, and (c) five separation columns.

Size analyses were performed to determine the distributions of the diameters of the magnetite cores of the particles. Typically 4-6 TEM images were analyzed for each sample, resulting in about 4000 particles being measured. Images were blurred slightly (typically 1-2 pixels) to flatten noise that was present in the background, and then an intensity threshold was applied to distinguish the particles from the background. Fovea Pro's watershed tool was then used to distinguish particles that were close together but not connected. Before measuring the sizes of the particles, the original image was manually compared to the threshold image (what the software interpreted to be particles) to check for any discrepancies, and all of the detected errors were manually corrected on the threshold image. This ensured that only true particles were identified in the images and any potential artifacts were removed prior to analysis. The arithmetic means and standard deviations of the distributions were calculated from the data (Table 3.1). It was found that the particle size distributions of all three samples could be accurately represented by a two-parameter Weibull distribution (Figure 3.3). The expression for the Weibull distribution is

$$P(r) = \frac{\gamma}{\alpha}\left(\frac{r}{\alpha}\right)^{\gamma-1} \exp\left(\frac{-r}{\alpha}\right)^{\gamma}$$

Eq. 3.1

where $P(r)$ is the probability of a particle with radius r, α is a scale parameter, and γ is a shape parameter.[138]

Table 3.1: Composition from TGA, magnetite size and standard deviation from TEM, saturation magnetization (M_s) at 5K of PDMS-magnetite complexes

Sample Name	PDMS-Magnetite Complex	**Wt % Magnetite**	**Mean Magnetite Diameter (nm)**	**Standard Deviation (nm)**	**M_s @ 5K (Am^2/kg)**
0-pass	Original Sample – Not Magnetically Separated	58	10.4	5.6	78.6
1-pass	Passed through a single separation column	43	7.7	4.2	57.4
5-pass	Passed through 5 magnetic separation columns	20	4.5	2.3	39.1

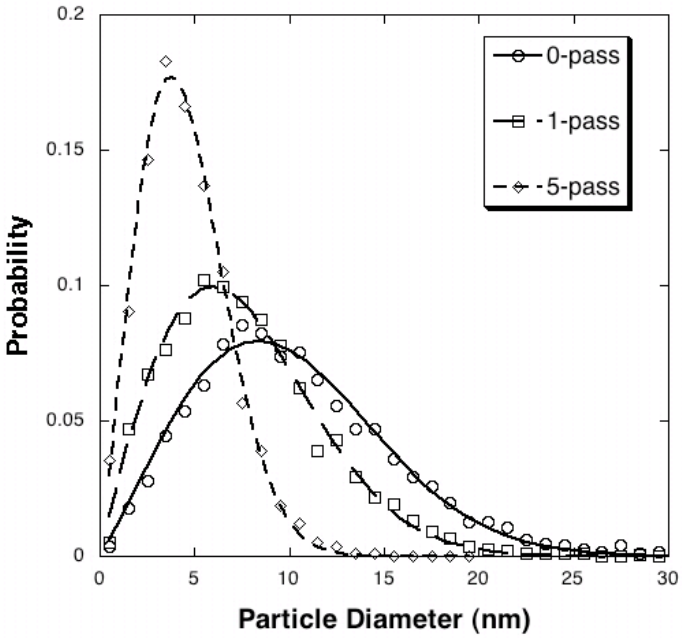

Figure 3.3. Weibull (number based) probability distribution functions of the magnetite core sizes fitted to particle diameters obtained from TEM.

Magnetic separations resulted in particles that were smaller and had narrower distributions (Figure 3.3). Moreover, multiple passes through the separation columns produced smaller average sizes and narrower distributions.

3.4.3. Magnetic Properties of the PDMS-magnetite Nanoparticle Complexes

Zero field cooled-field cooled (ZFC-FC) curves on the dried complexes[†] showed sudden changes in magnetization at 170K and 230K. These changes were thought to be associated with changes in the rheological properties of the PDMS surfactant, where the particles undergo Brownian rotation as the sample heats through transition temperatures corresponding to the PDMS in the complexes. In order to avoid/reduce these effects the samples were dissolved in a wax in order to fix the orientation of the PDMS-coated magnetite. The ZFC-FC curves for the fixed samples are shown in Figure 3.4. Although the artifacts associated with the Brownian rotation have been reduced they have not been eliminated, particularly in the case of the 5-pass sample. This may be due to a partial segregation of the complex and wax during the freezing of the wax, resulting in microdroplets of relatively pure complex. The ZFC-FC curves of both the 0-pass and 1-pass samples do not close, and this suggests the presence of some ferromagnetic particles, possibly in the form of aggregates. The curves for the 5-pass sample close at a temperature of 210K, but this corresponds to a rotational artifact in both the zero field cooled and field cooled curves, and may not be a true representation of the maximum blocking temperature. There was not, however, any evidence for a significant ferromagnetic contribution in this sample at higher temperature as can be seen in the ZFC-FC curves for the 0-pass and 1-pass samples. This demonstrates that the magnetic separation technique is an efficient method of removing larger particles and aggregates.

[†] When all of the solvent is removed the complex with the ~3242 g mol^{-1} PDMS is a viscous liquid with the consistency of thick honey at room temperature.

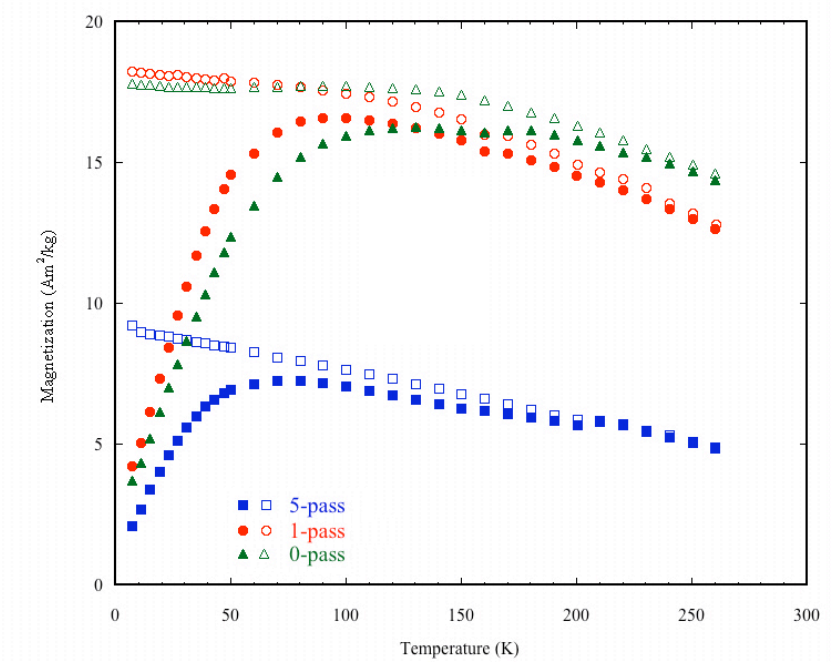

Figure 3.4. Zero-Field-Cooled (closed symbols)/Field-Cooled (open symbols) Curves

Hysteresis loops measured at 5K and 300K are shown in figures 3.5 and 3.6 respectively. The values of specific magnetization given in the figures have been corrected to reflect the magnetization of the magnetite particles (i.e. Am^2 per kg of Fe_3O_4). Analysis of the 5K hysteresis loops shows that all three materials have coercivities of ~250 Oe (as expected for magnetite particles) and no sign of any enhanced coercivity or exchange bias which might indicate the presence of coupled magnetic phases or significant disorder within the particles. Saturation magnetization was calculated by subtracting the diamagnetic contribution as inferred from the slope of the hysteresis curve at high fields. The saturation magnetization of the magnetite declines with increasing number of magnetic separation passes which correlates to a decrease in average particle size, as shown in Table 3.1. This decrease in magnetization with average particle size in this small size range is well documented in the literature.[139, 140]

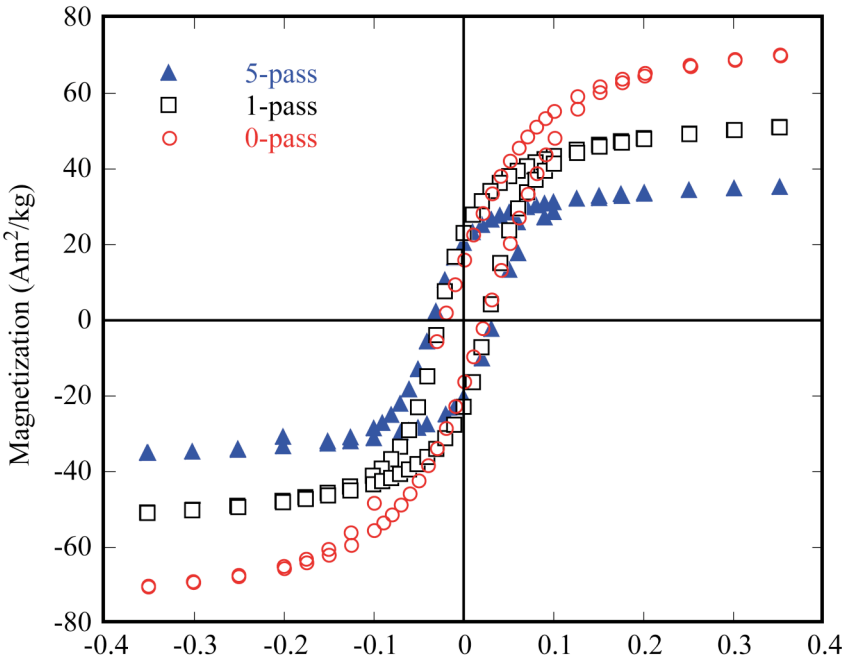

Figure 3.5. The 5K hysteresis loops show minimal coercivity, zero exchange bias and a decreasing saturation magnetization with increasing number of magnetic separations

The magnetization curves for the samples at 300K show no sign of hysteresis. This is as expected, since at 300K the samples are a viscous liquid in which any ferromagnetic particles will undergo Brownian rotation and will rapidly align with the applied field.

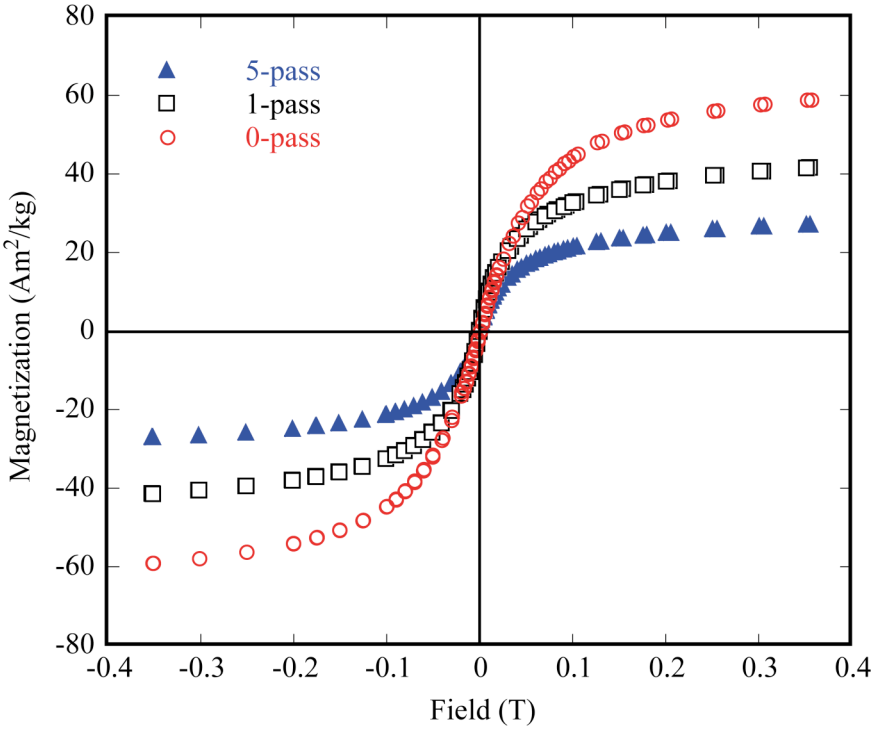

Figure 3.6. The 300K hysteresis loops show no presence of hysteresis and a decrease in the saturation magnetization with increasing magnetic separation.

3.4.4. Calculation of Chain Density and Particle Functionality

Chain densities (the number of chains per nm^2 of magnetite surface) were calculated using the Weibull probability functions of the magnetite core sizes from TEM image analysis, and compositions of the complexes from TGA. This was accomplished by first calculating the average surface area, $\overline{A}$, and the average volume of the magnetite cores, $\overline{V}$.

$$\overline{A} = 4\pi\overline{r^2} = 4\pi\int_0^\infty r^2 * P(r)dr$$

Eq. 3.2

$$\overline{V} = \frac{4}{3}\pi\overline{r^3} = \frac{4}{3}\pi\int_0^\infty r^3 * P(r)dr$$

Eq. 3.3

P(r) is a Weibull probability function of the magnetite with radius, r. By taking the ratio of average surface area to average volume and multiplying by the reciprocal of density of magnetite (density = 5.17 g mL^{-1}),[141] the surface area of the cores per mass of the magnetite was calculated.

$$\frac{\bar{A}}{\bar{V}} * \frac{1}{Density} = \frac{Area}{Mass}$$

Eq. 3.4

Taking into account the compositions of magnetite and PDMS in the complexes, the magnetite surface area was calculated as

$$\frac{Area}{Mass} * Mass\ Fraction\ Magnetite = Surface\ area\ of\ particles$$

Eq. 3.5

In a similar manner, by considering the mass fraction of the polymer and dividing by the number average molecular weight, M_n, and multiplying by Avogadro's number, N_a, the numbers of chains in the complexes were calculated.

$$Mass\ Fraction\ PDMS * \frac{1}{M_n} * N_a = Number\ of\ chains$$

Eq. 3.6

Using the values from Eq. 3.5 and Eq. 3.6, the average number of chains per unit of surface area was calculated.

$$\frac{Number\ of\ chains}{Surface\ area\ of\ particles} = Chains / Area$$

Eq. 3.7

Finally the functionality (number of chains per particle), f(r), of a particle of given radius is

$$f(r) = 4\pi r^2 * \frac{Chains}{Area}$$

Eq. 3.8

The calculated values for the PDMS-coated magnetite complexes (Table 3.2) indicate that the particles that were magnetically separated have more chains per area than the complex that was not magnetically separated. Thus, it is likely that by removing the clustered particles

from the ensemble, a more discrete distribution that can be more efficiently coated with a higher chain density is produced. In addition, the increased curvature of a smaller particle may also allow for a higher chain density.

3.4.5. Analysis of the Sizes of the PDMS-Magnetite Nanoparticles by DLS

The hydrodynamic diameters of the PDMS-magnetite nanoparticles were measured by DLS. The nanoparticle complexes were diluted with chloroform, which is a good solvent for PDMS.[142] Consistent with the core sizes derived from TEM, materials that had been magnetically separated had smaller diameters and narrower distributions in solution (Table 3.2). The probability size distribution curves constructed from the TEM and DLS data (Figure 3.3 and Figure 3.7 respectively) have similar shapes, and the material that had been rigorously separated through five magnetic separation columns had a narrower size distribution when analyzed by either method relative to the other two samples. It was expected that the DLS based sizes would be larger then the TEM values, since DLS measures the size of both the magnetite cores and the PDMS corona, while the TEM images only the magnetite cores. Moreover, since the chloroform dispersing medium is a good solvent for PDMS, the positive interaction between the PDMS chains and the medium would also be expected to increase the sizes as measured by DLS.

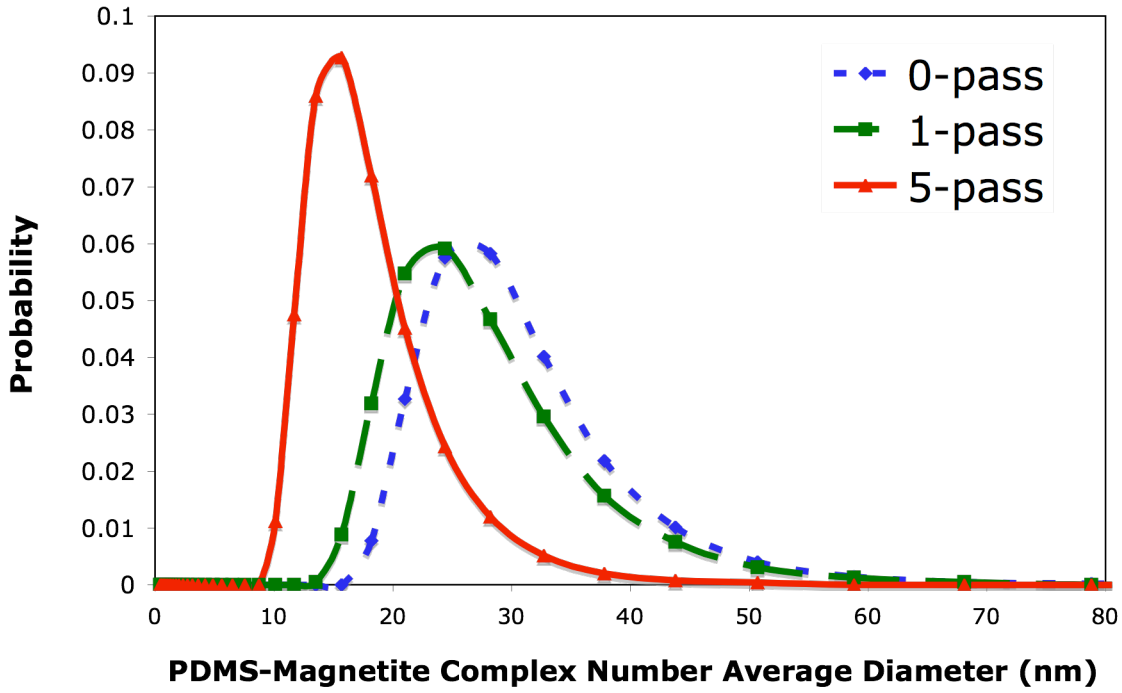

Figure 3.7: Number average hydrodynamic diameters from DLS indicate that particles that had been magnetically separated were smaller than those that were not separated.

3.4.6. Predicted Sizes of the Nanoparticle Complexes in Dispersions

We have developed a method for applying chain extension theory to predict corona sizes around the magnetite cores.[137] This was utilized in combination with TEM size distributions of the magnetite cores to arrive at predicted sizes for these complexes in dispersion. The predicted solution sizes derived from combined experimental and theoretical values were then compared to experimental DLS data (Table 3.2). The sizes of the polymer-magnetite complexes were calculated with a density distribution (DD) model developed by Vagberg et al. (Figure 3.8).[68] This model, based on a model for star polymers by Daoud and Cotton,[71] assumes concentric shells with a constant number of blobs in each shell. The blob diameter $\xi(r)$ is a continuous function of distance from the surface. The segment density in the shell varies with distance from the core that, in the present case, is the surface of the magnetite particle.

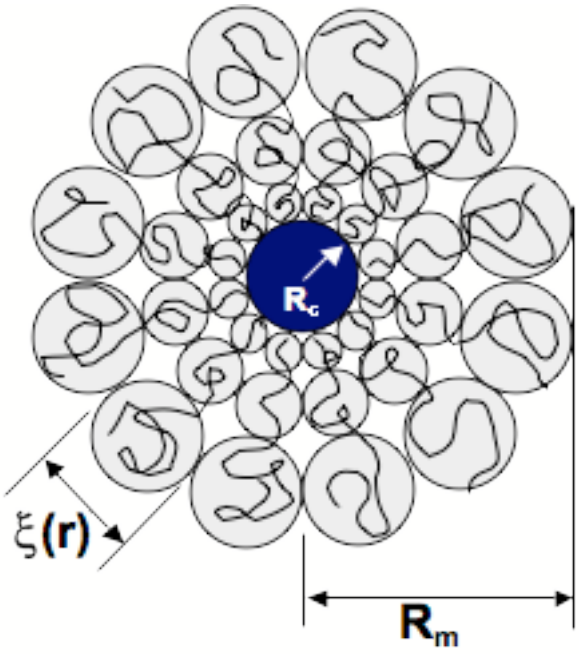

Figure 3.8. Representation of the PDMS-magnetite nanoparticle complex showing the Vagberg model parameters. Adapted from Daoud and Cotton.[71]

The DD model predicts the radius R_m of the PDMS-magnetite complex as a function of the core magnetite radius.

$$R_m(r) = \left(\frac{8 N_k f(r)^{\frac{1-\nu}{2\nu}}}{3 * 4^{1/\nu} \nu} L_k^{1/\nu} + r^{1/\nu} \right)^{\nu}$$

Eq. 3.9

where N_k is the number of Kuhn segments in one of the corona chains (a PDMS chain in the present case), ν is the Flory exponent, r is the radius of the magnetite particle, and $f(r)$ is the number of corona chains per particle which was calculated using Eq. 3.8. The Flory exponent, ν, varies between 0.5 at a theta condition and 0.6 for a good solvent (chloroform in this case). The statistical segment or Kuhn length L_k is defined as

$$L_k = c_\infty l_0$$

Eq. 3.10

and the number of statistical segments in a chain, N_k, is defined as

$$N_k = n / c_\infty$$

Eq. 3.11

where c_∞ is the characteristic ratio (5.2 for PDMS[68]), l_0 is the average length of a backbone bond (0.155 nm for PDMS), and n is the number of backbone bonds in a chain (2*degree of polymerization for PDMS).

The number average diameter, $\overline{D_n}$, of the nanoparticle complex can be calculated as

$$\overline{D_n} = 2\int_0^\infty P(r)R_m(r)dr$$

Eq. 3.12

The volume average diameter, $\overline{D_v}$, can be calculated as

$$\bar{D}_v = 2\left(\frac{3}{4\pi}\bar{V}_m\right)^{1/3}$$

Eq. 3.13

where the average volume of the PDMS-magnetite nanoparticle complex, $\bar{V}_m$, is found by

$$\bar{V}_m = \frac{4}{3}\pi\int_0^\infty P(r)R_m^3(r)dr\,.$$

Eq. 3.14

The intensity average diameter was determined using a method developed by Prudhomme et al.[143] In dynamic light scattering, the particle sizes can be determined by first describing the relationship between the first cumulant, $\Gamma(q)$, and the scattering from a distribution of particles.

$$\frac{\Gamma(q)}{q^2} = \frac{\sum_{j=1}^{\infty} n_j I_j D_j}{\sum_{j=1}^{\infty} n_j I_j}$$

Eq. 3.15

where q is the wave vector, n_j is the number of particles at a particular radius r_j, I_j is the scattering intensity from these particles, and D_j is the diffusion coefficient.[65] The diffusion

coefficient, D_0, for the particles can be described in terms of the first cumulant and the Stokes-Einstein relation

$$D_0 = \frac{\Gamma(q)}{q^2} = \frac{k_B T}{6\pi\mu r}$$

Eq. 3.16

where k_B is Boltzmann's constant, T is temperature in Kelvin, and μ is the viscosity of the solvent. Combining equations 3.15 and 3.16, the intensity average radius, $\overline{R_I}$, can be described in terms of

$$\frac{6\pi\mu\overline{R_I}}{k_B T} = \frac{\sum_{j=1}^{\infty} n_j I_j}{\sum_{j=1}^{\infty} n_j I_j \frac{k_B T}{6\pi\mu R_j}}.$$

Eq. 3.17

The hydrodynamic radius of the particles was shown by DLS to be on the order of 30 nm. Therefore these particles should be in the Rayleigh scattering range in which the scattering intensity, I_j, can be described as

$$I_j = I_0 q^4 \cos^2\theta \left[\left(\frac{n_p}{n_s}\right)^2 - 1\right]^2 \frac{R_j^{\,6}}{9\beta^2} F_f(\theta)$$

Eq. 3.18

where I_0 is the incident light intensity, θ is the scattering angle, n_p and n_s are the refractive indices of the particle and the solvent respectively, β is the distance from the particle to the light detector, and $F_f(\theta)$ is the Rayleigh form factor .[144] The scattering intensity is directly related to the radius of the particles to the sixth power, and thus equation 3.17 reduces to

$$\overline{R_I} = \frac{\sum_{k=1}^{\infty} n_k R_k^{\,6}}{\sum_{k=1}^{\infty} n_k R_k^{\,5}}.$$

Eq. 3.19

For a particle size distribution described by the Weibull probability function, the discrete summations in eq 3.19 can be replaced by integrals to calculate the intensity average diameter, $\overline{D_I}$ as

$$\overline{D_I} = 2\overline{R_I} = 2\frac{\int_0^\infty P(r)R_m(r)^6 dr}{\int_0^\infty P(r)R_m(r)^5 dr}$$

Eq. 3.20

Table 3.2: Comparison of solution sizes of the complexes derived from chain extension theory in combination with TEM (for the core sizes) and experimental values from DLS of the volume average diameter of the PDMS-magnetite complexes.

Sample	Average # chains/nm^2	Intensity Average Diameter Measured (DLS)	Intensity Average Diameter Calculated	Volume Average Diameter Measured (DLS)	Volume Average Diameter Calculated	Number Average Diameter Measured (DLS)	Number Average Diameter Calculated
0 - pass	1.68	53.3 ±1.5	29.8	36.4 ±2.1	23.8	29.0 ±2.1	22.1
1 - pass	1.85	49.9 ±5.3	26.2	33.8 ±1.0	20.8	26.2 ±2.1	19.3
5 - pass	4.23	35.8 ±1.8	21.4	22.5 ±0.4	18.1	17.0 ±0.7	17.1

Calculations were made for the intensity, volume, and number average sizes for the three samples and compared to the DLS values (Table 3.2). In all cases, the predicted values of the nanoparticle complex diameters vary in the expected order: intensity average > volume average > number average. Overall, the sizes measured by DLS, while larger, followed a similar trend to the values calculated from the TEM and compositional results in combination with the chain extension predictions. It should be noted that several classical problems arise in analyzing particle size distributions by DLS. First, transformation of the autocorrelation function to a size distribution is mathematically non-unique. While there is always a question of non-uniqueness in DLS size calculations, a comparison of the three averages derived from the TEM core-brush model with the corresponding averages from DLS suggests that the DLS data are sound. Secondly, in the Rayleigh regime, the intensity of the scattered light is proportional to particle

radius to the 6^{th} power. Thus, the scattering for particles in the large part of the distribution can complicate detection of scattering from smaller particles. This problem is less severe as the particle size distribution narrows. Our proposed method for predicting polymer-nanoparticle size distributions couples a proven polymer brush model with TEM-based sizes of the magnetite cores, allowing one to calculate any moment of the size distribution. For example, we calculated the intensity average radius in a dispersion in which the scattering intensity varies as r^6 (see equations 3.18-3.20).

The closest agreement was for the most narrow particle size distribution (five times magnetically separated) involving the volume and the number averages, the averages that give the least weight to aggregates in the distributions. Thus, the effects of any errors in calculating or estimating the size distribution are smallest with the calculated number average, larger with the volume average and largest with the intensity average. It is likely that samples with narrower size distributions would fit this model better than those with larger polydispersity. It is also likely that some larger particles and aggregates were not fully included in the TEM image analysis as they are difficult to image. This would result in lower calculated values.

3.5. Conclusions

PDMS-magnetite nanoparticle complexes were synthesized and magnetically separated, and this produced different size distributions. The complexes that were magnetically separated were smaller and had narrower size distributions than those that were not magnetically separated. TEM and DLS showed similar trends in distributions of the magnetite cores and complex sizes as a function of the degree of magnetic separation, and this permitted us to utilize measurements of core size distributions to predict sizes of the complexes in dispersions. A careful experimental analysis by TEM of the size distributions of the magnetite cores was combined with the assumption that the surface chain density was constant. This was then utilized with a polymer brush model based on star polymers to predict the distributions of particle sizes in dispersions. This approach provides a tool for a more precise characterization of the size distributions of polymer-nanoparticle complexes, relative to previous methods utilized only a mean (single) core particle size.

It is critical that one be able to characterize the distributions of particle sizes in order to predict the stability of the polymer-nanoparticle complexes in dispersions, because the

interparticle potentials depend on the size distributions. While it is not yet clear how to fully account for the effect of size distribution on the separate van der Waals, steric electrostatic and magnetic potentials, the ability to predict the size distributions is a necessary first step toward developing an understanding of these dependencies. Moreover, the rheological properties of neat fluids comprised of polymer-nanoparticle complexes, such as those investigated in this work, depend strongly on the larger particles in the distributions. In terms of applications for nanoparticles as drug delivery vehicles, pharmaceutical scientists will likely need to quantify the fractions of particles that are below or above a critical size to avoid clearance via the kidneys or clogging of capillary blood vessels.

With some modifications this model could be applied to other nanoparticles that are coated with polymers and surfactants, allowing scientists and engineers to approximate the sizes and distributions of newly developed nanoparticles. In addition, these calculations could be extended to calculating the steric interaction forces between particles to aid in predicting the stability of nanoparticle suspensions.

3.6. Acknowledgements

The authors are grateful for the financial support of the NSF/ARC Materials World Network for the Study of Macromolecular Ferrofluids (DMR-0602932 and LX0668968), the National Eye Institute of the NIH under SBIR contract B6867G1, and the ARC Discovery Grant - DP0559333. Transmission electron microscopy was carried out using the facilities at the Centre for Microscopy, Characterisation and Analysis, The University of Western Australia, which is supported by University, State and Federal Government funding.

4. Stability of Polydimethylsiloxane-Magnetite Nanoparticles against Flocculation: Interparticle Interactions of Polydisperse Materials

O.Thompson Mefford,[a] M. L. Vadala,[b] M. R. J. Carroll,[c] R. Mejia-Ariza,[a] B. L. Caba,[a] T. G. St. Pierre,[c] R. C. Woodward,[c] R. M. Davis,[a] and J. S. Riffle[a*]

[a]Macromolecules and Interfaces Institute, Virginia Tech, Blacksburg, Virginia 24061

[b]NanoMedics, LLC, Erie, PA, 16509

[c]School of Physics, University of Western Australia, Crawley, Western Australia 6009, Australia

4.1. Abstract

The stability against flocculation of fluid complexes comprised of magnetite nanoparticles coated with polydimethylsiloxane (PDMS) oligomers was investigated theoretically and experimentally. Particle-particle interaction potentials in a theta solvent and in a good solvent for the PDMS were predicted by calculating van der Waals, electrostatic, steric, and magnetic forces as functions of interparticle separation distances. A variety of nanoparticle sizes and size distributions were considered. Calculations of the interparticle potential in dilute suspensions indicated that flocculation was likely for the largest 1% of the population of particles. Finally, the rheology of these complexes over time in the absence of a solvent was measured to probe their stabilities against flocculation as neat fluids. An increase in viscosity was observed upon aging, suggesting that some agglomeration occurs with time. However, the effects of aging could be removed by exposing the sample to high shear, indicating that the magnetic fluids were not irreversibly flocculated.

Keywords: Magnetite, nanoparticle, dispersion, polydimethylsiloxane, DLVO, ferrofluid, rheology

4.2. Introduction

In recent years, the use of magnetic nanoparticles in medical applications has grown significantly. Currently, magnetic nanoparticles are utilized as contrast agents for MRI to diagnose tumors and cardiovascular disease, as hyperthermia agents for brain cancer therapy, and for magnetic separations of cells and bioagents.[2, 12, 13, 145, 146] In addition, researchers in our

laboratories have synthesized hydrophobic ferrofluids comprised of polymer-coated magnetite nanoparticles for treating retinal detachments. [14-16, 18, 93, 94] These latter materials are the focus of this paper.

Tailoring the surfaces of these materials is critical for the success of these applications. Polymers that form sheaths around the magnetic nanoparticles can function to (i) suspend the nanoparticles in the intended medium, (ii) provide a stabilizing layer that prevents agglomeration, and (iii) reduce immune response. This has been accomplished with a variety of polymers.[147] Magnetic iron oxide nanoparticles have been coated with water soluble polymers such as dextran[113] and poly(ethylene oxide),[28, 114, 146] and with nonpolar materials such as polystyrene and poly(methyl methacrylate).[115]

The stabilities of polymer-magnetite complexes in dilute suspensions are related to the net particle-particle interaction potentials. Particles are attracted by van der Waals and magnetic interactions and repelled by steric and electrostatic forces. To maintain stability of a dispersion, the repulsive forces must be substantial enough to prevent agglomeration driven by the attractive forces. This balance has been extensively studied in the realm of colloidal suspensions. The classical approach utilizes Derjaguin-Landau-Verwey-Overbeek (DLVO) theory[148-151] as a means for predicting the net interaction energy including van der Waals, electrostatic, and steric forces in dilute dispersions. By varying the factors that contribute to each of the forces, the net interactions of particles can be controlled, leading to control over colloid stability and flocculation rates. For instance, the rate at which gold nanoparticles agglomerate has been altered by changing the electrostatic charge on the surface of the particles,[20] or alternatively by changing the ionic properties of the medium.[152, 153] The stabilities of magnetic nanoparticle dispersions have also been investigated by altering the pH in the presence of applied external magnetic fields. This altered the electrostatic repulsions, and resulted in flocculation of maghemite particles in strong magnetic fields.[154] It has also been observed that magnetic nanoparticles can form chain-like structures in dilute dispersions with application of an applied field.[155]

This paper will describe the size distribution of PDMS-magnetite nanoparticle complexes where the PDMS forms a stabilizing brush layer that contributes significantly to the overall size of the complexes. For a given slice in the size distribution, DLVO theory can provide qualitative insight into the stability against flocculation, an important issue for applications of these

complexes. In this work, dilute suspensions of the polymer-nanoparticle complexes are considered in both a good solvent for the PDMS and a theta solvent, and the viscosities of an undiluted fluid will be presented.

4.3. Experimental

4.3.1. Materials

Hexamethylcyclotrisiloxane (D_3, Gelest, Inc., 98 %) was dried over calcium hydride and sublimed under vacuum into pre-weighed, flame-dried, roundbottom flasks, each containing a magnetic stir bar. The flasks were purged with nitrogen and re-weighed to determine the amount of D_3 in each flask. Cyclohexane (EM Science, 99%) was stirred with concentrated sulfuric acid for 48 h, washed with deionized water until neutral, stirred over magnesium sulfate, then over calcium hydride, distilled, stored over sodium under a nitrogen atmosphere, and distilled prior to use. Tetrahydrofuran (THF, EM Science, 99.5%) was dried over calcium hydride, distilled, and stored over sodium in the presence of benzophenone under a nitrogen atmosphere until the solution was a deep purple. The THF was distilled just prior to use. Toluene (Burdick and Jackson, 99.9%) was washed twice with concentrated sulfuric acid and neutralized with water. It was dried over magnesium sulfate for 1 h, then over calcium hydride overnight and distilled just before use. Aqueous hydrochloric acid (50% by volume) was prepared by adding 5 mL of concentrated hydrochloric acid (EM Science) to 5 mL of deionized water in a graduated cylinder. Ferric chloride hexahydrate ($FeCl_3 \cdot 6H_2O$) and ferrous chloride tetrahydrate ($FeCl_2 \cdot 4H_2O$) (both from Aldrich) were stored under nitrogen in a desiccator and used as received. Iron granules (Alfa Aesar, 1-2 mm, 99.98%) were washed repeatedly with a variety of solvents to remove any coating on the surface. The granules were subsequently dried overnight in a vacuum oven at 40 ºC. Ammonium hydroxide (Alfa Aesar, 50% v/v aqueous), mercaptoacetic acid (Aldrich, 97%), 2,2'-azobisisobutyronitrile (AIBN, 98%, Aldrich), n-butyllithium (1.6 M, Aldrich), trivinylchlorosilane (Gelest, Inc., 95%), octamethylcyclotetrasiloxane (D_4, 99% Gelest) and trimethylchlorosilane (Gelest, Inc., 99%) were used as received. NdFeB doughnut-shaped magnets that were magnetized through the thickness were purchased from Engineered Concepts. The field generated by the doughnut magnets was 0.24 T, and the magnets had dimensions of 1.0 in (2.54 cm) I.D., 0.5 in (1.27 cm) O.D, and 0.25 in (0.635 cm) thick.

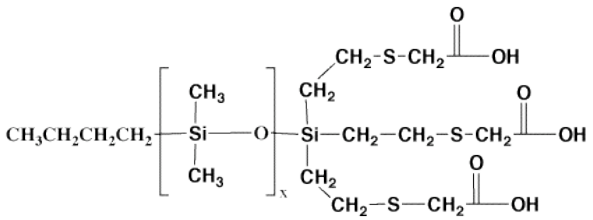

Figure 4.1: Tri-carboxylic acid functional PDMS

4.3.2. Synthesis of PDMS-coated Magnetite Nanoparticles

The method for synthesizing the nanoparticles complexed with a carboxylate-functional PDMS (Figure 4.1) have been previously reported.[17, 18] The PDMS oligomer that was utilized for the ferrofluid in the present work was a 3242 g mol^{-1} PDMS dispersion stabilizer prepared by the following method.

D_3 (51.23 g, 0.23 mol) was sublimed into a flame-dried, roundbottom flask. The flask was purged with nitrogen, and cyclohexane (50 mL) was added to the flask via a syringe. Once the D_3 monomer dissolved at room temperature, 1.6 M *n*-butyllithium (10.86 mL, 0.0174 mol) was added to the reaction flask, and the solution was stirred for 0.5 h. THF (15 mL) was then charged to the solution as a reaction promoter. ^{1}H NMR was used to monitor the progress of the living anionic polymerization. At ~95% conversion of monomer, the polymer was terminated with an excess of trivinylchlorosilane (3.78 mL, 0.0261 mol), and the mixture was stirred overnight. The PDMS oligomer was diluted with chloroform, and washed with deionized water (3X). The solution was concentrated under vacuum and poured into methanol to precipitate the liquid polymer. The polymer was dried under vacuum at 80 ^{0}C overnight.

A thiol-ene addition of mercaptoacetic acid to the trivinylsilane-functional PDMS oligomer was conducted as follows. A 2800 g mol^{-1} trivinylsiloxy terminated PDMS (15 g, 0.016 eq vinyl) was added into a flame-dried, roundbottom flask and dissolved in distilled toluene (25 mL). The reaction solution was deoxygenated by sparging with nitrogen through the solution for 2 h. AIBN (0.0037 g, 2.4 x 10^{-4} mol) and mercaptoacetic acid (1.67 mL, 0.024 mol) were added to the reaction vessel, and the flask was purged with nitrogen. The reaction was heated to 80 ^{0}C and stirred for 1 h. Reaction completion was confirmed by observing the disappearance of the vinyl proton peaks at ~6 ppm in the ^{1}H NMR spectra. The solvent was removed under vacuum, and the polymer was dissolved in methanol (30 mL) by stirring for 30 min. Deionized water was added to the solution until the polymer coagulated as a solid, and then

it was collected via filtration. The methanol/deionized water coagulation process was repeated 5 times, then the polymer was dried under vacuum at 80 ^{0}C. The M_n of the functionalized PDMS oligomer was determined to be 3242 g mol^{-1} by ^{1}H NMR.

The preparative method for a 70:30 wt:wt PDMS stabilizer:magnetite complex is provided. Magnetite was synthesized using a chemical precipitation of iron salts. Iron (III) chloride hexahydrate (2.01 g, 0.00744 mol) and iron (II) chloride tetrahydrate (0.736 g, 0.00370 mol) were weighed into separate roundbottom flasks, and each was dissolved in 20 mL of deoxygenated water. The two iron salt solutions were charged to a 500-mL, three-necked roundbottom flask equipped with an UltraTurrax T25 homogenizer. Careful attention was paid to maintaining an oxygen-free environment by purging the reaction vessel with a heavy nitrogen flow. The homogenizer speed was set to 13,000 rpm, and ammonium hydroxide (15 mL) was added via syringe until the homogenizing solution turned black and reached a pH of 9-10. The 3242 g mol^{-1} PDMS dispersion stabilizer (2.0 g) was dissolved in dichloromethane (60 mL) and was added to the basic magnetite dispersion. After stirring for approximately 30 min, 50 vol % aqueous hydrochloric acid (~6 mL) was added slowly until the solution became slightly acidic (pH 5-6). The acidic interfacial solution was stirred for ~1 h, then the dichloromethane was removed under vacuum. The magnetite complex was collected with a magnet and the water was decanted. The magnetite complex was washed several times with water (5X) and methanol (5X) before drying overnight at 40 ^{0}C under reduced pressure.

Magnetic separation columns comprised of ~6 g of soft iron granules were firmly packed in 3-mL plastic syringes. A magnetic field was generated by a 0.24 Tesla NdFeB doughnut-shaped magnet placed around the exterior of the syringe. The PDMS-magnetite nanoparticles were diluted in chloroform (chloroform is good solvent for PDMS[142]) to a concentration of 0.002 mg mL^{-1}. The dispersion was sonicated with a Biologics ultrasonic homogenizer (model 150V/T) for 5 min using the 50% power setting with a micro-tip probe and a 50% pulse. Following sonication, 150 mL of the chloroform dispersion (0.3 g of particles) were passed through the column at a flow rate of ~20 mL min^{-1} and collected.

4.3.3. Characterization

4.3.3.1. Thermogravimetric Analysis (TGA)

TGA was carried out on the PDMS-magnetite nanoparticles using a TA Instruments TGA Q500. After equilibrating the samples at 25 ºC, the temperature was ramped at 10 ^{o}C min^{-1} to a maximum temperature of 650 ºC under a nitrogen purge. Char yields (the mass remaining at the end of the experiment) were recorded at the maximum temperature.

4.3.3.2. Transmission Electron Microscopy (TEM)

TEM was conducted with a JEOL 3000F field-emission-gun transmission electron microscope (operated at 300kV) equipped with a 1024x1024 pixel digital imaging system. Dry samples of the magnetite complexes were dispersed in chloroform and cast onto amorphous carbon-coated copper grids for analysis. Great care was taken to ensure that both eucentric height and focus were set consistently from one sample to another in order to reduce uncertainty in the digital image analysis. Images were acquired at a magnification of 300kx corresponding to 1.65 pixels nm^{-1}. This magnification yielded both sufficient resolution and contrast for digital image analysis, and provided a large enough field of view to measure adequate numbers of particles. Particle size analysis was performed using Reindeer Graphics' Fovea Pro 4 plug-in for Adobe Photoshop CS2. Means and standard deviations of the particle size diameters were calculated based upon 3500-5000 particles per sample, and particle size distributions were fitted with a Weibull distribution.

4.3.3.3. Dynamic Light Scattering (DLS)

DLS measurements were conducted with a Malvern Zetasizer ZS compact scattering spectrometer (Malvern Instruments Ltd, Malvern, UK) at a wavelength of 633 nm from a 4.0 mW, solid-state He-Ne laser at a scattering angle of 170°.

4.3.3.4. Rheology

Rheology measurements were conducted with a TA Instruments AR-G2 rheometer equipped with a stainless steel cone with an angle of 0.5° and a diameter of 20 mm (truncation 12 μm). The sample volume was approximately 0.03 mL. Steady-state flow experiments were conducted measuring the viscosity of the neat complexes at shear rates from 0.00001 to 10,000 s^{-}

[1] at 25 ˚C with no pre-shear protocol. For comparison, one sample was pre-sheared at 10,000 s^{-1} for 2 min before measurements were made.

4.4. Results and Discussion

4.4.1. Synthesis and Separation of PDMS-magnetite Complexes

Magnetite nanoparticles were precipitated by reacting a stoichiometric ratio of $FeCl_2$ and $FeCl_3$ with hydroxide ion in an oxygen-free environment while being mixed rapidly by a homogenizer. The homogenizer was employed in efforts to minimize aggregate formation during the process. The surfaces of the magnetite nanoparticles were subsequently coated by adsorbing a PDMS oligomer that had three carboxylates on one end and a non-functional trimethylsilyl group at the other (Figure 4.1). The M_n of the functionalized PDMS oligomer was determined to be 3242 g mol^{-1} by ^1H NMR. Following a thorough washing procedure to remove any unbound polymer, a chloroform dispersion of the PDMS-magnetite complexes was passed through a magnetic separation column to remove any large particles and aggregates that might have formed during synthesis.

The particle-polymer composition ratios were determined by weight loss measurements (TGA). The amount of polymer on the surface of the magnetite is necessary for determining the thickness of the stabilizing layer that prevents particle aggregation. The materials were heated under nitrogen in the TGA furnace past the point of thermal degradation of the PDMS brushes, and this left only the magnetite mass as residual char. As previously reported, PDMS leaves no detectable char above 650 ºC when heated under these conditions.[136] It has also been previously demonstrated that the magnetite does not lose any weight under these conditions.[137] The resulting nanoparticle complex was determined by TGA to be 30 weight percent magnetite, and 70 weight percent PDMS oligomer, as targeted.

4.4.2. Transmission Electron Microscopy (TEM)

Particles produced via co-precipitation of iron salts as described herein are polydisperse in nature. Therefore, to understand the interactions among this distribution of particles, a necessary first step is to carefully characterize the particle size and size distribution. TEM in conjunction with image analysis is an effective means to measure the core particle size. A chloroform dispersion of the PDMS-magnetite complex was cast onto a carbon-coated TEM

grid, and the chloroform was allowed to evaporate at room temperature. This sample preparation protocol resulted in the nanoparticles being fairly evenly spread out across the grid. Images of the particles were taken at 300,000 times magnification (Figure 4.2), since this offered the best contrast of particles to background at acceptable resolution.

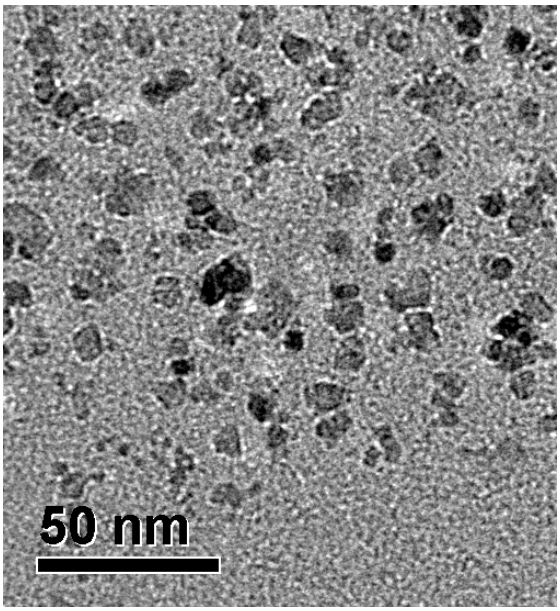

Figure 4.2: Representative TEM image of PDMS-magnetite particles

Size analyses were carried out to determine the distribution of the diameters of the magnetite cores of the nanoparticles. Seven TEM images of the sample were analyzed, resulting in 8439 particles being measured. The images were blurred slightly (2 pixels) to flatten noise in the background, and then an intensity threshold was applied to distinguish the particles from the background. Fovea Pro's watershed tool was utilized to distinguish particles that were close together but not connected. The original image was compared to the threshold image (what the software interpreted to be particles) to check for any discrepancies, and all of the detected errors were manually corrected on the threshold image before particles sizes were measured. This ensured that only true particles were identified in the images and any potential artifacts were removed prior to analysis. The arithmetic mean and standard deviation of core diameters in the distribution were calculated from the data (7.2 and 3.6 nm respectively). It was found that the particle size distribution could be accurately represented (R^2=0.996) by a two-parameter Weibull distribution (Figure 4.3).

$$P(r) = \frac{\gamma}{\alpha}\left(\frac{r}{\alpha}\right)^{\gamma-1} \exp\left(\frac{-r}{\alpha}\right)^{\gamma}$$

Eq. 4.1

where P(r) is the probability of a particle with radius r, α is a scale parameter (α = 4.07 nm), and γ is a shape parameter (γ = 2.11).

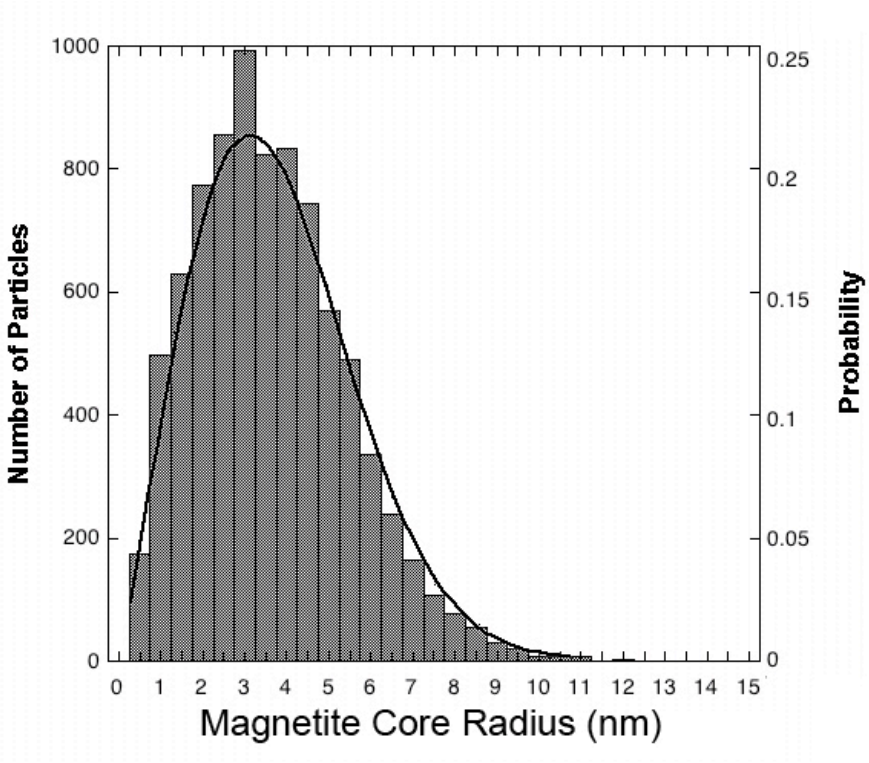

Figure 4.3: Histogram of the radii of the magnetite cores fitted with a Weibull probability function

4.4.3. Dynamic Light Scattering (DLS)

The PDMS-magnetite complex was dispersed in either chloroform or D_4. Chloroform has been shown to be a good solvent for PDMS,[142] and because the repeat unit for D_4 and PDMS is the same, it was reasoned that dispersions in D_4 would approximate theta conditions. There was little if any effect of the solvent quality on the averages (intensity, volume and number average) measured by DLS of the particles in the two solvents (Figure 4.4 and **Error! Reference source not found.**). This is reasonable considering the end-to-end distance of an unperturbed PDMS chain of 3242 g mol^{-1} in solution (3.1 nm for a theta solvent from the wormlike chain

model)[156] its contour length (12.6 nm) relative to the calculated brush thickness (mean is 6.4 nm). The high surface chain density (see section 4.4.4.3) of 3.9 chains nm^{-2} (21 mg m^{-2}) results in highly-stretched PDMS corona chains even in theta conditions. Thus, changing the solvent quality from a theta to a good solvent results in little change in the layer thickness. The averages in both solvents vary in the expected order: intensity > volume > number. In addition, the shape of the distribution of particles was very similar to that of the core particle sizes, indicating that it might be possible to calculate the size of the total complex based on the measured core particle sizes.

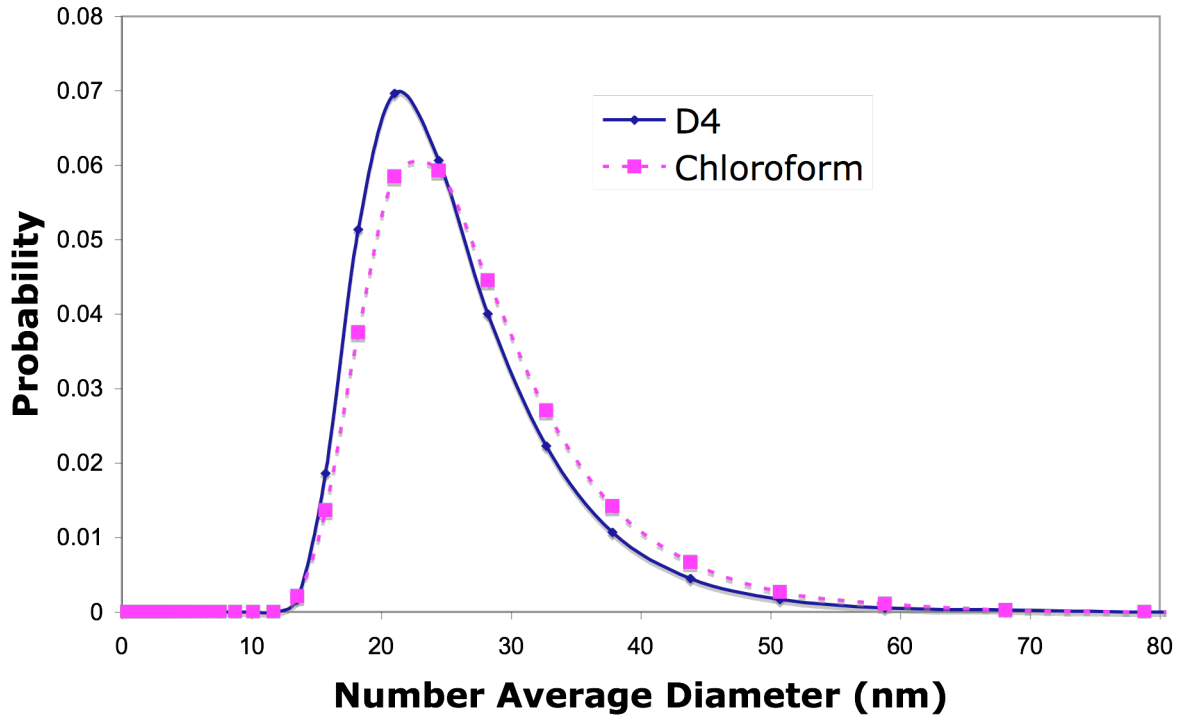

Figure 4.4: Number Average Diameters of the PDMS-Magnetite Complex in D_4 and Chloroform Suspensions from DLS

Table 4.1: Calculated and Measured Values of the Intensity, Volume, and Number Averages of the PDMS-Magnetite Complex Diameter

	Calculated Values (TEM)		Measured Values (DLS)	
Solvent	Good	Theta	$CHCl_3$	D_4
Intensity Average	27.2	26.9	41.2 ± 0.4	46.8 ± 0.6
Volume Average	22.6	21.6	30.2 ± 0.6	32.7 ± 1.9

Number Average	21.2	20.0	24.0 ± 0.8	25.4 ± 2.4

4.4.4. Calculations of Particle-Particle Interactions

A modified form of DLVO theory was utilized to examine interparticle energies to predict stabilities of dilute dispersions of these complexes. The particle-particle interaction potentials were calculated by summing the potentials of van der Waals, V_a, and magnetic, V_m, attractions along with electrostatic, V_e, and steric, V_e, repulsions (Eq. 4.2).

$$V_{total} = V_a + V_e + V_s + V_m$$

Eq. 4.2

The potentials were normalized by thermal energy, k_BT, where k_B is Boltzmann's constant, and T is temperature in Kelvin. Normalizing the data to thermal energy allows for inferences to be made regarding the relative energetics of energy wells that exist with certain compositions, thus suggesting that agglomeration would be likely. In addition, the potentials were calculated as functions of the radii of the magnetite cores, R_c, derived from the TEM size analyses. By considering the net potential as a function of the radius of the magnetite, predictions for the stabilities of dispersions could be made for discrete points along the distribution of core particle sizes.

4.4.4.1. Van der Waals Attractions

The van der Waals portion of the total interaction potential, V_a, was calculated as a function of the magnetite surface-to-surface distance, Δ_{ss}, between two particles of equal size having a core radius, R_c (Figure 4.5).[64, 157]

$$V_a = -\frac{1}{6k_BT} A_{eff} \left(\frac{2R_c^{\,2}}{\Delta_{ss}(4R_c + \Delta_{ss})} + \frac{2R_c^{\,2}}{(2R_c + \Delta_{ss})^2} + \ln\left(\frac{\Delta_{ss}(4R_c + \Delta_{ss})}{(2R_c + \Delta_{ss})^2} \right) \right)$$

Eq. 4.3

where k_B is Boltzmann's constant (1.38×10^{-23} J K^{-1}), T is the Temperature (298 K), and A_{eff} is the effective Hamaker constant that includes retardation effects. A_{eff} was derived from Eq. 4.4.

$$A_{eff} = \frac{3}{4} k_B T \left(\frac{\bar{\varepsilon}(0) - \varepsilon(0)}{\bar{\varepsilon}(0) - \varepsilon(0)} \right)^2 + \frac{3\hbar\omega}{16\sqrt{2}} \frac{\left(\bar{n}_0^2 - n_0^2\right)^2}{\left(\bar{n}_0^2 + n_0^2\right)^{\frac{3}{2}}} F(\delta)$$

Eq. 4.4

where $\varepsilon(0)$ and $\bar{\varepsilon}(0)$ are the dielectric constants for the medium (PDMS) and the substrate (magnetite) (2.5[158] and 20,000[137] respectively), n_0 and $\bar{n_0}$ are the low frequency refractive indices of the medium and substrate (1.43[158] and 1.970[137] respectively), $\hbar$ is Planck's constant (6.63 x 10^{-34} J s), and ω is the frequency of the dominant relaxation in the UV (1.88 x 1016 rad s^{-1}). The function F(δ) accounts for retardation effects, and approaches unity at the point of surface-to-surface contact.

$$F(\delta) \approx \left(1 + \left(\frac{\pi\delta}{4\sqrt{2}} \right)^{3/2} \right)^{-2/3}$$

Eq. 4.5

where δ is a dimensionless surface-to-surface distance relative to the dimensional surface-to-surface separation, Δ_{ss}.

$$\delta = n_0 \left(\bar{n}_0^2 + n_0^2\right)^{1/2} \frac{\Delta_{ss}\omega}{c}$$

Eq. 4.6

where c is the speed of light (3 x 10^8 m s^{-1}).

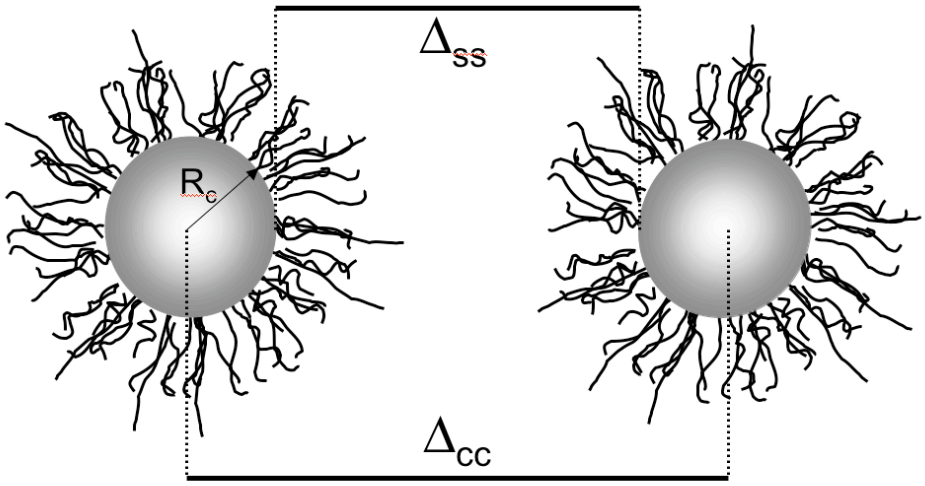

Figure 4.5: Cartoon illustrating distances between particles: center-to-center distance, Δ_{cc}, and surface-to-surface separation of magnetite cores, Δ_{ss}

4.4.4.2. Electrostatic Repulsion

The electrostatic component for the particle-particle potential was calculated via the following equation (Eq. 4.7).

$$V_e = \frac{2\pi R_c \varepsilon(0)\varepsilon_o \psi_o^2 \ln(1+e^{-\kappa\Delta ss})}{k_B T}$$

Eq. 4.7

where ε_0 is the permittivity of free space, Ψ_0 is the surface potential, and $1/\kappa$ is the Debye length. The surface potential of magnetite synthesized by the method described herein has been reported to be ~1.3 mV at neutral pH.[137] Because PDMS is extremely nonpolar, there is only a very low concentration of electrolytes, and this results in the Debye length, $1/\kappa$, approaching zero.[63, 64] Thus Eq. 4.7 reduces to

$$V_e = \frac{2\pi R_c \varepsilon(0)\varepsilon_o \psi_o^2 \ln(1)}{k_B T}$$

$$V_e = 0$$

Eq. 4.8

4.4.4.3. Steric Repulsion

The steric potential relies strongly on the number of chains on each particle. Because the number of chains per particle is directly related to the radius of the magnetite core, R_c, the steric interaction potential was calculated as a function of the core particle size.

The Weibull probability functions derived from TEM and the compositional ratios of polymer to magnetite obtained from the weight loss measurements were utilized to determine the chain density (the number of chains per nm^2 of particle surface area). This was accomplished by first calculating the average surface area, $\overline{A}$, and the average volume of the magnetite cores, $\overline{V}$.

$$\overline{A} = 4\pi\overline{r^2} = 4\pi\int_0^\infty r^2 * P(r)dr$$

Eq. 4.9

and

$$\overline{V} = \frac{4}{3}\pi\overline{r^3} = \frac{4}{3}\pi\int_0^\infty r^3 * P(r)dr$$

Eq. 4.10

where P(r) is a Weibull probability function of radius, r. The surface area of the particles per unit mass was calculated by taking the product of the ratio of average surface area to average volume and the reciprocal of the density of magnetite, $\rho_{magnetite}$ (5.17 g mL^{-1}).[141]

$$\frac{\overline{A}}{\overline{V}} * \frac{1}{\rho_{magnetite}} = \frac{Area}{Mass}$$

Eq. 4.11

The magnetite surface area was determined by taking the mass fractions of the complexes into account (0.3 PDMS and 0.7 magnetite).

$$\frac{Area}{Mass} * Mass\ Fraction\ Magnetite = Surface\ area\ of\ particles$$

Eq. 4.12

In a similar manner, by considering the mass fraction of the polymer and dividing by the number average molecular weight, M_n (3242 g mol^{-1}), and multiplying by Avogadro's number, N_a, the number of chains on the complexes was calculated as

$$Mass\ Fraction\ PDMS * \frac{1}{M_n} * N_a = Number\ of\ chains$$

Eq. 4.13

Using the values from Eq. 4.12 and Eq. 4.13, the average number of chains per unit of surface area was found to be 3.9 chains per nm^2. It has been reported that there are approximately 5.2 binding sites for carboxylate groups per nm^2 on the surface of magnetite.[133] Thus, based on the calculated number of chains on the surface, we conclude that all three binding groups on each chain are likely not bound to the surface of the magnetite.

$$\frac{Number\ of\ chains}{Surface\ area\ of\ particles} = Chains\ /\ Area$$

Eq. 4.14

Using the calculated chain densities, the functionality (number of chains per particle), f(r), of a particle of given radius is

$$f(r) = 4\pi r^2 * \frac{Chains}{Area}$$

Eq. 4.15

4.4.4.3.1. Polymer Brush Size and Chain Density on the Magnetite Surface

A promising model for our polymer-magnetite complexes is the density distribution (DD) model, developed by Vagberg et al.[68] This model, based on a model for star polymers by Daoud and Cotton,[71] assumes concentric shells with a constant number of blobs in each shell. The blob diameter, $\xi(r)$, is a continuous function of distance from the surface. The segment density in the shell varies with distance from the core that, in the present case, is the surface of the magnetite particle. This model is an improvement over flat surface models that have been utilized for predicting steric interactions. By accounting for the effects of surface curvature and changes in chain density in determining the brush thickness, the physics of chain interpenetrations can be better described.

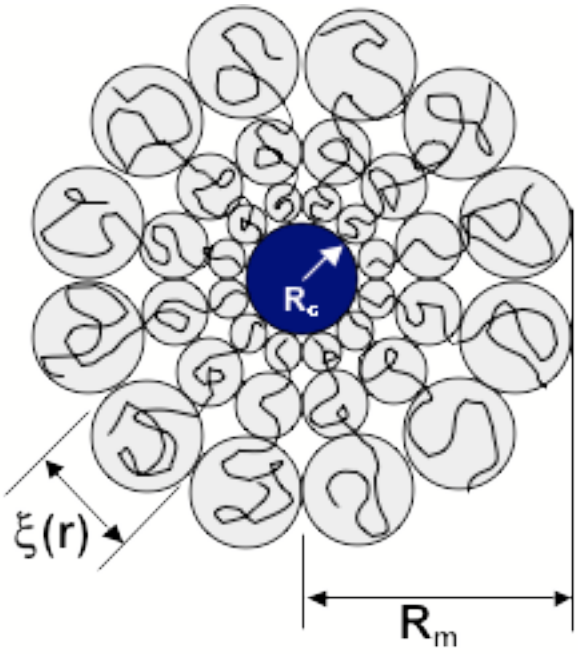

Figure 4.6: Representation of a PDMS-magnetite complex showing the model parameters. Adapted from Daoud and Cotton.[71]

The DD model predicts the radius, R_m, of the PDMS-magnetite complex.

$$R_m(r) = \left(\frac{8 N_k f(r)^{\frac{1-\nu}{2\nu}}}{3 * 4^{1/\nu} \nu} L_k^{1/\nu} + r^{1/\nu} \right)^{\nu}$$

Eq. 4.16

where N_k is the number of statistical or Kuhn segments in one of the corona chains (a PDMS chain in the present case), ν is the Flory exponent, r is the radius of the magnetite core, and f(r) is the number of corona chains per particle. For this work, the Flory exponent, ν, was varied between 0.5 for the case with D_4 as the dispersing medium to simulate theta conditions, to 0.6 for chloroform (a good solvent for PDMS). The statistical segment or Kuhn length L_k is defined as

$$L_k = c_\infty l_0$$

Eq. 4.17

and the number of statistical segments in a chain, N_k, is defined as

$$N_k = n / c_\infty$$

Eq. 4.18

where c_∞ is the characteristic ratio (5.2 for PDMS[68]), l_0 is the average length of a backbone bond (0.155 nm for PDMS), and n is the number of backbone bonds in a chain (2*degree of polymerization for the PDMS).

4.4.4.3.2. Calculation of Sizes of the PDMS-magnetite Complexes

The number average diameter, $\overline{D_n}$, of the complex can be calculated as

$$\overline{D_n} = 2\int_0^\infty P(r)R_m(r)dr$$

Eq. 4.19

The volume average diameter, $\overline{D_v}$, can be calculated as

$$\bar{D}_v = 2\left(\frac{3}{4\pi}\bar{V}_m\right)^{1/3}$$

Eq. 4.20

where the average volume of the PDMS-magnetite nanoparticle complex, $\bar{V}_m$, is found by

$$\bar{V}_m = \frac{4}{3}\pi\int_0^\infty P(r)R_m^3(r)dr\,.$$

Eq. 4.21

The intensity average diameter was determined using a method developed by Prudhomme et al.[143] In dynamic light scattering, the particle sizes can be determined by first describing the relationship between the first cumulant, $\Gamma(q)$, and the scattering from a distribution of particles

$$\frac{\Gamma(q)}{q^2} = \frac{\sum_{j=1}^{\infty} n_j I_j D_j}{\sum_{j=1}^{\infty} n_j I_j}$$

Eq. 4.22

where q is the wave vector, and n_j is the number of particles at a particular radius r_j, I_j is the scattering intensity from these particles, and D_j is the diffusion coefficient.[65] The diffusion coefficient, D_0, for the particles can be described in terms of the first cumulant and the Stokes-Einstein relation.

$$D_0 = \frac{\Gamma(q)}{q^2} = \frac{k_B T}{6\pi\mu r}$$

Eq. 4.23

where k_B is Boltzmann's constant, T is temperature in Kelvin, and μ is the viscosity of the solvent. Combining equations 4.22 and 4.23 the intensity average radius, $\overline{R_I}$, can described in terms of

$$\frac{6\pi\mu\overline{R_I}}{k_B T} = \frac{\sum_{j=1}^{\infty} n_j I_j}{\sum_{j=1}^{\infty} n_j I_j \frac{k_B T}{6\pi\mu R_j}}.$$

Eq. 4.24

The hydrodynamic radius of the particles was shown by DLS to be on the order of 30 nm. Therefore these particles should be in the Rayleigh scattering range in which the scattering intensity, I_j, can be described as

$$I_j = I_0 q^4 \cos^2\theta \left[\left(\frac{n_p}{n_s} \right)^2 - 1 \right]^2 \frac{R_j^{\,6}}{9\beta^2} F_f(\theta)$$

Eq. 4.25

where I_0 is the incident light intensity, θ is the scattering angle, n_p and n_s are the refractive indices of the particle and the solvent respectively, β is the distance from the particle to the light detector, and $F_f(\theta)$ is the Rayleigh form factor .[144] The scattering intensity is directly related to the radius of the particles to the sixth power, and thus equation 4.24 reduces to

$$\overline{R_I} = \frac{\sum_{k=1}^{\infty} n_k R_k^{\,6}}{\sum_{k=1}^{\infty} n_k R_k^{\,5}}.$$

Eq. 4.26

For a particle size distribution described by a Weibull probability function, the discrete summations in eq. 4.26 can be replaced by integrals to calculate the intensity average diameter, $\overline{D_I}$ as

$$\overline{D_I} = 2\overline{R_I} = 2\frac{\int_0^{\infty} P(r) R_m(r)^6 dr}{\int_0^{\infty} P(r) R_m(r)^5 dr}$$

Eq. 4.27

For a given quality of solvent (good, theta), the agreement between the calculated and measured values is best for the number averages (table 4.1). This is reasonable since the number average in DLS measurements gives the least weight to the larger particles in the distribution. The effect of solvent quality on the sizes of the PDMS-magnetite complexes is accounted for in equation 4.16, and is found to be negligible, a trend that was observed by DLS.

4.4.4.3.3. Radius of Gyration, R_g

A critical parameter for the steric interaction (eq. 4.41) is the radius of gyration, R_g, of the particle-polymer complex. One approach is to experimentally measure this using a scattering technique such as static light scattering (SLS) or small angle neutron scattering (SANS). Alternately, one can approximate R_g using the moment of inertia, I, and the mass, m, of the complex.

$$R_g = \sqrt{\frac{I}{m}}$$

Eq. 4.28

The moment of inertia of a composite body is the sum of the moments of inertia of the components. For the case of a magnetite core having a corona of extended PDMS chains, the moment of inertia can be described as

$$I_{total} = I_{magnetite} + I_{corona}$$

Eq. 4.29

Correspondingly, the mass of the ensemble is

$$m_{total} = m_{magnetite} + m_{corona}$$

Eq. 4.30

and the radius of gyration of the entire complex is

$$R_g = \sqrt{\frac{I_{total}}{m_{total}}}$$

Eq. 4.31

The moment of inertia of a mass, m, rotated about an axis at a distance r is given by[159]

$$I = \int r^2 dm$$

Eq. 4.32

Extending this to the moment of inertia of a sphere with density ρ at a distance r from the origin yields

$$I = \int r^2 \rho(r) 4\pi r^2 dr$$

Eq. 4.33

One must define the density of the PDMS-magnetite complex as a function of distance from the center, r. For $r<R_c$, the density is the bulk density of magnetite, $\rho_{magnetite}$.

$$\rho(r) = \rho_{magnetite} \qquad for \quad r < R_c$$

Eq. 4.34

For the PDMS corona, the density is defined by the density distribution model[68] as

$$\rho(r) = m_s A\left(\frac{r}{a_s}\right)^{\frac{1}{\nu}} r^{-3} \quad for \quad R_c < r < R_m$$

Eq. 4.35

in which m_s is the mass of a segment of PDMS, and the constant of proportionality, A, is determined by the relationship between the blob size at the core-corona boundary and the number of corona chains, $f(R_c)$.

$$A = \frac{3 * 4^{\frac{1}{\nu}} f\left(R_c\right)^{\frac{3\nu-1}{2\nu}}}{32}$$

Eq. 4.36

Inserting the expressions in Eq. 4.34 and Eq. 4.35 into the formula for inertia given as Eq. 4.33 yields expressions for the inertia of the core and corona respectively.

$$I_{core} = \int_0^{R_c} r^2 \rho_{magnetite} 4\pi r^2 dr = \frac{4\pi R_c^5 \rho_{magnetite}}{5}$$

Eq. 4.37

$$I_{corona} = \int_{R_c}^{R_m} r^2 m_s A\left(\frac{r}{a_s}\right)^{\frac{1}{\nu}} r^{-3} 4\pi r^2 dr = \frac{4\pi A m_s}{a_s^{1/\nu}\left(2+\frac{1}{\nu}\right)}\left(R_m^{\left(2+1/\nu\right)} - R_c^{\left(2+1/\nu\right)}\right)$$

Eq. 4.38

The mass of the core and the corona can be calculated as:

$$m_{core} = \rho_{magnetite} \frac{4}{3}\pi R_c^{\,3}$$

Eq. 4.39

$$m_{corona} = f(R_c)\frac{M_n}{N_a}$$

Eq. 4.40

Finally, having calculated R_g, the particle-particle steric interaction can be calculated as described by Likos et al.[66, 67]

$$V_s = \begin{cases} \frac{5}{18} f(R_c)^{3/2} \left[-\ln\left(\frac{\Delta_{cc}}{\sigma}\right) + \frac{1}{1+\frac{\sqrt{f(R_c)}}{2}} \right] & for\ \Delta_{cc} \le \sigma \\ \frac{5}{18} f(R_c)^{3/2} \frac{1}{1+\frac{\sqrt{f(R_c)}}{2}} \left(\frac{\sigma}{\Delta_{cc}}\right) e^{\frac{\sqrt{f(R_c)}(\Delta_{cc}-\sigma)}{2\sigma}} & for\ \Delta_{cc} \ge \sigma \end{cases}$$

Eq. 4.41

where σ has been shown to scale in simulations as $\sigma \cong 1.3R_g$.[160]

4.4.4.4. Calculations of Magnetic Interactions

The maximum magnetic interaction between two particles was calculated for the nanoparticles. It was assumed that all the particles were single domain particles and the spins for two interacting particles were aligned. This provides an upper bound for magnetic attractions between two particles in close proximity to one another. In this case the interaction between the particles can be treated similarly to two magnetic dipoles.[3]

$$V_M = -\frac{1}{k_B T} \frac{8\pi\mu_0 R_c^{\,6} M_s^{\,2}}{9\left(\Delta_{cc} + 2R_c\right)^3}$$

Eq. 4.42

where μ_0 is the permeability of free space (1.26 x 10^{-6} m kg s^{-2} A^{-2}), M_s is the saturation magnetization for magnetite (4.66 x 10^5 A m^{-1}), and Δ_{cc} is the center-to-center distance of the particles.

4.4.4.5. Summing of Potentials for Different Points along the Magnetite Particle Size Distribution

Due to the polydisperse nature of the sizes of the magnetite cores, the interparticle potential cannot be simply calculated to represent the behavior of the entire sample. Population Balance approaches have addressed the problem of interactions between particles of dissimilar sizes as the size distribution evolves with time from a monodisperse suspension. However, the present system starts with a polydisperse distribution of magnetite core particles. While pair interaction models for binary colloids (i.e., two different sizes) exist for van der Waals, electrostatic, and magnetic effects, there is currently no such model for describing steric

interactions. Thus, we employ the DLVO theory for particles in a given slice of the size distribution to gain qualitative insight into the effect of particle size on colloid stability.

Calculations of the net interaction potential were made at magnetite core sizes at the 50, 90, 95, and 99th percentiles of the size distribution. For instance, the 50th percentile is a radius in which 50% of the population of particles is smaller than 3.42 nm. Figure 4.7 and Figure 4.8 illustrate the dimensionless potential energy calculated for van der Waals, electrostatic, steric, and magnetic interactions, as well as the sum of the potentials for theta and good solvent conditions respectively. As the particle size of the core increases, the total dimensionless potential energy develops a minimum (Table 4.2). The dispersion properties in terms of stability against flocculation for both cases are remarkably similar. The net-potential is weakly influenced by the solvent conditions, rather particle size is the more dominant factor. At larger particle sizes the distance between the particles at the energy minimum closely approximates twice the length of the polymer brush on the surface of the magnetite. At the highest percentile considered (99th), the energy well is approximately twice that of thermal energy. This suggests that approximately 1% of the particles in dilute solutions would agglomerate (considering particles of equal sizes). These agglomerates would form effectively larger magnetic bodies and these would have a larger dipole moment collectively. Moreover, the newly formed clusters could act as nucleation sites for further agglomeration, first capturing large particles and then having the magnetic strength to capture smaller particles over time.

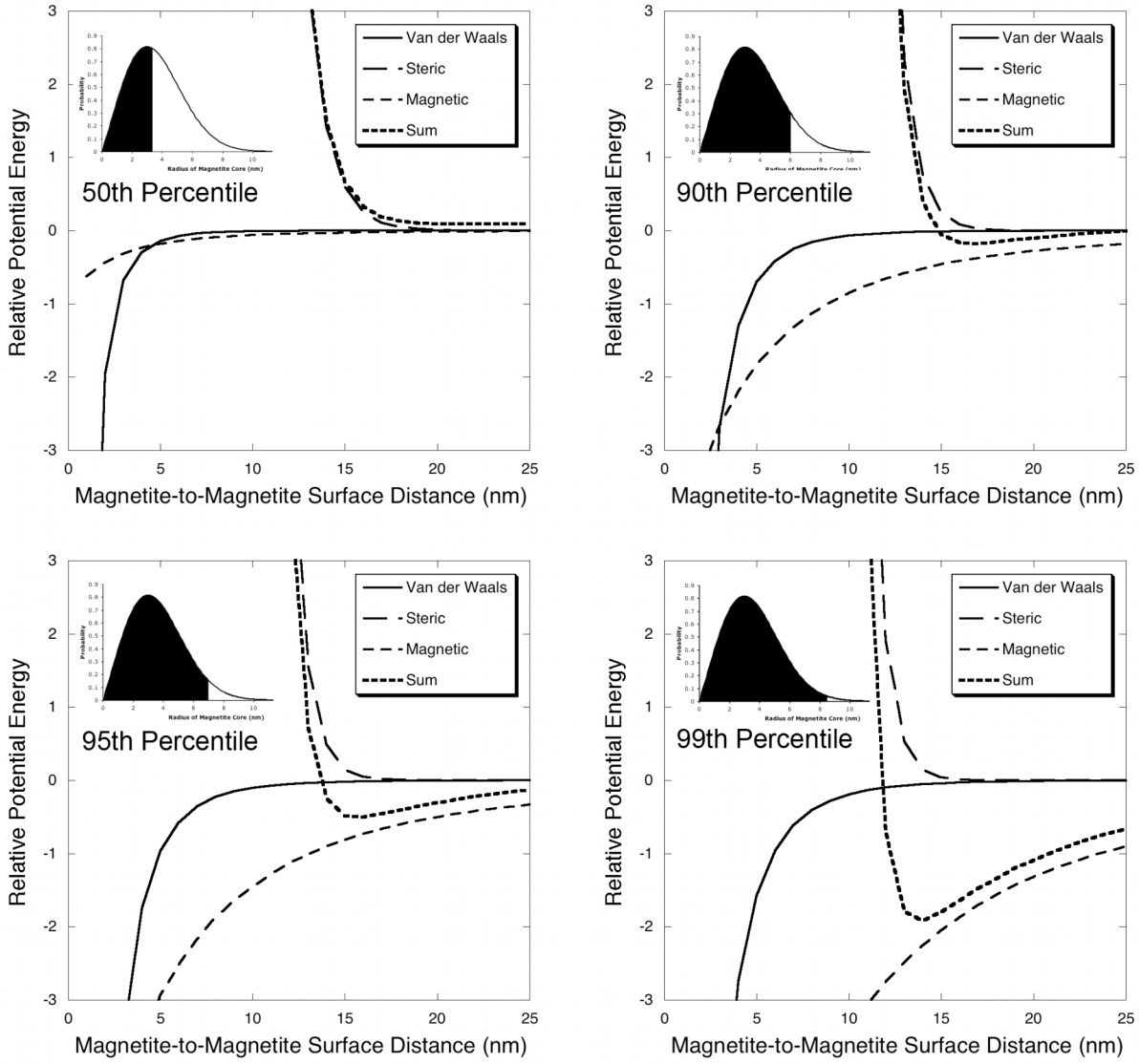

Figure 4.7 Relative Potential Energies Calculated for Two Equal Size Particles at Different Percentiles of the Distribution of Magnetite Core Radii in Theta Solvent Conditions. In the graph of the 50th percentile, it is noted that the V_s and the sum overlap.

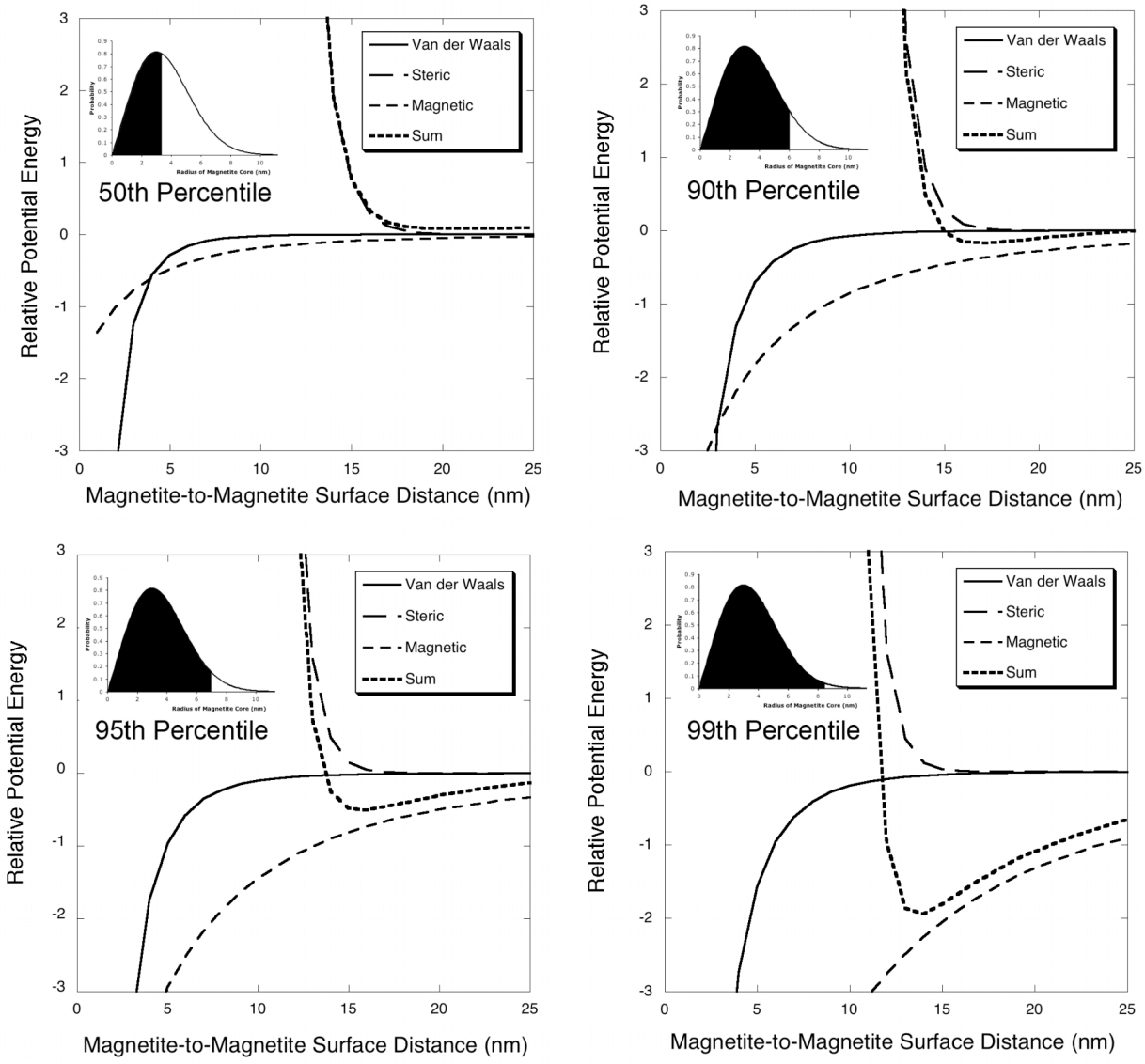

Figure 4.8: Relative Potential Energies Calculated for Two Equal Size Particles at Different Percentiles of the Distribution of Magnetite Core Radii in Good Solvent Conditions

Table 4.2: Particle Radii, Brush Thickness, Minimum Relative Potential Energy, and Distance at Minimum at Different Percentiles of the Size Distribution

	Percentile							
	50th		90th		95th		99th	
Solvent	Theta	Good	Theta	Good	Theta	Good	Theta	Good
Particle Radius (nm)	3.4		6.1		6.8		8.4	
Brush Thickness (nm)	6.2	7.2	7.4	7.7	7.6	7.9	8.0	8.2
Complex Radius (nm)	9.6	10.6	13.4	13.8	14.5	14.7	16.4	16.6
Secondary Minimum Depth	-0.01	-0.01	-0.33	-0.32	-0.62	-0.63	-2.02	-2.04
Separation Distance at Secondary Minimum (nm)	23.9	23.7	17.5	17.6	16.4	16.4	14.5	14.4

4.4.5. Rheology of Neat Magnetite-PDMS Complex Fluids

While the suspension properties of these complexes are important in dilute media, their behavior as neat fluids is also of interestl. One of the applications of these complexes is as ferrofluids for closing holes in retinal tissue.[14-18] In such cases, the complexes must be free of solvent and have flow properties suitable for clinical purposes. The fluid nature of these complexes even without addition of a dispersing medium or carrier fluid is a consequence of the mobile PDMS chains that are terminally bound to the magnetite cores at only one end. This property, in combination with the biocompatibility of the fluids, make these materials uniquely suited for their intended application of remotely closing holes in retinal detachment treatments.[14-16, 18, 93, 94] Fluids of functionalized metal oxide nanoparticles with similar liquid-like properties also been synthesized by other authors.[161-163] For instance, silica nanoparticles have been

functionalized with positively charged organosilanes. Salts were formed on the surface by the addition of either an isostearate or a sulfonate.[161]

To probe the stability of the PDMS-magnetite ferrofluids (without solvent), the rheological properties were investigated as a function of aging time (Figure 4.9). Viscosity (especially at low shear rates) increased as the samples were aged indicating that there might be some formation of clusters. To test if the nanoparticles were irreversibly clustered due to aging, the sample was sheared at 10,000 s^{-1} for two minutes. It was hoped that the kinetic energy from the shearing would break up any clusters that had formed. The measured viscosity of the sheared sample closely matched the sample that was not aged, suggesting that the clusters had been broken up..

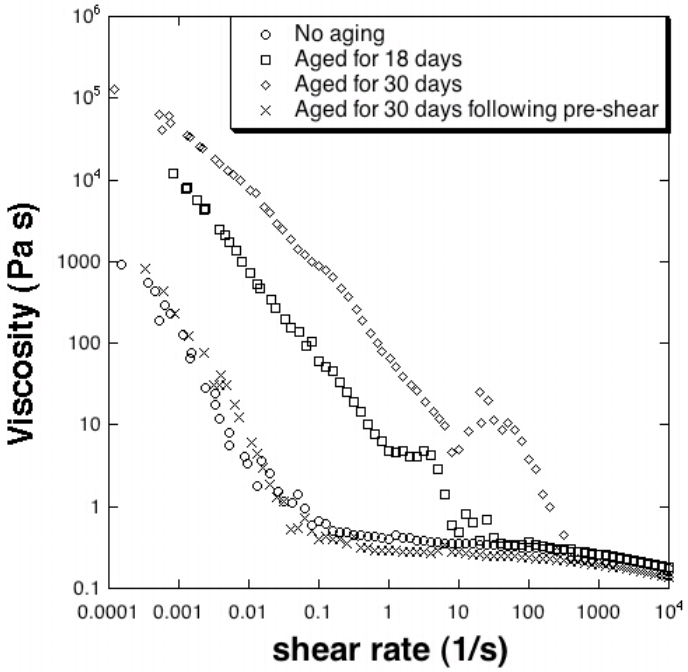

Figure 4.9: Rheological measurements of PDMS-magnetite nanoparticles over time.

4.5. Conclusions

Magnetite nanoparticles were synthesized by reacting iron salts with base, then a PDMS oligomer was adsorbed onto the magnetite nanoparticle surfaces. TEM was used in combination with a polymer brush model to calculate the size distribution of the PDMS-magnetite complexes. The net interparticle potentials for four different particle sizes, representing different portions of a magnetite core size distribution, were examined to obtain a better understanding of the effect of

particle size on the overall stability of dispersions against flocculation. It was observed that larger particles induced an energy well at a magnetite surface-to-surface distance approximately twice that of the polymer brush. For 1% of the particles in the system the energy well was greater than $2k_BT$, indicating that some agglomeration may occur for in dispersions of these polymer-magnetite nanoparticles over time. Finally, the effect of aging on the shear viscosity of a magnetite-PDMS ferrofluid was probed via rheological measurements over time. Increases in shear viscosity (especially at low shear) suggested that some clustering occurs. These clusters could, however, be broken up by applying shear.

4.6. Acknowledgements

The authors are grateful for the financial support of the NSF/ARC Materials World Network for the Study of Macromolecular Ferrofluids (DMR-0602932 and LX0668968), the National Eye Institute of the NIH under SBIR contract B6867G1, and the ARC Discovery Grant - DP0559333. Transmission electron microscopy was carried out using the facilities at the Centre for Microscopy, Characterisation and Analysis, The University of Western Australia, which is supported by University, State and Federal Government funding.

5. Conclusions

The motion of ferrofluid droplets in aqueous media was studied by theoretical analysis and experimental verification. A numerical method for estimating the travel times of the droplets was developed. The method was shown to be accurate to provide an upper bound to the travel times when compared to experiments of the motion of ferrofluid droplets in aqueous media toward external magnets. The calculated forces imposed on the droplets by the external magnets predict that travel times are on the order of seconds to minutes, which indicates that the proposed procedure for remotely closing a retinal hole is scientifically possible. Moreover, the numerical method can be utilized as an aid for the future design of magnets with appropriate sizes and strengths, and these designs may aid in reducing the work required with animal models.

PDMS-magnetite nanoparticle complexes were synthesized and magnetically separated to produce different size distributions for analysis. The complexes that were magnetically separated were smaller and had narrower size distributions than those that were not magnetically separated. TEM and DLS showed similar distributions of particles and complex sizes. The similarity in the distributions of these two size measurements suggested that sizes of the complexes in dispersions could be estimated by examining the core particle size distributions by TEM image analysis, and employing these core sizes in conjunction with colloidal theories. This was accomplished by applying the Daoud and Cotton[71] blob model for star polymers in conjunction with size distributions obtained from the TEM. Calculations of the size of the polymer-particle complex come within close proximity of measurements of hydrodynamic size. If particles of narrower distributions were studied in a similar manner, the calculation would likely come closer to agreement with measured values. With some modifications, this model could be applied to other nanoparticles that are coated with polymers or surfactants, allowing scientists and engineers to approximate the sizes and distributions of newly-developed nanoparticles.

The stability of the polymer-iron oxide complexes was studied using a modified DLVO theory in which van der Waals, steric, electrostatic, and magnetic forces were summed to determine the net interaction of same-sized particles in a dilute dispersion. The net energies were calculated for four sizes representing different points in the size distribution of the magnetite core. It was observed that larger particles induced an energy well at a magnetite surface-to-surface distance approximately twice that of the calculated size of the polymer brush.

For 1% of the particles in the system, the energy well was greater than $2k_BT$, suggesting that agglomeration may occur for the case of same-sized particles in a dispersion. The solvent free properties of the system were investigated via rheological measurements over time. Increases in shear viscosity (especially at low shear rates) suggested some agglomeration occurred with aging. These agglomerates could, however, be broken up by the application of high shear, thus removing the aging history of the material.

6. Recommendations for Future Work

Over the years our trans-disciplinary research group has gained considerable knowledge of synthesis and characterization methods for magnetic nanoparticles coated with polymers, and of the properties of these nanoparticle complexes. We have demonstrated that droplets of complexes comprised of magnetite coated with polydimethylsiloxane oligomers can remain intact as they are moved remotely through aqueous media by applying forces derived from magnetic field gradients. We can alter the size and size distribution of the complexes via magnetic separations, and we have successfully characterized the sizes of both the cores (magnetite) and the complexes in dispersions. We have demonstrated that modified colloidal theories in conjunction with microscopy analyses of the core sizes can be employed to predict the sizes in dispersions, and that the predicted sizes are in reasonable agreement with the experimental values. Moreover, we have begun to characterize the rheology of these neat liquid complexes to investigate stabilities against flocculation. Through this work we have gained the tools necessary to expand in a variety of directions. Key recommended areas for growth are discussed below. Each will require the same teamwork that has made the previous advances possible.

6.1. Magnetophoretic mobility

By placing permanent magnets on the exterior of sample chambers containing ferrofluid droplets, the motion of the droplets could be observed, and the results were compared to theoretical calculations. This proved to be a good first experiment to examine the magnetophoretic properties of these ferrofluids. However, our experimental set-up was limited by poor control of the external magnetic field. To resolve this, a new instrument, *MacroThales*, has been designed and constructed, and this apparatus provides improved user-control of the fields and field gradients to be utilized for applying forces to the ferrofluid droplets. Initial trials using metal sphere standards have demonstrated that the mobility of ferromagnetic materials can be controlled.

However, forming good ferrofluid droplets in either glycerol or water proved to be difficult. Samples have had great affinity to the needle introducing the ferrofluid, the sides of the sample chamber, and the surface of the solution. The science and art of good droplet formation in needs to be better understood. Therefore, we should concentrate on the interfacial energy of PDMS in

both water and glycerol. It might be necessary to add a surfactant to the ferrofluid to help bridge the PDMS-solvent interface. Some possible candidates for surfactants might be the block copolymer PDMS-co-PEO or pluronics. Pendant-drop measurements would be a usefule technique to characterize the interfacial energy of the ferrofluid and water. In addition, special care should be made to assure that surfactant does not leach out into the aqueous solution. Surfactant that does not compose the water-PDMS interface could possibly lead to an immune response. The presence of free surfactant can be assessed by DLS and elemental analysis.

6.2. Particle Size Control

Calculations of particle-particle interaction potentials have demonstrated the importance of the core particle radius on the total potential. By reducing the amount of large particles in the system the likelihood of agglomeration can be significantly reduced. Particle size can be controlled by number of methods. In this work, magnetic filtrations of the nanoparticle dispersions were presented as a low-cost high-throughput method for removing larger particles and aggregates. However variables such as flow rate and amount of captured nanoparticles on the surface of the iron granules can lead to inconsistent results. If more accurate control over particle size distribution is desired, it might be wise to invest in more advanced separation techniques such as magnetic fluid flow fractionation (MFFF). [35, 124, 126-129] Unfortunately, MFFF devices are have only been used in analytical scale application. To use such a device, a specially built system would need to be created for the separation of PDMS-magnetite nanoparticles on a preparative scale.

6.3. Surface chemistry of magnetite

In the analysis of the sizes of the PDMS-magnetite complexes, it was assumed that the PDMS chains uniformly coated the surface of magnetite. Unfortunately this hypothesis cannot be easily determined on nanoparticles. However, if one were able to functionalize a flat magnetite surface, some very detailed surface characterization would become possible. Elipsometry could give an indication of polymer brush thickness in various solvents. Atomic force microscopy (AFM) could be employed to determine uniformity of the surface coating. In addition, more advanced AFM experiments could give an indication of the interaction of PDMS-magnetite coated surfaces. Finally, a quartz crystalline microbalance (QCM) could be used to measure the kinetics of surface adsorption as a function of pH and concentration, assuming that a

sufficiently thin layer of magnetite could be formed. In addition, the effect of solutions such as phosphate buffers (PBS) on any possible displacement of polymer chains could also be investigated using the above described techniques.

6.4. Magnetic particle-particle interactions

In calculating the total particle-particle interaction potential, the maximum magnetic interaction was assumed. This occurs when two nanoparticle spins are aligned with each other. While this assumption allows for some useful inferences to be made regarding the aggregation rates of the particles, it does not fully represent the physics of the particles. One possibility for improving and expanding our understandings of the magnetic attractive forces is to experimentally measure the particle interactions as a function of concentration in a dispersion For instance zero-field-cool measurements could be made for concentrated and highly dilute solutions. The measured magnetization for the two samples could be normalized for magnetite content. In doing so, comparisons could be made for systems in which interparticle interaction would be more (the concentrated solution) and less (the dilute solution) likely. Similar considerations are being pursued by workers at NIST.[164-166] One is cautioned that these experiments should be conducted with the best-defined, and likely the narrowest particle size distributions, that are possible. Collaborations with the NIST team in this endeavor would likely be valuable.

7. References:

1. Tesla, N., *Modern Mechanics and Inventions* **1934,** July.
2. Willard, M. A.; Kurihara, L. K.; Carpenter, E. E.; Calvin, S.; Harris, V. G., Chemically prepared magnetic nanoparticles. *International Materials Reviews* **2004,** 49, (3-4), 125-170.
3. Rosensweig, R. E., *Ferrohydrodynamics*. Cambridge University Press: New York, 1985.
4. Penninga, I.; Waard, H. d.; Moskowitz, B. M.; Bazylinski, D. A.; Frankel, R. B., Remanence measurement on individual magnetotactic bacteria using a pulsed magnetic field. *Journal of Magnetism and Magnetic Materials* **1995,** 149, 279-286.
5. Diebel, C. E.; Proksch, R.; Green, C. R.; Neilson, P.; Walker, M. M., Magnetite defines a vertibrate magnetorecptor. *Nature* **2000,** 406, 299-302.
6. Walker, M. M.; Diebel, C. E.; Haugh, C. V.; Pankhurst, P. M.; Montgomery, J. C.; Green, C. R., Structure and function of the vertebrate magnetic sense. *Nature* **1997,** 390, 371-376.
7. Papi, F.; Luschi, P.; Akesson, A.; Capogrossi, S.; Hays, G. C., Open-sea migration of magnetically disturbed sea turtles. *Journal of Experimental Biology* **2000,** 203, 3435-3443.
8. Mouritsen, H.; Huyvaert, K. P.; Frost, B. J.; Anderson, D. J., Waved albatrosses can navigate with strong magnets attached to their head. *Journal of Experimental Biology* **2003,** 206, 4155-4166.
9. Benhamou, S.; Bonadonna, F.; Jouventin, P., Successful homing of magnet-carrying white-chinned petrels released in the open sea. *Animal Behaviour* **2003,** 65, 729-734.
10. Grassi-Schultheiss, P. P.; Heller, F.; Dobson, J., Analysis of magnetic material in the human heart, spleen and liver. *BioMetals* **1997,** 10, 351.
11. Schultheiss-Grassi, P. P.; Dobson, J., Magnetic analysis of human brain tissue. *BioMetals* **1999,** 12, 67.
12. Pankhurst, Q. A.; Connolly, J.; Jones, S. K.; Dobson, J., Applications of magnetic nanoparticles in biomedicine. *Journal of Physics D: Applied Physics* **2003,** 36, R167-181.
13. Tartaj, P.; Morales, M. d. P.; Veintemillas-Verdaguer, S.; Gonzalez-Carreno, T.; Serna, C. J., The preparation of magentic nanoparticles for application in biomedicine. *Journal of Physics D: Applied Physics* **2003,** 36, R182-R197.
14. Dailey, J. P.; Phillips, J. P.; Li, C.; Riffle, J. S., Synthesis of silicone magnetic fluid for use in eye surgery. *Journal of Magnetism and Magnetic Materials* **1999,** 194, 140-148.
15. Stevenson, J. P.; Rutnakornpituk, M.; Vadala, M. L.; Esker, A. R.; Charles, S. W.; Wells, S.; Dailey, J. P.; Riffle, J. S., Magnetic cobalt dispersions in poly(dimethylsiloxane) fluids. *Journal of Magnetism and Magnetic Materials* **2001,** 225, 47-58.
16. Vadala, M. L.; Zalich, M. A.; Fulks, D. B.; Pierre, T. G. S.; Dailey, J. P.; Riffle, J. S., Cobalt-silica magnetic nanoparticles with functional surfaces. *Journal of Magnetism and Magnetic Materials* **2005,** 293, 162-170.
17. Wilson, K. S.; Goff, J. D.; Riffle, J. S.; Harris, L. A.; St. Pierre, T. G., Polydimethylsiloxane-magnetite nanoparticles complexes and dispersions in polydimethlysiloxane carrier fluids. *Polymers for Advanced Technologies* **2005,** 16, (2-3), 200-211.
18. Mefford, O. T.; Woodward, R. C.; Goff, J. D.; Vadala, T. P.; St. Pierre, T. G.; Dailey, J. P.; Riffle, J. S., Field Induced Motion of Ferrofluids through Immiscible Viscous Media:

Testbed for Restorative Treatment of Retinal Detachment. *Journal of Magnetism and Magnetic Materials* **2007,** 311, 347-353.
19. Jakubovics, J. P., *Magnetism and Magntic Materials*. 2nd ed.; The Institute of Materials: Cambridge, 1994.
20. Leslie-Pelecky, D. L.; Rieke, R. D., Magnetic Properties of Nanostructured Materials. *Chemistry of Materials* **1996,** 8, 1770-1783.
21. Kittel, C., Theory of the Structure of Ferromagnetic Domains in Films and Small Particles. *Physical Review* **1946,** 70, (11-12), 965-971.
22. Papell, S. S. Low viscosity magnetic fluid obtained by the colloidal suspension of magnetic particles. U.S. Patent 3,215,572, 1965.
23. Rosensweig, R. E.; Kaiser, R., Study of Ferromagnetic Liquid, Phase I. In NTIS, Ed. NASA Office of Advanced Research and Technology, Washington, D.C.: 1967; Vol. Rep. No. NASW-1219;.
24. Khalafalla, S. E.; Reimers, G. W., *Separation Science* **1973,** 8, 161-178.
25. Khalafalla, S. E.; Reimers, G. W. Magnetiofluids and their manufacture. U.S. Patent 3,764,540, 1973.
26. Khalafalla, S. E.; Reimers, G. W. Production of magnetic fluids by peptization techniques. U.S. Patent 3,843,540, 1974.
27. McNab, T. K.; Fox, R. A.; Boyle, J. F., Some magnetic properties of magnetite (Fe3O4) microcrystals. *Journal of Applied Physics* **1968,** 39, (12), 5703-5711.
28. Harris, L. A.; Goff, J. D.; Carmichael, A. Y.; Riffle, J. S.; Harburn, J. J.; St. Pierre, T. G.; Saunders, M., Magnetite Nanoparticle Dispersions Stabilized with Triblock Copolymers. *Chemistry of Materials* **2003,** 15, (6), 1367-1377.
29. Shen, L.; Laibinis, P. E.; Hatton, T. A., Aqueous magnetic fluids stabilized by surfactant bilayers. *Journal of Magnetism and Magnetic Materials* **1999,** 194, 37-44.
30. Chantrell, R. W.; Popplewell, J.; Charles, S. W., *IEEE Trans. Magnetics* **1978,** MAG-14, (5), 975-7.
31. Massart, R.; Dubois, E.; Cabuil, V.; Hasmonay, E., Preparation and properties of monodisperse magnetic fluids. *Journal of Magnetism and Magnetic Materials* **149,** 149, 1-5.
32. Fortin, J.-P.; Wilhelm, C.; Sevais, J.; Menager, C.; Bacri, J.-C.; Gazeau, F., Size-Sorted Anionic Iron Oxide Nanomagnets as Colloidal Mediators for Magnetic Hyperthermia. *Journal of the American Chemical Society* **2007,** 129, 2628-2635.
33. Fried, T.; Shemer, G.; Markovich, G., Ordered Two-Dimensional Arrays of Ferrite Nanoparticles. *Advanced Materials* **1158,** 13, (15), 1158-1161.
34. Nunes, A. C.; Yu, Z. C., *Journal of Magnetism and Magnetic Materials* **1989,** 78, 241.
35. Rheinlander, T.; Roessner, D.; Weitschies, W.; Semmler, W., Comparison of size-selective techniques for the fractionation of magnetic fluids. *Journal of Magnetism and Magnetic Materials* **2000,** 214, 269-275.
36. Sun, S.; Zeng, H.; Robinson, D. B.; Raoux, S.; Rice, P. M.; Wang, S. X.; Li, G., *Journal of the American Chemical Society* **2004,** 126, 273-279.
37. Sun, S.; Zeng, H., *Journal of the American Chemical Society* **2002,** 124, 8204-8205.
38. Bae, D.-S.; Han, K.-S.; Cho, S.-B.; Choi, S.-H., Synthesis of ultrafine Fe3O4 powder by glycothermal process. *Materials Letters* **1998,** 37, 255-258.
39. Thomas, J. R., Preparation and magnetic properties of colloidal cobalt particles. *Journal of Applied Physics* **1966,** 37, (7), 2914-5.

40. Hess, P. H.; Parker, P. H., *Journal of Applied Polymer Science* **1966,** 10, 1915-1927.
41. Mailfert, R.; Martinet, A., *Journal of Physics* **1973,** 34, (203), 197-202.
42. Rutnakornpituk, M.; Thompson, M. S.; Harris, L. A.; Farmer, K. E.; Esker, A. R.; Riffle, J. S.; Connolly, J.; St. Pierre, T. G., *Polymer* **2002,** 43, (8), 2337-2348.
43. Stevenson, J. P.; Rutnakornpituk, M.; Vadala, M.; Esker, A. R.; Charles, S. W.; Wells, S.; Dailey, J. P.; Riffle, J. S., *Journal of Magnetism and Magnetic Materials* **2001,** 225, (1-2), 47-58.
44. Vadala, M.; Rutnakornpituk, M.; Zalic, M. A.; St. Pierre, T. G.; Riffle, J. S., *Polymer* **2004,** 45, (22), 7449-7461.
45. Connolly, J.; St. Pierre, T. G.; Rutnakornpituk, M.; Riffle, J. S., *Journal of Physics D: Applied Physics* **2004,** 37, (18), 2475-2482.
46. Baranauskas, V. V.; Riffle, J. S. Oxidatively stable magnetic metal nanoparticles prepared with copolymers containing phthalonitrile moieties, and polymer-metal complexes and their conversion to oxidatively-stable metal nanoparticles. U.S. Patent Applied, 2005.
47. Baranauskas, V. V.; Zalic, M. A.; Saunders, M.; St. Pierre, T. G.; Riffle, J. S., *Chemistry of Materials* **2005,** 17, (21), 5246-5254.
48. Suslick, K. S., Sonochemistry. *Science* **1990,** 247, (4949), 1439-1445.
49. Doktycz, S. J.; Suslick, K. S., Interparticle Collisions Driven by Ultrasound. *Science* **1990,** 247, (4946), 1067-1069.
50. Shafi, K. V. P.; Ulman, A.; Yan, X.; Yang, N.-L.; Estournes, C.; White, H.; Rafailovich, M., Sonochemical Synthesis of Functionalized Amorphous Iron Oxide Nanoparticles. *Langmuir* **2001,** 17, 5093-5097.
51. Vijayakumar, R.; Koltypin, Y.; Felner, I.; Gedanken, A., Sonochemical synthesis an characterization of pure nanometer-sized Fe3O4 particles. *Materials Science and Engineering* **2000,** A286, 101-105.
52. Kumar, R. V.; Koltypin, Y.; Xu, X. N.; Yeshurun, Y.; Gedanken, A.; Felner, I., Fabrication of magnetic nanorods by ultrasound irradiation. *Journal of Applied Physics* **2001,** 89, (11), 6324-6328.
53. Kumar, R. V.; Koltypin, Y.; Cohen, Y. S.; Cohen, Y.; Aubach, D.; Palchik, O.; Felner, I.; Gedanken, A., Preparation of amorphous magnetite nanopartilces embedded in polyvinyl alcohol using ultrasound radiation. *Journal of Materials Chemistry* **2000,** 10, 1125-1129.
54. Chen, D.; Xu, R., Hydrothermal Synthesis and Characterization of Nanocrystalline Fe3O4 Powders. *Materials Research Bulletin* **1998,** 33, (7), 1015-1021.
55. Yi, X.; Yitai, Q.; Jing, L.; Zuyao, C.; Li, Y., Hydrothermal preparation and characterization of ultrafine powders of ferrite spinels MFe2O4 (M=Fe, Zn, and Ni). *Materials Science and Engineering* **1995,** B34, L1-L3.
56. Seip, C. T.; Carpenter, E. E.; O'Connor, C. J., Magnetic Properties of a Series of Ferrite Nanoparticles Synthesized in Reverse Micelles. *IEEE Transactions on Magnetics* **1998,** 34, (4), 1111-1113.
57. Lee, K. M.; Sorensen, C. M.; Klabunde, K. J.; Hadjinpanayis, G. C., Synthesis and Characterization of Stable Colloidal Fe3O4 Particles in Water-In-Oil Microemulsions. *IEEE Transactions on Magnetics* **1992,** 28, (5), 3180-3182.
58. Zhou, Z. H.; Wang, J.; Liu, X.; Chan, H. S. O., Synthesis of Fe3O4 nanoparticles from emulsions. *Journal of Materials Chemistry* **2001,** 11, 1704-1709.

59. Feltin, N.; Pileni, M. P., New Technique for Synthesizing Iron Ferrite Magnetic Nanosized Particles. *Langmuir* **1997,** 13, 3927-3933.
60. Banerjee, S.; Roy, S.; Chen, J. W.; Chakravorty, D., Magnetic properties of oxide-coated iron nanoparticles synthesized by electrodeposition. *Journal of Magnetism and Magnetic Materials* **2000,** 219, 45-52.
61. Larson, R. G., *The Structure and Rheology of Complex Fluids*. Oxford University Press: New York, 1999.
62. Berkovsky, B. M.; Medvedev, V., F.; Krakov, M. S., *Magnetic Fluids*. Oxford University Press: Oxford, 1993.
63. Israelachvili, J. N., *Intermolecular and Surface Forces*. Academic Press: Orlando, FL, 1985.
64. Israelachvili, J. N., *Intermolecular and Surface Forces*. Academic Press: London, 1991.
65. Russel, W. B.; Saville, D. A.; Schowalter, W. R., *Colloid Dispersions*. Cambridge University: Cambridge, 1987.
66. Likos, C. N., Soft matter with soft particles. *Soft Matter* **2006,** 2, 478-498.
67. Likos, C. N.; Lowen, H.; Watzlawek, M.; Abbas, B.; Jucknischke, O.; Allgaier, J.; Richter, D., Star Polymers Viewed as Ultrasoft Colloidal Particles. *Physcial Review Letters* **1998,** 80, (20), 4450-4453.
68. Vagberg, L. J. M.; Cogan, K. A.; Gast, A. P., Light-Scattering Study of Starlike Polymeric Micelles. *Macromolecules* **1991,** 24, 1670-1677.
69. Witten, T. A.; Pincus, P. A., Colloid Stabilization by Long Grafted Polymers. *Macromolecules* **1986,** 19, 2509-2513.
70. Grest, G. S.; Kremer, K.; Witten, T. A., Structure of Many-Arm Star Polymers: A Molecular Dynamics Simulation. *Macromolecules* **1987,** 20, 1376.
71. Daoud, M.; Cotton, J. P., *Journal of Physique* **1982,** 43, 531-538.
72. Barnes, H. A.; Hutton, J. F.; Walters, K., *An Introduction to Rheology*. Elsevier: New York, 1989.
73. Krieger, I. M., Rheology of Polymer Colloids. In *Polymer Colloids*, Buscall, R.; Corner, T.; Stageman, J. F., Eds. Elsevier Science Publishing Co.: New York, 1985; pp 219-246.
74. Einstein, A., *Ann Phys* **1906,** 19, 289.
75. Batchelor, G. K., *J Fluid Mech* **1970,** 41, 545.
76. Batchelor, G. K., *J Fluid Mech* **1971,** 46, 813.
77. Saunders, F. L., *Journal of Colloid Science* **1961,** 16, 13.
78. Batchelor, G. K.; Greene, J. T., *J Fluid Mech* **1972,** 56, 401.
79. Ball, R.; Richmond, P., *J Phys Chem Liquids* **1980,** 9, 99.
80. Onoda, G. Y.; Liniger, E. R., *Phys Rev Lett* **1990,** 64, 2727.
81. Krieger, I. M.; Dougherty, T. J., *Trans Soc Rheol* **1959,** 3, 137.
82. Mews, J.; Frith, W. J.; Strivens, T. A.; Russel, W. B., *AlChE J* **1989,** 35, 415.
83. Bingham, E. C., *US Bureau of Standards Science Paper* **1916,** No. 278.
84. Casson, N., In *In Rheology of Disperse Systems*, Mill, C. C., Ed. Pergamon: New York, 1959.
85. Krieger, I. M.; Maron, S. H., *Journal of Colloid Science* **1956,** 6, (528).
86. Maron, S. H.; Pierce, P. E., *Journal of Colloid Science* **1956,** 11, 80.
87. Krieger, I. M.; Dougherty, T. J., *Trans Soc Rheol* **1959,** 6, 528.
88. Cross, M. M., *Journal of Colloid Science* **1965,** 20, 414.

89. Carreau, P. J., Rheological equations from molecular network theories. *Trans Soc Rheol* **1972,** 16, 99-127.
90. McTague, J. P., Magnetoviscoisty of magnetic colloids. *Journal of Chemical Physics* **1963,** 51, (1), 133-6.
91. Rosensweig, R. E.; Kaiser, R.; Miskolczy, G., *J. Colloid and Interface Sci.* **1968,** 29, (4), 680-6.
92. Calugaru, G.; Badescu, R.; Luca, E., *Rev. Roum. Phys.* **1976,** 21, (4), 305-8.
93. Rutnakornpituk, M.; Baranauskas, V. V.; Riffle, J. S.; Connolly, J.; Pierre, T. G. S.; Dailey, J. P., Polysioxane fluid dispersion of cobalt nanoparticles in silica spheres for use in ophthalmic applications. *European Cells and Materials* **2002,** 3, 102-105.
94. Wilson, K. S.; Goff, J. D.; Riffle, J. S.; Harris, L. A.; Pierre, T. G. S., Polydimethylsiloxane-magnetite nanoparticle complexes and dispersions in polysiloxane carrier fluids. *Polymers for Advanced Technologies* **2005,** 16, 200-211.
95. Martenyuk, M. A.; Raikher, Y. L.; Shlionmis, M. I., On the kinetics of magnetization of suspension of ferrofluid particles. *Soviet Phys JETP* **1974,** 38, (2), 413-416.
96. Shlionmis, M. I., Effective visocisity of magnetic suspensions. *Soviet Phys JETP* **1972,** 34, (6), 1291-1294.
97. Shlionmis, M. I., Magnetic Fluids. *Soviet Phys Uspekhi* **1974,** 17, (2), 153-169.
98. Shlionmis, M. I., Comment on "magnetoviscosity and relaxation in ferrofluids". *Phys Rev E* **2001,** 64, 1-6.
99. Shlionmis, M. I., Ferrohydrodynamics: testing a third magnetization equation. *Phys Rev E* **2001,** 64, 1-4.
100. Shlionmis, M. I., Ferrohydrodynamics: retrospective and issues. In *Ferrofluids, Magnetically Controllable Fluids and Their Application*, Springer: Berlin, 2002; pp 85-111.
101. Felderhof, B. U., Magnetovisocsity and relaxation in ferrofluids. *Phys Rev E* **2000,** 62, (3), 3848-3854.
102. Felderhof, B. U., Reply to "comment on 'magnetoviscosity and relaxation in ferrofluids'". *Phys Rev E* **2001,** 64, (6), 1-4.
103. Felderhof, B. U.; Kroh, H. J., Hydrodynamics of magnetic and dielectric fluid in interaction with electomagnetic fields. *Journal of Chemical Physics* **1999,** 110, (15), 7403-7411.
104. He, W.; Lee, S. J.; Jiles, D. C.; Schimidt, D. H.; Porter, D.; Shinar, R., Design of high-magnetic field gradient sources for controlling magnetically induced flow of ferrofluid in microfluidic systems. *Journal of Applied Physics* **2003,** 10, 7459-7461.
105. Bashtovoi, V.; Bossis, G.; Kuzhir, P.; Reks, A., Magnetic field effect on magnetic fluids. *Journal of Magnetism and Magnetic Materials* **2005,** 289, 376-378.
106. Veguera, J. G.; Dikansky, Y. I., Periodical structure in a magnetic fluid under the action of an electric field and with a shear flow. *Journal of Magnetism and Magnetic Materials* **2005,** 289, 87-89.
107. Naletova, V. A.; Turkov, V. A.; Sokolov, V. V.; Tyatyuskin, A. N., The interaction of the particles of magnetizable suspetions with a wall (wall-adjacent effect) in uniform electric and magnetic fields. *Journal of Magnetism and Magnetic Materials* **2005,** 289, 367-369.
108. Naletova, V. A.; Turkov, V. A.; Tyatyuskin, A. N., Spherical body in a magnetic fluid in uniform electric and magnetic fields. *Journal of Magnetism and Magnetic Materials* **2005,** 289, 370-372.

109. Rinaldi, C.; Chaves, A.; Elborai, S.; He, X.; Zahn, M., Magnetic Fluid Rheology and Flows. *Current Opion in Colloid and Interface Science* **2005,** 10, 141-157.
110. Boyer, T. H., *Am. J. Phys.* **1988,** 56, 688-692.
111. Reimers, G. W.; Khalafalla, S. E. U.S. Patent 3843540, 1974.
112. Kelly, J. R. U.S. Patent 4019994, 1977.
113. Molday, R. S. U.S. Patent 4452773, 1984.
114. Suzuki, M.; Shinkai, M.; Kamihira, M.; T, K., Preparation and characteristics of megentite-labled antibody with the use of Poly(Ethylene Glycol) derivatives. *Biotechnol Appl Biochem* **1995,** 21, 335-345.
115. Noguchi, H.; Yanase, N.; Uchida, Y.; Suzuta, T., Preparation and characterization by thermal-analyssi of magnetite latex-particles *Journal of Applied Polymer Science* **1993,** 48, (9), 1539-1547.
116. Carpenter, E. E., *Journal of Magnetism and Magnetic Materials* **2001,** 225, 17.
117. Boutonnet, M.; Kizling, J.; Stenius, P., *Colloids Surf. A* **1982,** 5, 209.
118. Lopez-Quintela, M. A.; J., R., *Journal of Colloid and Interface Science* **1993,** 158, 446.
119. Viau, G.; Fievet-Vicent, F.; Fievet, F., Monodisperse iron-based particles: precipitation in liquid polyols. *Journal of Materials Chemistry* **1996,** 6, (6), 1047-1053.
120. Viau, G.; Fievet-Vicent, F.; F., F., Nucleation and growth of bimetallic CoNi and FeNi monodisperse particles prepared in polyols. *Solid State Ionics* **1996,** 84, 259-270.
121. Park, J.; Lee, E.; Hwang, N.-M.; Kang, M.; Kim, S. C.; Hwang, Y.; Park, J.-G.; Noh, H.-J.; Kim, J.-Y.; Park, J.-H.; Hyeon, T., One-Nanometer-Scale Size-Controlled Synthesis of Monodisperse Magnetic Iron Oxide Nanoparticles. *Angewandte Chemie* **2005,** 44, 2872-2877.
122. Harris, L. A.; Riffle, J. S.; St. Pierre, T. G., Principles of Design and Synthesis of Iron Oxide Magnetic Nanoparticles. *Journal of the Australasian Ceramics Society* **2005,** 41, (2), 23-42.
123. Watson, J. H. P., Magnetic Filtration. *Journal of Applied Physics* **1973,** 44, (9), 4209-4213.
124. Rheinlander, T.; Kotitz, R.; Weitschies, W.; Semmler, W., Magnetic fractionation of magnetic fluids. *Journal of Magnetism and Magnetic Materials* **2000,** 219, 219-228.
125. Sarikaya, M.; Abbasov, T.; Erdemoglu, M., Saome Aspects of Magnetic Filtration Theory for Removal of Fine Particles from Aqueous Suspensions. *Journal of Dispersion Science and Technology* **2006,** 27, 193-198.
126. Espy, M. A.; Sandin, H.; Carr, C.; Hanson, C. J.; Ward, M. D.; Jr., R. H. K., An Instrument for Sorting of Magnetic Microparticles in a Magnetic Field Gradient. *Cytometry Part A* **2006,** 69A, 1132-1142.
127. Carpino, F.; Moore, L. R.; Zborowski, M.; Chalmers, J. J.; Williams, P. S., Analysis of magnetic nanoparticles using quadrupole magnetic field-flow fractionation. *Journal of Magnetism and Magnetic Materials* **2005,** 293, 546-552.
128. Latham, A. H.; Feitas, R. S.; Schiffer, P.; Williams, M. E., Capillary Magnetic Field Flow Fractionation and Analysis of Magnetic Nanoparticles. *Anal. Chem.* **2005,** 77, 5055-5062.
129. Kelland, D. R., Mangetic Separation of Nanoparticles. *IEEE Trans. Magnetics* **1998,** 34, (4), 2123-2125.
130. Miller, G. W.; Saunders, J. H., The thermal analysis of polymers. II. Thermomechanical analyses of segmented polyurethane elastomers. *Journal of Applied Polymer Science* **1969,** 13, (6), 1277-1288.

131. Helmer, J. D.; Polmanteer, K. E., Supercooling of polydimethylsiloxane. *Journal of Applied Polymer Science* **1969,** 13, (10), 2113-2118.
132. Malvern, *Calculating Volume Distribution From Dynamic Light Scattering*. Frequently Asked Questions ed.; Malvern Instruments: Worcestershire, UK, 2007.
133. Sun, Z.-X.; Su, F.-W.; Forsling, W.; Samskog, P.-O., Surface Characteristics of Magnetite in Aqueous Suspension. *Journal of Colloid and Interface Science* **1998,** 197, 151-159.
134. Viota, J. L.; Vicente, J. d.; Duran, J. D. G.; Delgado, A. V., Stabilization of magnetorheological suspensions by polyacrylic acid polymers. *Journal of Colloid and Interface Science* **2005,** 284, 527-541.
135. Caba, B. Brush-Forming Copolymers on Magnetite Nanoparticles. Virginia Tech, Blacksburg, VA, 2007.
136. Jovanovic, J. D.; Govedarica, M. N.; Dvornic, P. R.; Popovic, I. G., The thermogravimetric analysis of some polysiloxanes. *Polymer Degradation and Stability* **1997,** 61, 87-93.
137. Zhang, Q.; Thompson, M. S.; Carmichael, A. Y.; Caba, B. L.; Zalic, M. A.; Lin, Y. N.; Mefford, O. T.; Davis, R. M.; Riffle, J. S., Experiments and Theory of Aqueous Dispersions of Magnetite Nanoparticles Complexed with Copolyether Dispersants. *Langmuir* **2007,** In Press.
138. Bury, K. V., *Statistical Models in Applied Science*. Robert E. Krieger Publishing Company: Malabar, Florida, 1986.
139. Morales, M. P.; Andres-Verges, M.; Veintemillas-Verdaguer, S.; Montero, M. I.; Serna, C. J., Structural effects on the magnetic properties of Fe2O3 nanoparticles. *Journal of Magnetism and Magnetic Materials* **1999,** 203, 146-148.
140. Goya, G. F.; Berquo, T. S.; Fonseca, F. C.; Morales, M. P., Static and dynamic magnetic properties of spherical magnetite nanoparticles. *Journal of Applied Physics* **2003,** 94, (5), 3520-3528.
141. *CRC Handbook of Chemistry and Physics*. 87th ed.; CRC Press: Boca Raton, FL, 2006-2007.
142. Lee, J. N.; Park, C.; Whitesides, G. M., Solvent Compatibility of Poly(dimethylsiloxane)-Based Microfluidic Devices. *Anal. Chem.* **2003,** 75, 6544-6554.
143. Liu, Y.; Kathan, K.; Saad, W.; Prud'homme, R. K., Ostwald Ripening of ß-Carotene Nanoparticles *Physical Review Letters* **2007,** 98, 036102.
144. Fuller, G. G., *Optical Rheometry of Complex Fluids*. Oxford University Press: New York, 1995.
145. Neuberger, T.; Schopf, B.; Hofmann, H.; Hofmann, M.; von Rechenberg, B., Superparamagnetic nanoparticles for biomedical applications: Possibilities and limitations of a new drug delivery system. *Journal of Magnetism and Magnetic Materials* **2005,** 293, (1), 483-496.
146. Thunemann, A. F.; Schutt, D.; Kaufner, L.; Pison, U.; Mohwald, H., Maghemite Nanoparticles Protectively Coated with Poly(ethylene imine) and Poly(ethylene oxide)-block-poly(glutamic acid). *Langmuir* **2006,** 22, 2351-2357.
147. Kim, D. K.; Mikhaylova, M.; Zhang, Y.; Muhammed, M., Protective coating of superparamagnetic iron oxide nanoparticles. *Chemistry of Materials* **2003,** 15, (8), 1617.
148. Hunter, R. J., *Foundations of Colloids Science* Clarendon Press: Oxford, UK, 1992.

149. Verwey, E. J. W.; Overbeek, J. T. G., *Theory of the Stability of Lyophobic Colloids*. Dover: Mineola, NY, 2000.
150. Deryaguin, B. V.; Landau, L. D., Theory of the stability of strongly charged lyophobic sols and the adhesion of strongly charged particles in the solution of electrolytes. *Acta Physicochim (USSR)* **1941,** 14, (633-652).
151. Verwey, E. J. W.; Overbeek, J. T. G., *Theory of Stability of Lyophobic Colloids*. Elsevier: Amsterdam, 1948.
152. Kim, T.; Lee, K.; Gong, M.-s.; Joo, S.-W., Control of Gold Nanoparticle Aggregates by Manipulation of Interparticle Interaction. *Langmuir* **2005,** 21, 9524-9528.
153. Viudez, A. J.; Madueno, R.; Pineda, T.; Blazquez, M., Stabilization of Gold Nanoparticles by 6-Mercaptopurine Monolayers. Effects of the Solvent Properties. *Journal of Physical Chemistry B* **2006,** 110, (17840-17847).
154. Tsouris, C.; Scott, T. C., *Journal of Colloid and Interface Science* **1995,** 171, 319-330.
155. Pshenichnikov, A. F.; Fedorenko, A. A., *Journal of Magnetism and Magnetic Materials* **2005,** 292, 332-344.
156. Yamakawa, H., *Modern Theory of Polymer Solutions*. Harper and Row: 1971.
157. Stokes, R. J.; Evans, D. F., *Fundamentals of Interfacial Engineering*. Wiley-VCH: New York, 1996.
158. Gelest, Silicon, Germanium, Tin and Metal-Organic Compounds. In 2006.
159. Beer, F. P.; Johnston, R. J., *Vector Mechanics for Engineers: Statics*. McGraw Hill: New York, 1990.
160. Jusufi, A.; Watzlawk, M.; Lowen, H., Effective Interaction between Star Polymer. *Macromolecules* **1999,** 32, 4470-4473.
161. Bourlinos, A. B.; Giannelis, E. P.; Zhang, Q.; Archer, L. A.; Floudas, G.; Fytas, G., Surface-functionalized nanoparticles with liquid-like behavior: The role of the constituent components. *The European Physical Journal E* **2006,** 20, (109-117).
162. Warren, S. C.; Banholzer, M. J.; Slaughter, L. S.; Giannelis, E. P.; DiSalvo, F. J.; Wiesner, U. B., Generalized Route to Metal Nanoparticles with Liquid Behavior. *Journal of the American Chemical Society* **2006,** 128, 12074-12075.
163. Noginova, N.; Weaver, T.; King, M.; Bourlinos, A. B.; Giannelis, E. P.; Atsarkin, V. A., NMR and spin relaxation in systems with magnetic nanoparticles. *Journal of Physics: Condensed Matter* **2007,** 19, 076210.
164. Taketomi, S.; Drew, R. V.; Shull, R. D., Peculiar magnetic aftereffect of highly diluted frozen magnetic fluids. *Journal of Magnetism and Magnetic Materials* **2006,** 307, 77-84.
165. Taketomi, S.; Shull, R. D., Experimental verification of interactions between randomly distributed fine magnetic particles. *Journal of Magnetism and Magnetic Materials* **2003,** 266, 207-214.
166. Taketomi, S.; Shull, R. D., Experimental study of magnetic interactions between colloidal particles in magnetic fluids. *Journal of Applied Physics* **2002,** 91, (10), 8546-8548.

VITAE

Thompson Mefford was born on May 16, 1981 to Olin and Donna Mefford. He grew up in Florence, AL and a graduated salutatorian from Coffee High School in 1999. He attended Clemson University, graduating summa cum laude with a bachelors of Science degree in Textile and Polymer Chemistry and a minor in Philosophy. In 2003, Thompson enrolled at Virginia Tech pursuing at doctorate in Macromolecular Science and Engineering. During his time there, he traveled to the University of Western Australia twice to study the magnetic properties of iron-oxide nanoparticles. Upon completion of his degree, Thompson plans to stay in academia.